TUHH
Hamburg University of Technology

Institute for Ship Structural
Design and Analysis

Master Thesis

Fracture mechanics simulation of welded joints at sub-zero temperatures considering the weld shape

Author:	Nils-Erik Sanhen
Matriculation number:	21491441
Degree programme:	Product Development, Materials and Production
First examiner:	Prof. D.Sc. (Tech.) Sören Ehlers
Second Examiner:	D.Sc. (Tech.) Franz von Bock und Polach
Supervisor:	Dr.-Ing. Moritz Braun

Hamburg, 27th January 2022

Abstract

Welded joints are the most common method for connecting steel components, but they are also points of weakness, as they contain, among other things, initial cracks or are unwelded gaps. Most of the fatigue life of a welded joints takes place during the phase of macro crack growth, fracture mechanics models are therefore widely used method to predict the fatigue life. In this thesis, a procedure is developed how fracture mechanics simulations can be conducted automatically for a large number of welded joints with heterogeneous geometries. Therefore, an integrated procedure is developed in which parametric simulation models are generated, fracture mechanically analysed and the results together with their metadata are saved in a selectable master file. Then, the fatigue lives are calculated from the numerical results via the Paris-Erdogan equation and compared with the experimentally determined data. It is shown that by adapting the Paris-Erdogan parameters, high accuracy can be achieved in predicting fatigue lives under sub-zero temperatures. Moreover, a method is described in which a low effort verification of the Paris-Erdogan parameters C and m, separately from each other, by comparing numerical and experimental fatigue lives in a logarithmic space.

TUHH
Hamburg University of Technology

Institute for Ship Structural
Design and Analysis
Prof. Dr.-Ing. habil. A. Düster
Prof. D.Sc. (Tech.) Sören Ehlers

Master Thesis Description for

Nils-Erik Sanhen

Fracture mechanics simulation of welded joints at sub-zero temperatures considering the weld shape

(Deutsch: Bruchmechanische Simulation von Schweißverbindungen bei Minusgraden unter Berücksichtigung der Schweißnahtgeometrie)

To this day many different local fatigue assessment methods have been proposed and are still being developed. Each of them has benefits and downsides for particular problems. Most fatigue assessment methods which are used for ship and offshore structures like the nominal, the structural, or the notch stress approach were initially developed for structures which experience only small temperature variations. Consequently, fatigue tests were performed at room temperature and temperature effects are usually neglected, unless they're several hundred degrees above room temperature. While detrimental effects due to high temperatures are considered in fatigue design, low temperatures are typically neglected. However, recent research results have proven that low temperatures affect fatigue performance as well.

In order to improve the applicability of current methods for fatigue assessment of larger structures like ships or offshore structures in sub-zero temperature environments it is necessary to improve current assessment procedures. Hence, this project deals with the fracture mechanical simulation of welded joints at sub-zero temperatures.

The following tasks shall be fulfilled:

1. Setup of fracture mechanical models for different weldment geometries and numerical simulation of the crack growth
2. Validation of the fracture mechanical simulations on the basis of analytical formulae
3. Verification of the simulation model using data from experiments
4. Development of a prediction model for fatigue lives at different sub-zero temperature levels
5. Analyse and evaluate the findings in the context of the state-of-the-art presented in the technical literature

Literature studies of specific topics relevant to the thesis work shall be included.

The work scope may prove to be larger than initially anticipated. Subject to approval from the supervisors, topics may be deleted from the list above or reduced in extent.

In the thesis the candidate shall present his personal contribution to the resolution of problems within the scope of the thesis work.

Theories and conclusions should be based on mathematical derivations and/or logic reasoning identifying the various steps in the deduction.

The candidate should utilise the existing possibilities for obtaining relevant literature.

Thesis format

The thesis should be organised in a rational manner to give a clear exposition of results, assessments, and conclusions. The text should be brief and to the point, with a clear language and the objective to be published in a conference article and/or scientific journal. It is thus desirable that the thesis is written in English. Telegraphic language should be avoided.

The thesis shall contain the following elements: An executive summary, list of symbols and acronyms, followed by the main body of the thesis consisting of a brief background introduction, a state of the art defining the knowledge gaps defining the scope or work and limitations, the actual contribution chapters, conclusions with recommendations for further work, references and (optional) appendices. All figures, tables and equations shall be numerated.

The supervisors require that the candidate, in an early stage of the work, presents a written plan for the completion of the work. The plan may include a budget for the use of computer and laboratory resources if applicable, which will be charged to the department. Overruns shall be reported to the supervisors.

The original contribution of the candidate and material taken from other sources shall be clearly defined following basic academic principles and an acknowledged referencing system, which includes the name of the referred authors followed by the publication year in the text. The subsequent reference list can thus be alphabetical.

The report shall be submitted in two copies:

- Signed by the candidate
- The text defining the scope included
- In bound volume(s)
- Drawings and/or computer prints, which cannot be bound should be organised in a separate folder.
- The report shall also be submitted in PDF along with essential input files for computer analysis, spread sheets, MATLAB files etc. in digital format.

Ownership

According to the current rules, the candidate has the ownership of the thesis. Any use of the thesis has to be approved by TUHH M-10 (or external partner when this applies). TUHH M-10

has the right to use the thesis as if a TUHH M-10 employee carried out the work, if nothing else has been agreed in advance.

Registration date:	9th August 2021
Deadline:	17th February 2022
Supervisors:	Prof. D.Sc. (Tech.) Sören Ehlers D.Sc. (Tech.) Franz von Bock und Polach Dr.-Ing. Moritz Braun

Statutory Declaration

“I herewith declare that I have composed the present thesis myself and without use of any other than the cited sources and aids. Sentences or parts of sentences quoted literally are marked as such; other references with regard to the statement and scope are indicated by full details of the publications concerned. The thesis in the same or similar form has not been submitted to any examination body and has not been published. This thesis was not yet, even in part, used in another examination or as a course performance.

Hamburg, 27th January 2022

Nils-Erik Sanhen

Table of Contents

List of Figures

List of Tables

Acronyms

Acronym	Meaning
BM	Base material
C-joint	Cruciform joint
DBTT	Ductile-brittle transition temperature
FCG	Fatigue crack growth
FDBT	Fatigue ductile-brittle transition
FEM	Finite element method
FTT	Fatigue transition temperature
HAZ	Heat affected zone
RT	Room temperature
SIF	Stress intensity factor
TUHH	Hamburg University of Technology
WM	Weld material

List of Symbols

Symbol	Unit	Meaning
a	[mm	Crack length
a/c	[ ]	Aspect ratio
a_f	[mm]	Final crack depth
a_i	[mm]	Initial crack size
b	[mm]	Width of the specimen
c	[mm]	Crack width
C	[ ]	Parameter for the Paris-Erdogan equation
c_f	[mm]	Final crack width
c_i	[mm]	Initial crack width
da	[mm]	Crack step size
da/dN	[mm]	Crack propagation per cycle
e	[mm]	Axial misalignment
E	[GPa]	Youngs modulus
f_w	[ ]	Finite width correction factor
f_Φ	[ ]	An angular function from the embedded elliptical crack
g	[ ]	Correction factor depending on the crack depth and the position in the elliptical crack
H	[mm]	Weldment heigh
$h_1 \dots h_4$	[mm]	Vertical deflection in measurement setup
K	[N/mm$^{3/2}$]	General stress intensity factor
K_I	[N/mm$^{3/2}$]	Stress intensity factor for mode I
$K_{Ic,median}$	[MPa*m$^{1/2}$]	Estimate of fracture toughness via master curve
K_{Ic}, K_c	[N/mm$^{3/2}$]	Fracture toughness
k_m, $k_{m,e}$, $k_{m,a}$	[ ]	Total stress magnification factor, stress magnification factors for axial and angular misalignment
K_{max}	[N/mm$^{3/2}$]	Maximum stress intensity factor
K_t	[ ]	Stress concentration factor
m	[ ]	Parameter for the Paris-Erdogan equation
M	[ ]	Stress intensity magnification factors for a crack in a plain plate

M_a	[ ]	M for the deepest point of the crack
M_c	[ ]	M for the point at the surface
M_k	[ ]	Stress intensity magnification factors describing the specific case
M_{ka}	[ ]	M_k for the deepest point of the crack
M_{kc}	[ ]	M_k for the point at the surface
N_f	[ ]	Number of load cycles until final crack depth is reached
p	[mm]	Depth of fusion
Q	[ ]	Shape factor for elliptical crack
R	[ ]	Stress ratio
T	[mm]	Thickness of the loaded plate
t	[mm]	Thickness of the non-loaded plate
T_{100}	[°C]	Temperature for a median toughness of 100 MPa√m
T_{27J}	[°C]	Temperature at which the material will break at an energy of 27J in Charpy Test
T_{50J}	[°C]	Temperature at which the material will break at an energy of 50J in Charpy Test
T_{exp}	[°C]	Test temperature
T_P	[°C]	Peak temperature during welding
W	[mm]	Weldment width
Y	[ ]	General dimensionless geometric factor
ΔK	[N/mm$^{3/2}$]	Range of the general stress intensity factor
$\Delta K_{I,analytic}$	[N/mm$^{3/2}$]	Range of stress intensity factor for mode I, analytical calculated
ΔK_{th}	[N/mm$^{3/2}$]	Fatigue crack growth threshold
$\Delta \overline{K_I}$	[N/mm$^{3/2}$]	Averaged stress intensity factor for mode I
ΔN	[ ]	Constant cycle increment
$\Delta\sigma$	[MPa]	Stress range
Θ	[°]	Weld angle
ν	[ ]	Poisson's ratio
σ	[MPa]	Remote loading stress
σ_m	[MPa]	Mean stress
σ_{max}	[MPa]	Upper stress level
σ_{min}	[MPa]	Lower stress level

Φ	[rad]	Position in the curved crack front
ϕ	[°]	Angular misalignment

1 Introduction

Prior to the actual start of the thesis, this chapter will briefly describe the overarching problem of the subject area and deduce the motivation for this thesis from it. At the end of the chapter, the basic structure of the thesis will be discussed.

1.1 Current situation

Steel is still by far the most important structural material in industrial machinery and plant engineering due to its low cost and excellent mechanical properties [Augu22]. Thereby, the most frequently used joining technology in the industry is welding. It allows high strength connections, is material efficient and enables efficient lightweight construction. However, the welding process also results in a high heat influx into the structure, which causes microstructural changes in the weldment and in the heat-affected zone and can lead to an increased risk of brittle fracture or cracking [Frau22]. With respect to the fatigue behaviour of weldments, the temperature dependency of these features, as well as of the material steel in general, has been investigated in the past decades, mainly with regard to the effects at high temperatures. One driver of this trend was the great interest in more efficient turbines for thermal power plants. With the transformation of energy supply systems away from fossil fuels towards renewable energies, a wider focus on the temperature dependency of steel is to be expected, in addition to high temperatures, the sub-zero temperature range is expected to attract more attention by industry and science. One such example are the challenges faced by the installation of offshore turbines in Nordic countries, which is necessary to balance out local fluctuations in the energy supply. Due to the harsh climate conditions, the support structures of the wind turbines have to be designed for sub-zero temperatures, which requires the precise estimation of the temperature behaviour on the fatigue strength of steel [Brau22].

It has also to be noted that in recent years the research activity in this field has increased noticeably, while in the past special sub-zero temperatures effects related to material selection have been largely neglected, recently there are many publications that go beyond the mere consideration of fracture toughness alone [Brau20b]. So, studies show that the fracture toughness of steel decreases with the temperature but the fatigue strength at sub-zero temperatures increases at the same time [Alva14]. For the estimation of the influence of such effects on the fatigue behaviour of weldments, the weld seams and the adjacent zones are of particular importance. This is because the failure of a weldments usually occurs either at the weld root or at the weld toe [Fric12]. For the fatigue behaviour of welded joints, besides the residual stresses and acting load collectives, the weld geometry is of particular importance, which is why these local geometries assume a central position in the following thesis [Frau22].

1.2 General objective

The ultimate goal of this thesis is to better predict the fatigue life of weldments in order to reduce the over-dimensioning of constructions for sub-zero temperatures and thus to increase their efficiency. The crack propagation approach represents a tool to predict the fatigue life of a propagating crack. This is of great importance because a structural component does not fail due to the presence of a crack, but only when the crack has reached a critical crack length [Fric13]. The crack growth is strongly influenced by the local geometry; therefore, a procedure should first be developed with which weldments of different dimensions can be modelled. Subsequently, fracture mechanics simulations should be conducted on the basis of these models. The results of the simulations can then be compared with the results of experiments that have been conducted at different temperature levels. Based on these comparisons, it is to examine if and how the temperature influences can be taken into account in fracture mechanical simulations.

1.3 Structure of the thesis

At the beginning of the thesis, Chapter 2 provides a brief introduction to the fundamental definitions and concepts that are needed for the understanding of this thesis. In the following Chapter 5, the experimental setup is presented, which is then to be simulated fracture mechanically. Chapter 4 describes the procedure for creating the simulation models, the fracture mechanics simulations and the validation of the results. Based on the experimental data and the simulation models, Chapter 5 tries to develop a model that predicts the fatigue life at different sub-zero temperatures. In Chapter 6 the results are analysed and evaluated, before Chapter 7 summarises the central points of the thesis. In the concluding Chapter 8, a brief outlook is given on questions arising from this work.

2 State of the art

This chapter presents and briefly explains the theories and variables on which the thesis is based. A comprehensive presentation of the topic is not intended, rather the content is limited to elements that are relevant for considerations in the further course of this elaboration.

2.1 Phases of the fatigue life

The fatigue life can be separated in a crack initiation period and a crack growth period, see Figure 2.1. This distinction is useful, because the driving effects and used prediction methods are different. In the crack initiation period, fatigue is particularly a material surface phenomenon. An important parameter for predicting crack initiation is the stress concentration factor K_t. When the microcrack growth is no longer depending on the material surface conditions, the crack growth period starts. The crack growth period describes the advancing of crack penetration into the material. The stress intensity factor K is used for predictions of crack growth. [Schi09]

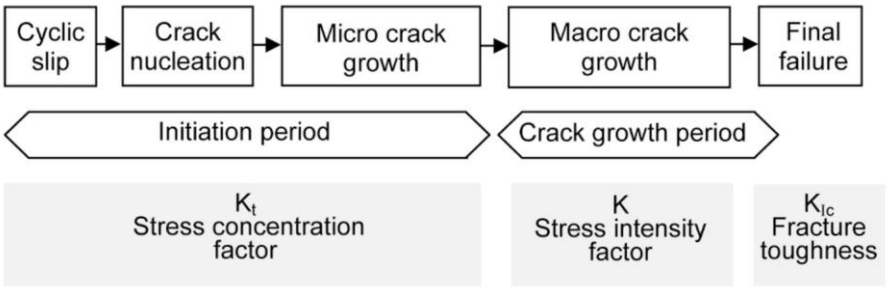

Figure 2.1: Different phases of the fatigue life and relevant factors [Schi09]

This thesis examines the fatigue properties of welded joints, more precisely cruciform joints (C-joints) and doubled-sided transverse stiffener. Weldments have typically short crack initiation periods, because of material defects and a lack of fusion. Therefore, this text will mainly cover the crack growth period.

2.2 Characteristics of stress cycles

External forces and moments applied on a body result in stresses, together with the residual stresses they can be described by stress cycles. Each stress cycle can be described by an upper stress σ_{max}, a lower stress σ_{min} and a mean stress σ_m [Fric17], see Figure 2.2.

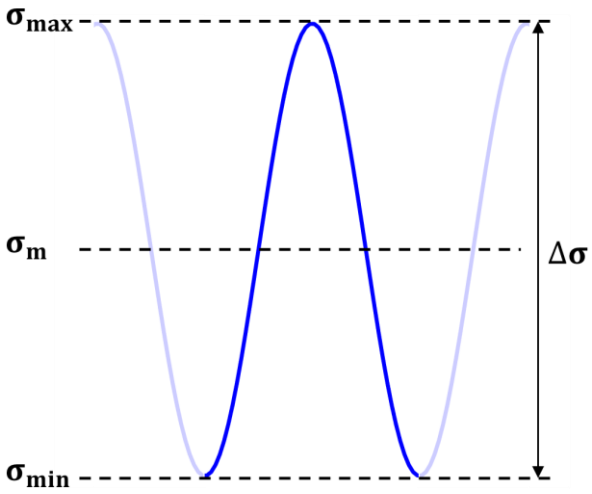

Figure 2.2: Characteristic stress levels of a load cycle

With the parameters describing the stress cycle, further parameters can be represented. One is the stress ratio *R*, which defines the ratio between the upper stress level and the lower stress level, and the other is the stress range *Δσ*.

$$R = \frac{\sigma_{min}}{\sigma_{max}} \tag{2.1}$$

$$\Delta\sigma = \sigma_{max} - \sigma_{min} \tag{2.2}$$

To investigate the fatigue life of test specimens, they are loaded with a sequence of stress cycles at a specific frequency. The entirety of the individual stress cycles is called stress history. It is possible to load the specimens with a sequence of different, variable amplitudes as well as with a sequence of constant amplitudes. For the investigation of fatigue parameters, these tests are often conducted under constant amplitudes, tests with constant amplitudes are also used in this thesis. [Schi09]

2.3 S-N curve

The connection between load amplitudes and the number of load cycles until final crack depth is reached N_f is described by S-N curves. A S-N diagram covers the stress level above the fatigue limit, the number of life cycles at these stresses is infinite, and below the tensile strength of a material, at this stress failure occurs at the first cycle. To create an S-N diagram, a number of fatigue strength experiments under a constant amplitude are run, as there is always a scatter. Tests are run both at high stresses, low cycle fatigue, and at low stresses, high cycle fatigue. Each S-N curve only valid for one definite stress ratio *R* [Fric17]. An example of a S-N diagram is shown in Figure 2.3.

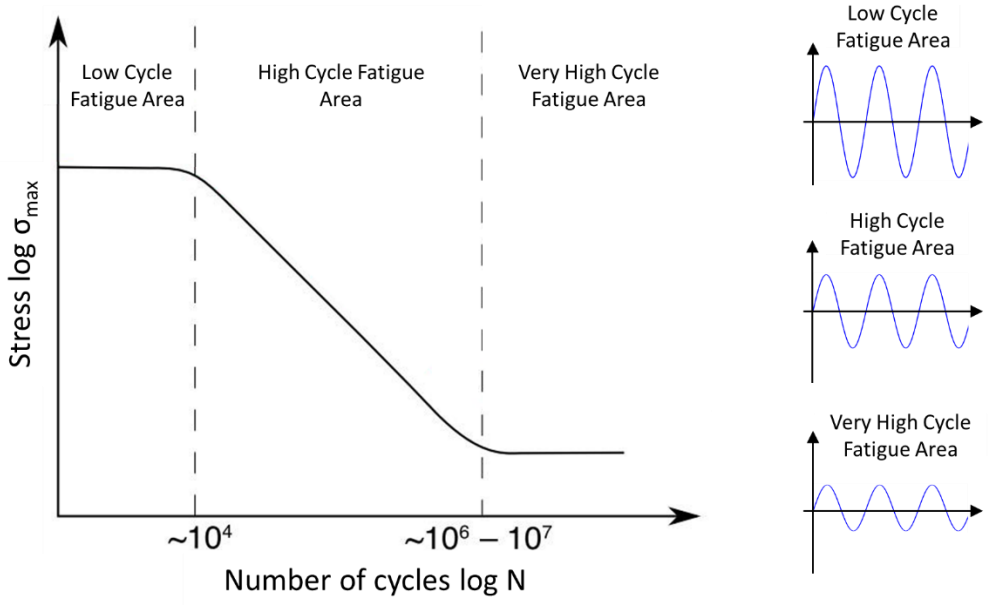

Figure 2.3: Example of a S-N curve

2.4 Stress intensity factor of cracks

To characterise the stress distribution around a notch during the crack initiation period the stress concentration factor K_t is used. For the crack growth period this concept is not possible because cracks usually have a radius of zero and the value K_t of would be infinite. Thus, the stress distribution around the crack uses the stress intensity factor (SIF) K which can be written as [Schi09]:

$$\mathrm{K} = \sigma * \sqrt{\pi * a} * Y \tag{2.3}$$

Where:

a = crack length

Y = dimensionless geometric factor

σ = remote loading stress

The general form of the SIF can be separated in three parts, which describe different opening modes. They are dependent of the stress form, tensile stress or shear stress and their orientation in relation to the crack front, see Figure 2.4.

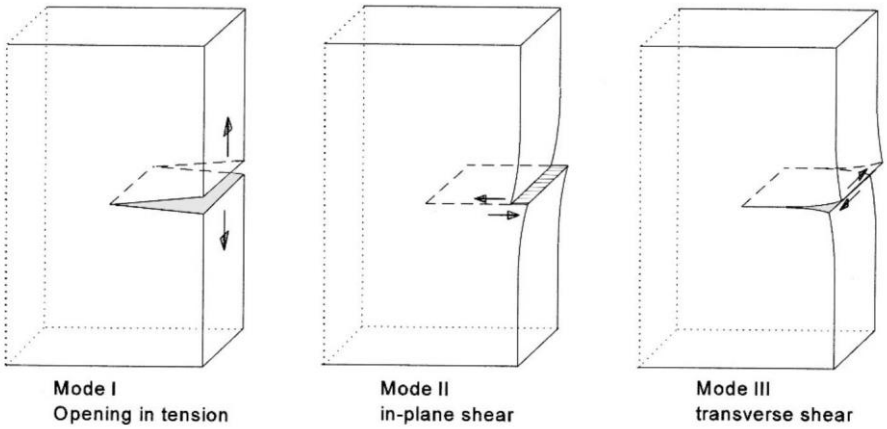

Figure 2.4: Three possible crack modes [Schi09]

The most influential crack mode for fatigue behaviour of weldments is mode I, therefore mode II and III are neglected in this thesis. For fatigue assessment not the actual value of the stress *σ* is relevant but the stress range *Δσ*. The formula for the SIF can be written as:

$$\Delta \mathrm{K}_I = \Delta\sigma * \sqrt{\pi * a} * Y \tag{2.4}$$

The dimensionless geometric factor *Y* combined different factors. Neglecting the parts which have no impact for the subject of this thesis, the standard formula can be written as:

$$\Delta \mathrm{K}_I = \Delta\sigma * \sqrt{\pi * a} * M_k * M \tag{2.5}$$

Where:

M = stress intensity magnification factors for a crack in a plain plate [Bown02]

M_k = stress intensity magnification factors describing the specific case [Bown02]

2.5 Fatigue crack growth regions

To describe the crack growth rate Paris and Erdogan introduce an equation which depicts the relationship between the crack propagation rate *da/dN* and the range of the stress intensity factor *ΔK* [Fric17]. The equation is:

$$\frac{da}{dN} = C * (\Delta K)^m \tag{2.6}$$

In this equation, the dimensionless parameters *C* and *m* are constant and among others depend on material, stress ratio and temperature. The standards BS 6835:1988 and ASTM 647-95a define the procedures and all necessary conditions to obtain feasible Paris law constants [Bran09]. Usually the Paris-Erdogan equation is plotted on a double-logarithmic scale in this representation, the area of constant crack growth can be defined as a linear relationship with the slope *m*, see Figure 2.5. The crack growth can be separated in 3 regions, the threshold region I, the linear Paris region II and the stable tearing crack growth region III.

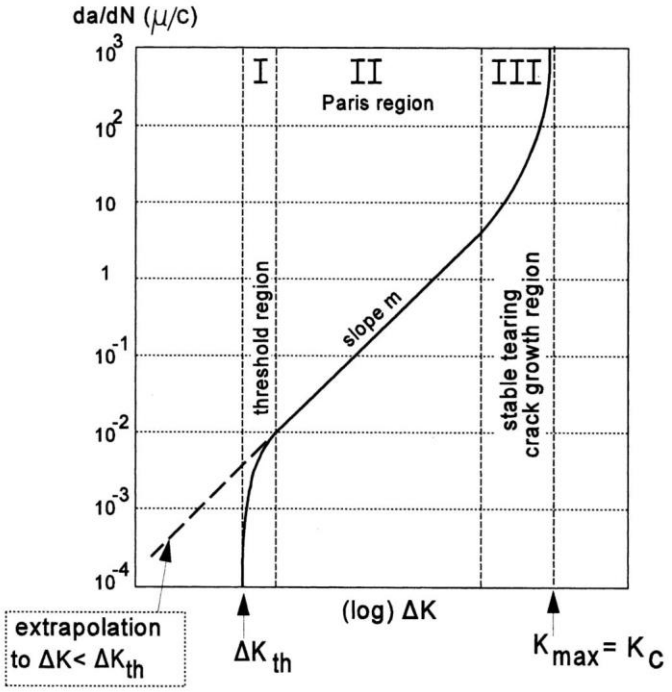

Figure 2.5: Plot of the Paris-Erdogan equation separated in three regions of the crack growth rate [Schi09]

The threshold region describes the lowest range of stress intensity factor under which macro crack growth take place. Below a threshold value ΔK_{th} the crack propagation is zero. In the Paris region the crack growth curve shows a linear behaviour with an approximately constant slope *m*. Whereby the Paris formula does not account fully for effects of the stress ratio *R* on crack growth. In the stable tearing crack growth region, the crack growth rates are high and cannot be described by a straight line. The stress intensity factor at which the final failure takes place is called K_c [Fric17] [Schi09].

2.6 Material zones in a weldment

The fracture toughness is mainly determined by the local microstructure of the material adjacent to the crack tip and the stress state. Therefore, for the investigation of fatigue properties, it is important to note that weldments do not have a uniform microstructure. General, weldments can be separated in 3 different material zones. First, the base material (BM), the microstructure is largely unaffected by the welding process. Secondly, the weld material (WM), this area consists of the filler material and melted material of the welded parts. Additionally, there is the heat affected zone (HAZ), in this 2–5 mm wide zone between the BM and the WM, the microstructure is affected by the heat influx of the welding process and the subsequent cooling process, see Figure 2.6. [Zerb14]

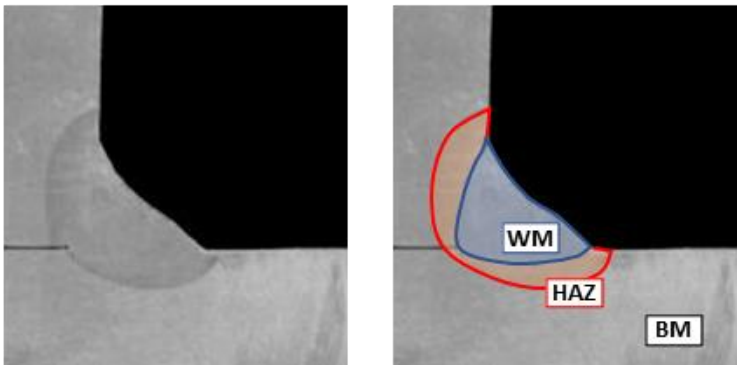

Figure 2.6: Different material zones in a weldment

The HAZ has been subjected to varying degrees of heat influx, which means that the HAZ cannot be described as a uniform material, the HAZ consists again of a range of microstructures, see Figure 2.7. The microstructures have a high, strongly varying influence on the fracture toughness, which can be both inferior and superior to that of the BM. [Zerb14]

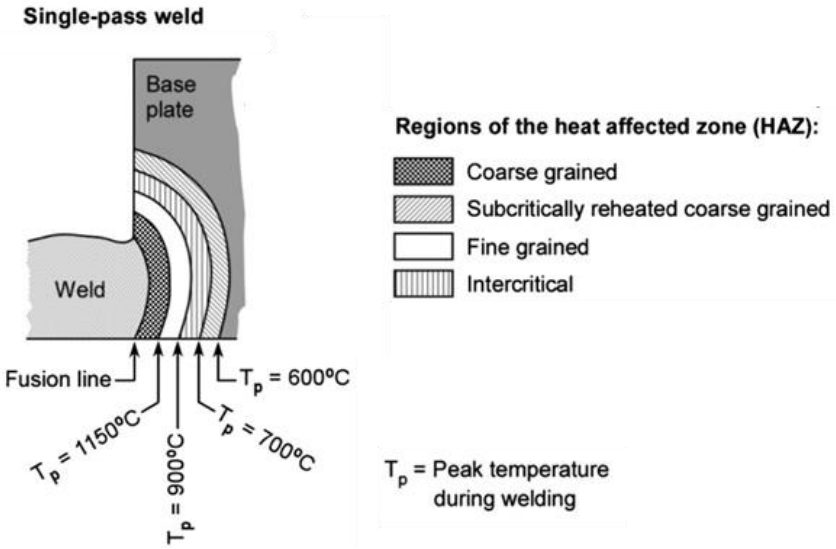

Figure 2.7: Schematic representation of different microstructures in the heat affected zone [Zerb14]

2.7 Influence of the weldment geometry

In this thesis, the fatigue properties of C-joints and transversal stiffener and failure location of C-joints are examined. These properties are dependent by the material factors, e.g. the microstructures and material failures like slag inclusions, pores, lack of fusion and cracks [Fric17]. Besides this, the fatigue properties are influenced by the weldment geometry, there are axial and angular misalignments but the central influence factor is the configuration of the geometry parameters. The fatigue properties are determined by the local dimensions of the weld, the unwelded gap between the parts and also by the plate thicknesses. For the dimensioning of C-joints, it is important to estimate whether a configuration will lead to a failure at the weld root or at the weld toe. For this reason, MADDOX has developed transition curves at which a crack is equally likely to occur at the weld root and the weld toe [Madd74]. The curves are derived from the S-N curves of experimental data and are determined by the plate thickness *2*b*, the weld width *c* and the length of the unwelded area *2*a*. In Figure 2.8 by FRICKE the

transition curves are shown [Fric13]. It should be noted that in the further part of the thesis a different nomenclature is used to describe the weld geometry.

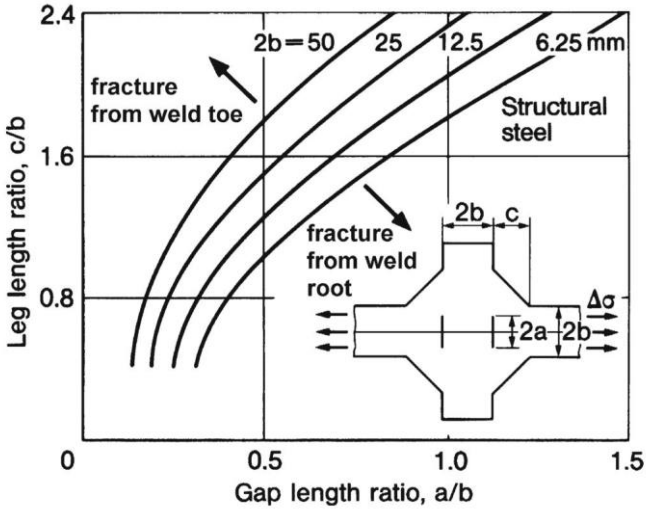

Figure 2.8: Limit curves separating fracture from weld toe and root in cruciform joints [Fric13]

2.8 Fatigue at sub-zero temperatures

The fatigue crack growth (FCG) of ferritic steels is decreasing together with the temperature until a so-called fatigue transition temperature (FTT) is reached. The FTT defines the point at which the fatigue ductile-brittle transition (FDBT) takes place, stable crack growth behaviour changes from plastic blunting and tearing to cleavage-controlled brittle fracture, which leads to a sharp increase of the FCG rate [Brau20a]. This behaviour is the result of two competing mechanisms. On the one hand, as temperature decreases, the stress required to activate mobile dislocations increases and crack tip opening displacement decreases. On the other hand, as temperatures decrease, ''static'' modes of crack propagation are activated, such as the micro cleavage cracking. The FTT indicates the point at which the mechanisms facilitating the FCG are dominant. It should be noted that starting from a peak near room temperature (RT), the fracture toughness of ferritic steels decreases consistently with temperature, with the temperature induced toughness decrease showing high scatter [Akse17]. The mechanism of FDBT is linked to the body-centred cubic crystal structure of ferrite. This effect does not occur, for example, in the body-centred tetragonal crystal structure of martensitic steels [Oh15]. The Charpy V-notch impact test is widely used to determine the brittleness of steels. This test investigates the impact energy at which a standardised specimen break. In reference to the relationship between temperature and brittleness, the Charpy V-notch impact test looks for the temperature at which the material will break at an energy of 27J (for steels with higher toughness 50J is used), the symbol is T_{27J} (T_{50J}). This temperature is defined as the ductile-brittle transition temperature (DBTT). A correlation can be assumed between the FTT and the DBTT, which is that the FTT of a material is around 15°C - 20°C below the DBTT [Alva17].

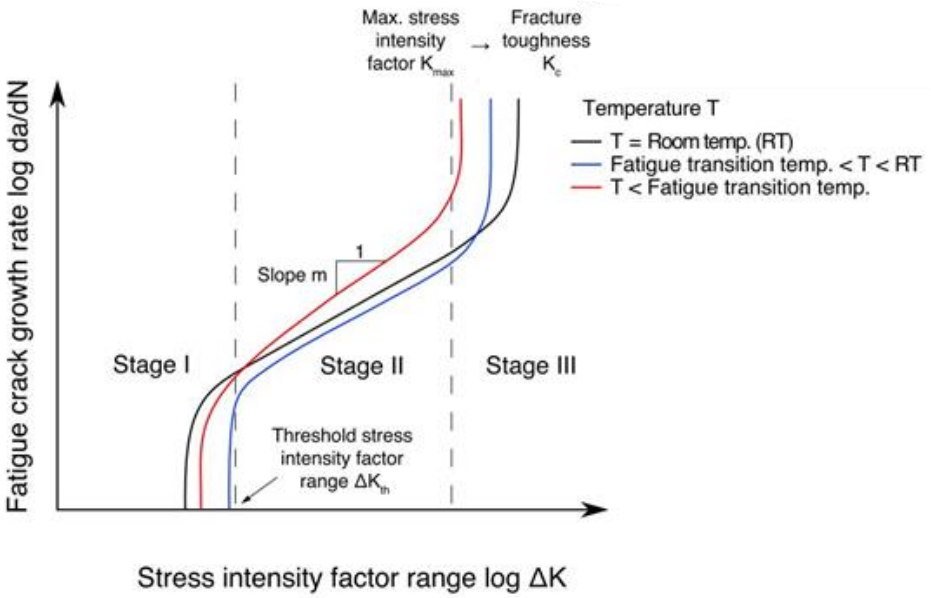

Figure 2.9: Schematic representation of fatigue crack growth behaviour below and above the FTT temperature when compared to RT [Brau21a]

The FCG rate in the linear Paris region is of particular importance for the fatigue life. The comparison of the curves in Figure 2.9 at RT and the curve below the RT but above the FTT shows that the slope in the Paris region does not change, only a decrease of the FCG rate takes place. In contrast, the curve below the FTT has a steeper slope and consistently larger, more detrimental FCGR.

3 Test setup and specimens

The aim of this thesis and therefore also the experiments is to determine the fatigue life of C-joints and transversal stiffeners to generate measurement data to verify simulation models. The required experiments are conducted on a resonance type fatigue testing machine, wherein clamping chucks and specimen are separated by a climate chamber from the environment that allows the control of the experiment temperature. In the following, the individual elements of the experiment will be described.

3.1 Specimens

In the experiments two types of welding are examined, cruciform joints with nonpenetrating fillet welds and two-sided transverse stiffeners. Depending on the type of the welding is the crack location, while transversal stiffener always fail at the weld toe, C-joints can either fail at the weld toe or the weld root. The distribution between these two failure locations, according to the current research stand, is mainly determined by the geometric dimensions of the welding and the welded plates, see e.g. [Fric13]. Because of the examined weldments and the incomplete penetration, it can be assumed that the C-joints will fail at the weld root. In Figure 3.1 polished and etched macrographs of specimens are presented together with a schematic sketch to indicate the possible failure locations.

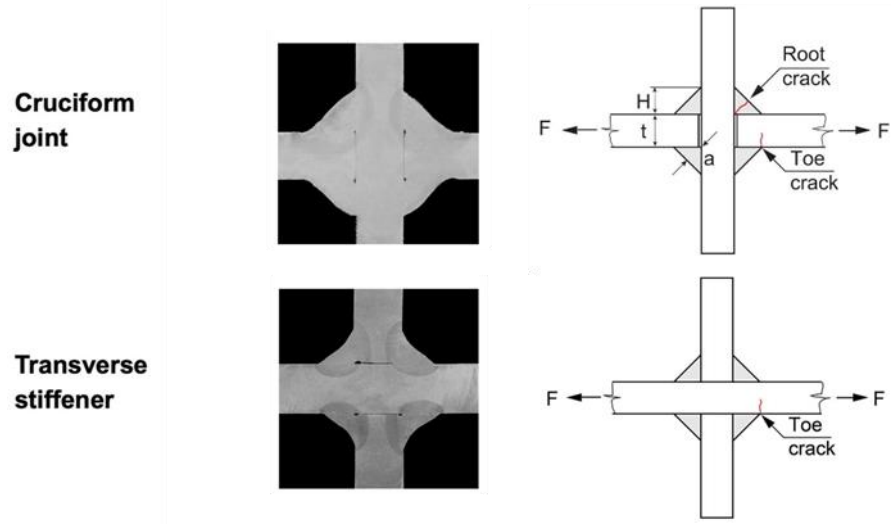

Figure 3.1: Polished and etched macrographs of the weldments with sketches to indicate failure locations [Brau20a] [Brau20b] [Brau21a]

In order to exclude material-related uncertainties on the specimens two different steel grades are examined. On the one hand S235J2 + N and on the other S500G1 + M, the Youngs modulus

and the Poisson's ratio is for both steel grades identical E = 206 GPa, v = 0.3. The chemical compositions can be seen in Table 3.1.

Table 3.1: Chemical composition of S235J2+N and S500G1+M used [w%]

	C	**Si**	**Mn**	**P**	**S**	**N**	**Cu**
S235J2+N	0.107	0.176	1.02	0.014	0.001	<0.001	0.016
S500G1+M	0.056	0.208	1.58	0.012	0.002	0.004	0.273
	Mo	**Ni**	**Cr**	**V**	**Nb**	**Ti**	**Al-T**
S235J2+N	0.002	0.020	0.023	0.001	<0.001	<0.001	0.041
S500G1+M	0.175	0.516	0.056	0.001	0.020	0.001	0.033

Another for this thesis relevant material characteristic is the DBTT, to be able to consider the influence of brittle material behaviour. The DBTT is determined by Charpy testing and is specified in the form of the T_{27J} for S235 and the T_{50J} for S500. For both materials Charpy test have already been carried out by BRAUN et al., he also used the same welding technique for his specimens [Brau21b]. However, the comparability of this data is limited by the fact, that he investigated butt-welded joints, which are composed of multiple weld layers and thus repeated heat influx. In addition to the investigation of the BM BRAUN et al. also carried out Charpy tests for material in the HAZ and the WM, his results are depicted in Table 3.2 [Brau21b].

Table 3.2: Results of the Charpy notch impact testing [Brau21b]

		BM	**HAZ**	**WM**
S235J2+N	T_{27J}	-78°C	-79°C	-28°C
S500G1+M	T_{50J}	-119°C	-85°C	-39°C

The distinction in different material areas is useful to consider the differences in the material properties during crack growth. While the crack propagation for the weld root failure takes place completely through WM, starts, for the weld toe, the crack initiation in the conjunction location between weldment and HAZ and is extending from HAZ in the BM [Song21]. According to ZERBST et al., the HAZ consists of several subregions with different microstructures and therefore material properties [Zerb14], see Section 2.6. The differences in the material properties, especially the fact that the extent of the subregions and their borders are not clear make it difficult to consider the HAZ. For simplicity, it is therefore assumed that the crack propagation is completely carried out through the BM and the HAZ will not be considered further in this work.

The specimens have been made of 3 steel plates and connected over single-layered welds. The used welding technique is the flux cored arc welding. For the welding process, a 1.2 mm diameter Outershield 71E-H wire is used in the S235 material and a stone megafil 821r wire for the S500 material. The resulting plates have dimensions of 1000 mm x 500 mm with a plate thickness of 10 mm, see Figure 3.2. The specimens are produced by cutting the plates with a hydraulic saw in pieces of 50 mm width by a length of 500 mm, after the sawing process the specimens are deburred [Brau20a].

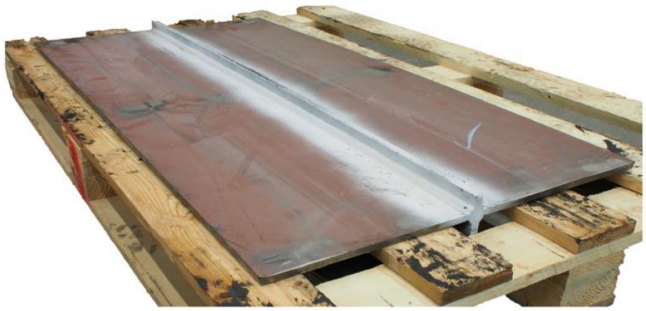

Figure 3.2: Welded plate before sawing [Brau20a]

3.2 Measurement devices for the specimen geometry and adjustment

During the manufacture process of the specimens, position deviations of the parts, heat influx, measurement inaccuracies and changing welding parameters occur and are causing misalignments. In order to allow comparability of the results of these different specimens, correction factors must be determined. These correction factors should compensate secondary bending effects on the stress which emanate from angular misalignment ϕ and axial misalignment e, see Figure 3.3. On the other hand, fatigue tests are influenced by the local geometry of the weldment, to classify the results, these must also be known [Brau21a].

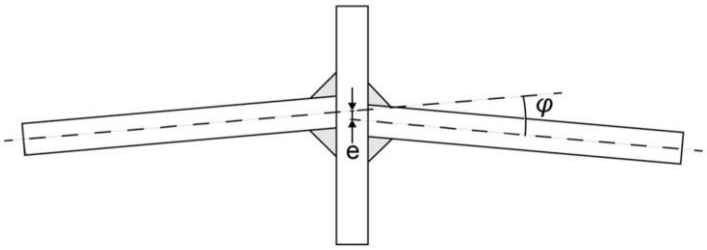

Figure 3.3: Sketch of a C-joint to indicate the two types of misalignment [Brau20a]

To measure the misalignments, two dial gauges are used in a measuring setup according to FISCHER, the calculation takes place based on a principle developed by BRAUN, see Figure 3.4 [Fisc16] [Brau21a]. The specimen is aligned with variable support beams and fixed supports within the measuring structure and lie on the points h_1 and h_4. The dial gauges are at the points h_2 and h_3 and measure the vertical deflection [Brau21a].

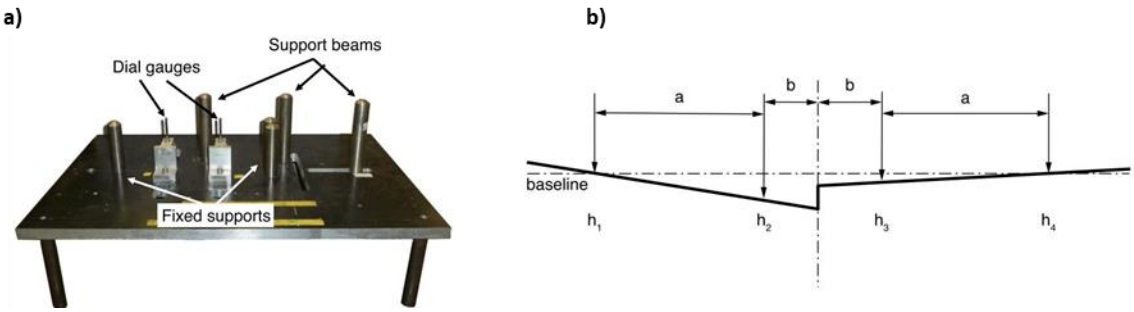

Figure 3.4: Misalignment measurement setup (a) and principle to determine axial and angular misalignment (b) [Brau21a]

In order to consider the misalignment effects, a resulting stress magnification factor k_m is determined that appropriate procedures is shown in the IIW Recommendations, see [Hobb16]. The stress magnification factor k_m consists of an axial part $k_{m,e}$ and an angular part $k_{m,a}$. The full presentation of the calculation formulas is not relevant for this thesis and will be dispensed for further information it is referred to the IIW Recommendations from HOBBACHER [Hobb16]. However, it should be noted that the clamping effects are not taken into account in these formulas, therefore the resulting secondary bending stress effects can be slightly overestimated [Brau21b]. The central equation to calculate the magnification factor k_m is:

$$k_m = 1 + (k_{m,e} - 1) + (k_{m,a} - 1) \tag{3.1}$$

In addition to the measurement of the vertical deflection with dial gauges, the width and height of the load-carrying plates is determined with a calliper gauge. This is necessary, because for the experiments machines loads have to be set, for this the stress must be known in the specimen area.

The principle of laser triangulation is used to measure the local weld geometries, using a laser scanner mounted on a single-axis system. Before the scan can start the specimen has to be prepared. In a first step the welding is cleaned with a brass brush, universal cleaner and cleaning wipes. In a second step the welds have been sprayed with a lime spray to allow a diffuse scattering of the laser beam. For the measurement of the weld, the system is placed in a fixed distance to the specimen and then the laser drives at a defined speed over the axis length, see Figure 3.5. The laser scanner creates a fixed number of pictures each second and is measuring the whole local geometry on this way. After completing the scan, the point cloud, each point is defined by its x-y-z-coordinates, is saved as an ASCII file. From this file, the weld geometry is created due the curvature method by SCHUBNELL et al. and the geometric parameters of the welding can be processed [Schu20].

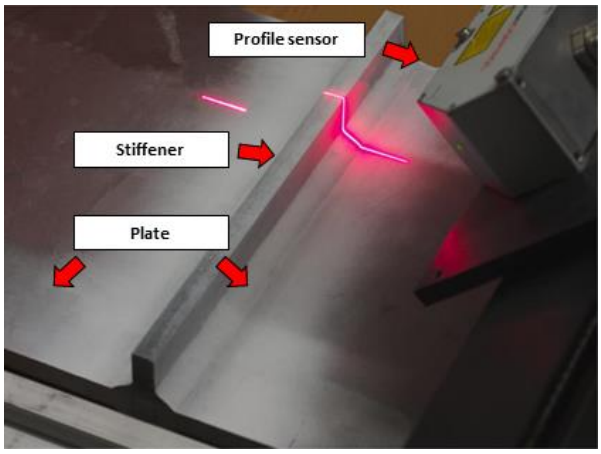

Figure 3.5: Laser scanning of a specimen with a thin layer of chalk [Renk21]

3.3 Test setup of fatigue tests

For the experimental determination of the fatigue behaviour resonance type fatigue testing machine are used. A specimen is applied with a cyclic load under a constant amplitude, the number of cycles to failure, i.e. rupture of the specimen, is measured. For this data of the whole S-N cycle, high and low cycle fatigue, have to created. In addition, sufficient number of

measuring points are needed to be able to form the scattering area of the specimens [Fric17]. For the experiments, a Schenck Horizontal Resonance Testing Machine with maximum load capacity of 200 kN and a frequency around 33 Hz is used. For the sub-zero experiments the resonance testing machine is adapted with a climate chamber that separate clamping chucks and specimen against the environment. The climate chamber allows it to set a temperature range between -180°C to 280°C. The cooling of the climate chamber is done by injecting vaporized nitrogen from a tank into the climate chamber. The temperature is continually measured by a PT100 platinum measuring resistor, based on the chamber temperature output, the injection of the nitrogen is controlled. With this setup a constant chamber temperature around ±1°C can be maintained. Since the temperature within the chamber is not identical to the specimen temperature, another PT100 platinum measuring resistor is attached with a magnet on the specimen. The temperature thus measured is used for the experimental setting and evaluation. In Figure 3.6 (a) the complete setup and in Figure 3.6 (b) the climate chamber with clamped specimen and PT100 platinum measuring resistor is shown.

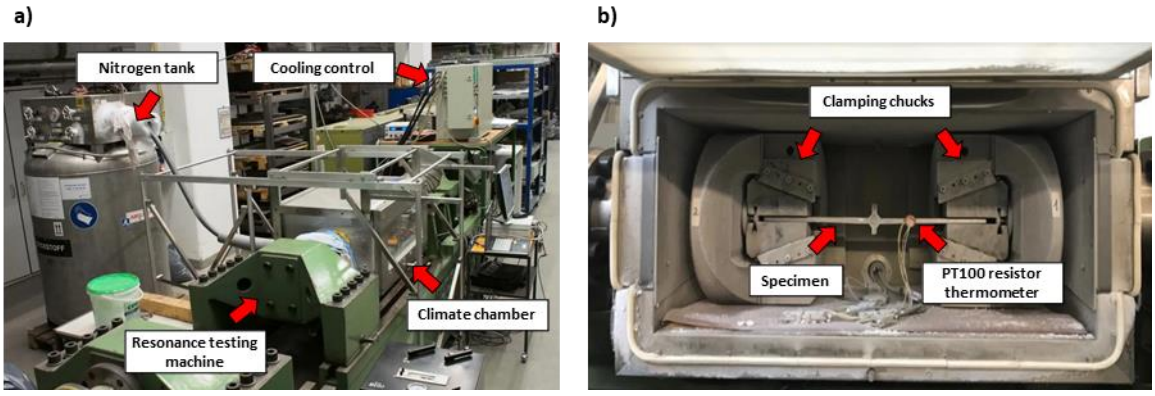

Figure 3.6: Whole experimental setup [Sall20] (a) Climate Chamber [Brau20a] (b)

4 Setup of numerical models to determine fatigue crack growth

Before simulation models can be created, the basic object of investigation must be determined, i.e. what are the question to be answered with the simulation model. This definition has already taken place in the introduction, see Section 1.2. The aim is to predict the fatigue life and the failure location of C-joints and transversal stiffeners, whereby the failure location is only relevant for the C-joints. In the models, the material behaviour must be considered depending on the temperatures, in particular around the FTT.

Based on this definition, a suitable fatigue simulation approach has to be selected and after that the used simulation tools. Simultaneously, verification conditions must be set up, based on established literature, e.g. the IIW Recommendations from HOBBACHER [Hobb16]. Subsequently, the simulation models are created, while used simplifications and specified parameters, e.g. initial crack length or number of elements, has to be named and justified. The validity of the models must be confirmed on the basis of conditions to be set up.

4.1 Selection of a fatigue strength assessment approach

There are two general sets of procedures for non-experimental fatigue assessment. Procedures based on S-N curves which show the relationship between the number of load cycles and stress parameters. Examples for this group are: Nominal stress approach, structural hot spot stress approach and the effective notch stress approach. The second group of fatigue assessment approaches is based on fracture mechanics and uses crack growth curves, following propagation laws like Paris-Erdogan [Fric13] [Hobb16].

The crack propagation approaches define an initial crack and allows to evaluate the crack growth behaviour until the final crack length is reached. Approaches based on S-N curves do not need initial cracks but can only consider one stress value. Whereas the crack propagation approach considers the whole stress field [Fric13]. With regard to the special case of welded joints, the crack propagation approach has the advantages, that the crack initiation phase is short due to the relatively sharp notches, weld imperfections and non-fused root faces [Fric17] [Al-M10]. Another selection criterion in this thesis is the prediction accuracy of the fatigue assessment approach under sub-zero temperatures. This question is answered in a study BRAUN et al. [Brau20b]. An experimental study shows that there are large differences between the predicted and the experimental results for procedures based on S-N curves. The deviations are related to the fatigue life span and the distribution between the failure locations [Brau20b]. The influence of the temperature on the material behaviour is described by the C

and m values in the Paris-Erdogan formula, see [Alva14]. Therefore, a crack propagation approach is used in following study.

4.2 Selection of tools for a fracture mechanical study

For a fracture mechanical study based on the crack propagation approach, a geometric model and the associated mesh of the area to be investigated is needed. In this model, the boundary conditions are defined, i.e. material properties, stresses and bearing points. Subsequently, an initial crack is added to the model with a finite element method (FEM) program and the iterative growing of the crack is simulated with this program. An iterative crack growth step is defined by a constant crack step size *da*. For each step the SIFs are calculated and stored. Together with the *C* and *m* parameter, the SIFs are used to solve the Paris-Erdogan equation. From this *da/dN* solutions the resulting fracture life, i.e. the number of constant cyclic loads until the specimen breaks N_f, is determined. For C-joints, there are two possible failure locations, the critical locations characterized by the lower number of constant load cycles.

In this thesis, the failure of existing specimens should be emulated, these specimens show differences in their geometry, see Section 3.2. Because of the high number of different geometries, it is time-consuming and error-prone to create them individual. In addition, it is difficult to produce a similar mesh, this reduces the comparability. Instead of the manual creation a parametric approach can be used.

With the program Ansys mechanical APDL complete FEM simulations can be done, however it is not suitable for the crack propagation approach that is followed. In this thesis the program should only be used to create geometric models, the input for another, specialised FEM software. The control of Ansys mechanical APDL can be done via the command line, this made it possible to run the program with external created scripts, i.e. .txt files. For this purpose, scripts are generated that contain the Ansys commands to create geometric models of welds, the mesh and boundary conditions. The geometry and the mesh are dependent on a small number of variables, by changing them all necessary models can be generated. The corresponding scripts with the adapted variables are generated in MATLAB, the values for the variables are adopted from the evaluated measurement results, see Section 3.2.

The crack propagation approach can be performed for both 2D and 3D models. The 3D models enable the simulation of different crack fronts, while in 2D models can only be simulated straight crack fronts, this is particularly relevant for weld toe failure, see Figure 4.1 [Fisc12]. More about the reasons and impacts of the crack front in the following Section 4.3.2. However, the 3D models have the disadvantage that their complex geometry is much more difficult to create in general and especially as a parametric model. However, FISCHER and FRICKE show that by adapting the geometry function and the *a/c* ratio, defining the length and depth of the crack front, the SIFS of 2D models can be modified subsequently [Fisc12]. Therefore, 2D models are used in this thesis.

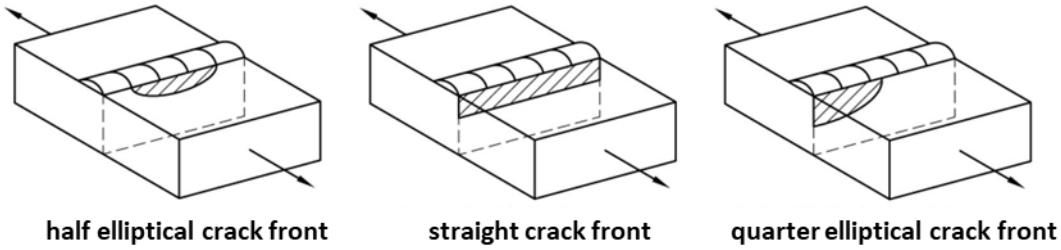

Figure 4.1: Different crack fronts in butt-welded joints [Fisc12]

For the numerical calculation of the SIFs the software Franc2D, developed by Cornell University Fracture Group, is used. In Franc2D an initial crack has to be defined. After that it uses the crack propagating approach, based on J-integral techniques, to calculate stress intensity factors for the growing crack. The results of the programme are provided in tabular form and can be saved, for example, in a .txt file. The results are then imported to MATLAB, linked with the associated metadata and used to calculate the fatigue life via Paris-Erdogan. Simultaneously, the analytical result for the corresponding geometry is calculated in MATLAB, this allows the Validation of the numerical results. Besides the creation of parametric scripts and the calculation of the fatigue life, MATLAB serves as the central control program, in which all other programs are embedded. By MATLAB the programs are invoked, inputs done and files transmitted. This serves, in addition to the reduction of the effort, the avoidance of random errors, which cannot be detected later in the project, e.g. insert similar values from the wrong line. The simulation procedure is shown in Figure 4.2.

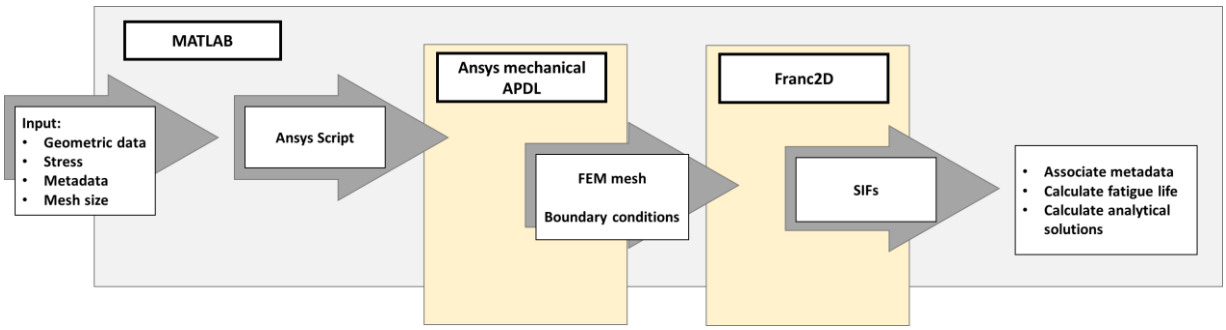

Figure 4.2: Simulation procedure of fatigue crack growth

4.3 Creation of analytical solutions

There are universally accepted international codes and recommendations on the subject of weldments, such as the IIW recommendations or BS7910 [Hobb16] [Brit15]. In these publications, formulas, including their scope, are described with which SIFs can be calculated analytically. By calculating the same load case via analytical formulas and numerical simulations, the validity of the numerical results can be confirmed or rejected. Wherein is to emphasize that the accordance of numerical and analytical results confirms only the validity of numerical results within the scope of the analytical formulas. Therefore, in the selection of the analytical formulas, it is important to pay attention to their accordance with the real case.

In this section the analytical formulas, for the three investigated failure locations, weld toe failure at C-joints and transversal stiffener and weld root failure at C-joints, are formulated.

An exemplary geometry for each case is defined, appropriate formulas for the cases are selected and the SIFs are calculated. After the analytical the corresponding numerical case is calculated and the two solutions are compared with each other, in this section.

For the crack propagation approach the IIW recommendations as well as the BS7910 suggest specific values for the selection of some parameters used in the calculation, e.g. the initial crack size a_i or aspect ratio a/c [Hobb16] [Brit15]. In addition, there are publications that deal with the selection of better appropriated parameters or indicate to them, e.g. ENGESVIK and MOAN regarding a formula describing an aspect ratio [Enge83]. The parameters can have a great impact on the results, their selection is not trivial and they are justified when necessary.

At this point, the parameters are introduced that are identical for all three failure cases. In Figure 4.3, selected geometric parameters and the stress range $\Delta\sigma$ are shown. Here, H describes the weldment height, W the weldment width, T the thickness of the loaded plate and t the thickness of the unloaded plate. The selection of the parameters described in this paragraph are subject to few restrictions except that they must be in the scope for the analytical formulas. The selected parameter values are shown in Table 4.1.

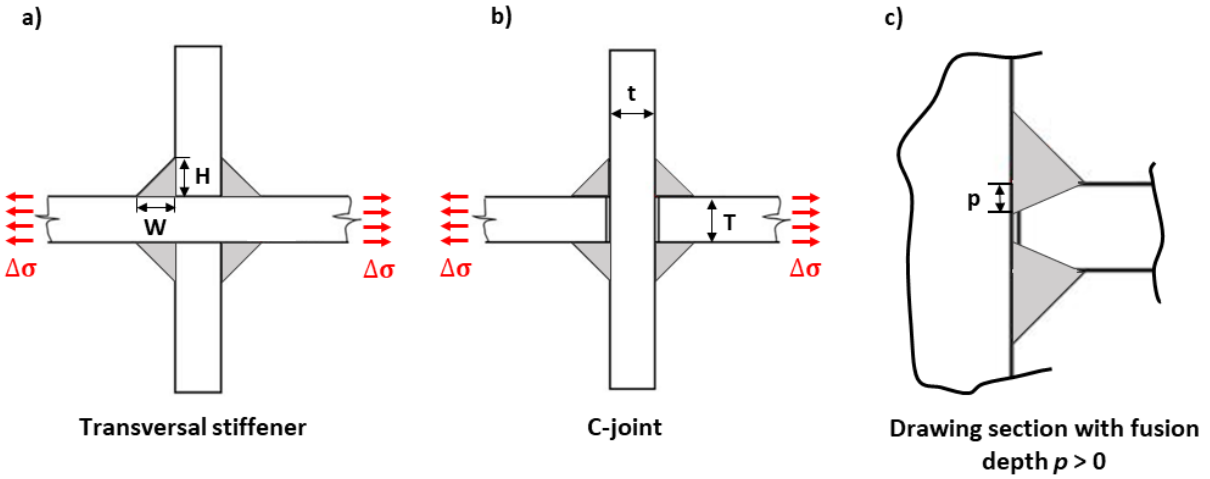

Figure 4.3: Sketch of a transversal stiffener (a), a C-joint (b) and a drawing section $p > 0$ (c) with geometric parameters, graphic representation according to [Brau20a]

For the specimens, it is assumed that there is no fusion under the weldment. Therefore, the fusion depth is $p = 0$ but to illustrate this parameter in Figure 4.3 (c) a drawing section with a fusion depth greater than zero is shown. For the crack propagation approach an initial crack with the initial crack depth a_i has to exist. In the calculations the crack propagates stepwise through the material until it reaches a final crack depth a_f at which the final failure occurs. For these calculations the value for the initial crack depth has a great impact on the results, because the biggest part of the fatigue life takes place at short crack lengths.

In the IIW Recommendations, considerations have taken place to the transition from the phase of micro crack growth to the macro crack growth, eventually an initial crack depth of $a_i = 0.1$ mm is suggested [Hobb16]. For the appropriate selection of this value, comprehensive investigations can be carried out, due to the scope of this work the suggested value is taken over in the first place. If the results shows that the initial crack depth of a_i is not suitable, further investigations will be done.

The final failure occurs, if the stress intensity factor K_I is bigger than the fracture toughness K_{Ic}, with exceeding the crack reaches the final crack depth a_f. For the calculation of the SIFs the final crack depth is needed as stop criterion. The fracture toughness is a material property and dependent on the ambient temperature. From this dependency WALLIN created mean curves to describe it, the determination is codified in ASTM E1921-21 [Wall99] [ASTM03]. The formula is:

$$K_{Ic,median} = 30 + 70 * exp(0.019 * (T_{exp} - T_{100})) \quad (4.1)$$

Where:

$K_{Ic,median}$ = Estimate of fracture toughness via master curve [MPa√m]

T_{exp} = Test temperature [°C]

T_{100} = Temperature for a median toughness of 100 MPa√m [°C]

To obtain the temperature, at which the median toughness is 100 MPa√m, the Sanz-correlation can be used. This describes a correlation between the results of Charpy impact tests T_{27J} and the T_{100} value [Lang19]. The formula is:

$$T_{100} = T_{27J} - 18°C \quad (4.2)$$

From experiments by BRAUN et al., T_{27J} values for the S235 and S500 steels are available [Brau21b]. The calculation of the final crack depth a_f is connected with a computational effort, whereby the final crack depth is only needed as stop criterion. Since the majority of the fatigue life takes place during the growing of short crack lengths, the final crack depth is less significant. Therefore, an alternative stop criterion described in the IIW Recommendations can be used, it stipulates that the final failure occurs after half plate thickness for failure at the toe [Hobb16]. For means of simplicity the IIW is used and is set to a_f = 5 mm for failure at the toe. The problem with the final crack depth for the failure at the root is that the crack is not propagating perpendicular to the surface of the weld. Therefore, the extreme case is used that the crack growth is perpendicular to the load case and the final crack length is set half height of a weldment a_f = 4 mm, when H = 8 mm. This assumption is based on the observation by KAINUMA and MORI that for fatigue cracks originates from the weld root the direction approximately perpendicular to the applied load and so coincided with that of the unwelded gap [Kain06].

Table 4.1: General parameters – used for all failure cases in this thesis

H	8 mm	$\Delta\sigma$	100 MPa
W	8 mm	p	0 mm
T	10 mm	a_i	0.1 mm
t	10 mm	a_f	5 mm / 4 mm

4.3.1 Cruciform joint – weld root failure

For C-joints with the failure location at the weld root, the crack is initiated due the non-welded gap between the plates and propagates from the through the weldment until it comes to the final failure. The non-welded gap affects the fatigue behavior like an initial crack. Therefore,

the initial crack is half the thickness of the loaded plate a_i = 5 mm and the final crack length is $a_f = a_i + a_f$ = 9 mm. The non-welded gap has a straight crack front. In the BS7910, the following analytical formulas are given for the failure described [Brit15]:

$$M_k = \lambda_0 + \lambda_1 * \left(\frac{2a}{T+2H}\right) + \lambda_2 * \left(\frac{2a}{T+2H}\right)^2 \tag{4.3}$$

$$M = 1 \tag{4.4}$$

$$\lambda_0 = 0.956 - 0.343 * \left(\frac{W}{T}\right) \tag{4.5}$$

$$\lambda_1 = -1.219 + 6.21 * \left(\frac{H}{T}\right) - 12.22 * \left(\frac{H}{T}\right)^2 + 9.704 * \left(\frac{H}{T}\right)^3 - 2.741 * \left(\frac{H}{T}\right)^4 \tag{4.6}$$

$$\lambda_2 = 1.954 - 7.938 * \left(\frac{H}{T}\right) + 13.299 * \left(\frac{H}{T}\right)^2 - 9.541 * \left(\frac{H}{T}\right)^3 + 2.513 * \left(\frac{H}{T}\right)^4 \tag{4.7}$$

The SIF can be calculated via the already introduced formula:

$$\Delta K_I = \Delta\sigma * \sqrt{\pi * a} * M_k * M \tag{4.8}$$

Beginning with the initial crack depth the SIFs are calculated in an iterative step width of *da* = 0.1 mm, see Figure 4.4.

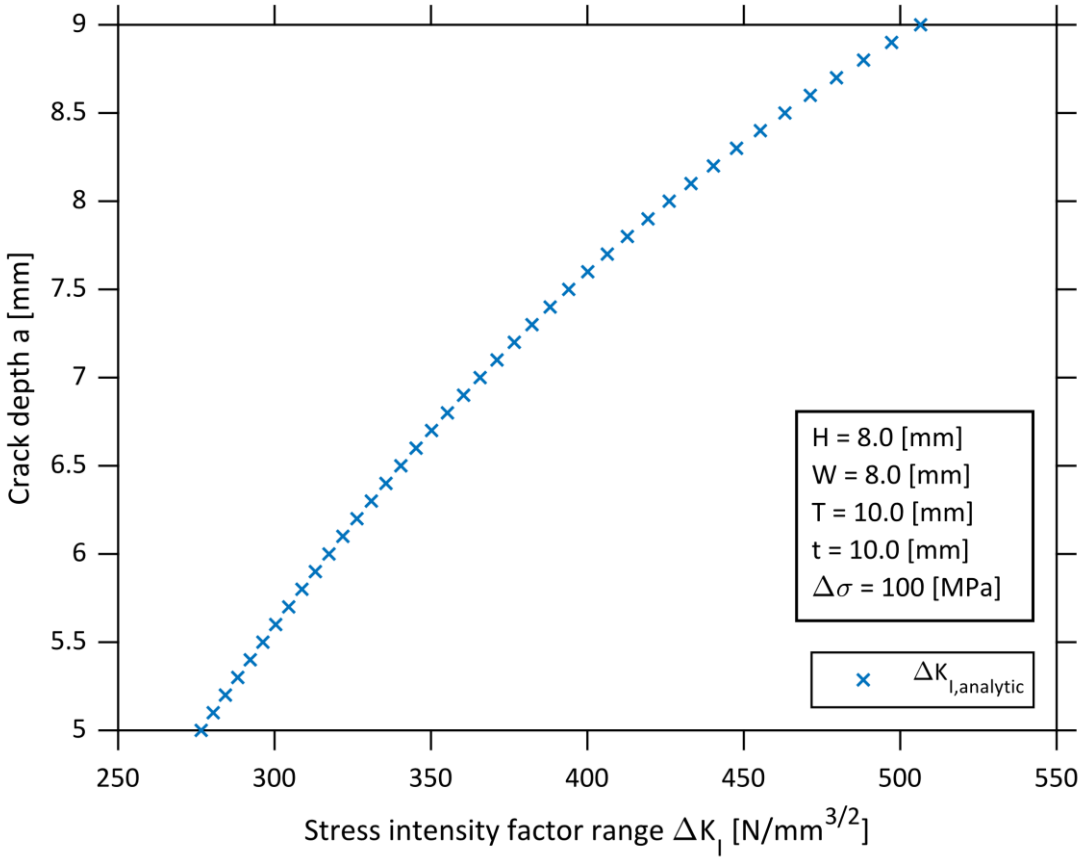

Figure 4.4: Analytical calculated SIFs for a C-joint with failure at the root

4.3.2 Transverse stiffener – weld toe failure

The force path in the C-joint, from the plates through the welds and the fastening is much more complicated than that of the transversal stiffener with failure at the toe. Therefore, the procedure for the transversal stiffener is described first. Compared with the failure at the root, the failure of C-joints and transversal stiffeners at the toe is fracture mechanical also more complicated. The reason is that the macro crack growth does not start with a straight crack front, like the non-welded gap between the plates at the C-joint. The straight crack front allows to neglect the 3rd dimension, the crack width *c*. This is not possible for a realistic analytical calculation of the toe failures because the crack starts at one or multiple points, they grow in a semi-elliptical shape at first and after a specific crack depth they unify to an approximately straight crack front. Therefore, the analytical calculation has to take place in the 3D space and not in the 2D space. In the 3D calculation alongside with the crack depth *a* the crack width *c* have to be considered. But the numerical calculations of crack growth are conducted with the 2D FEM program Franc2D but this program is not able to consider the 3D effects. The numerical results can only be validated with 2D analytical SIFs. Even if, it has to be expected that the 2D analytical case is more inaccurate than the 3D analytical case in depicting the experimental results. However, FISCHER and FRICKE have shown that a subsequent modification of the numerically calculated SIFs, with a 2D FEM program, via the 3D geometric functions is in principle possible [Fisc12]. Therefore, after the 2D analytical calculation of the SIFs, the SIFs are calculated additionally for the 3D case. If the 3D SIFs are much closure to the experimental results, their geometric functions should be used to modify the numerical results.

The fundamental formula for the 2D and 3D case remains the same:

$$\Delta K_I = \Delta\sigma * \sqrt{\pi * a} * M_k * M \tag{4.9}$$

The differences between the 2D and the 3D analytical equations are contained in the definition of the M_k and M factor. The stress intensity magnification factor M is a weight function which results from the surface crack growth in a finite plain plate [Newm81]. For the 2D case this formula represents a straight crack in a plate, see Figure 4.5 (a), while the 3D case represents a semi-elliptical crack, see Figure 4.5 (b).

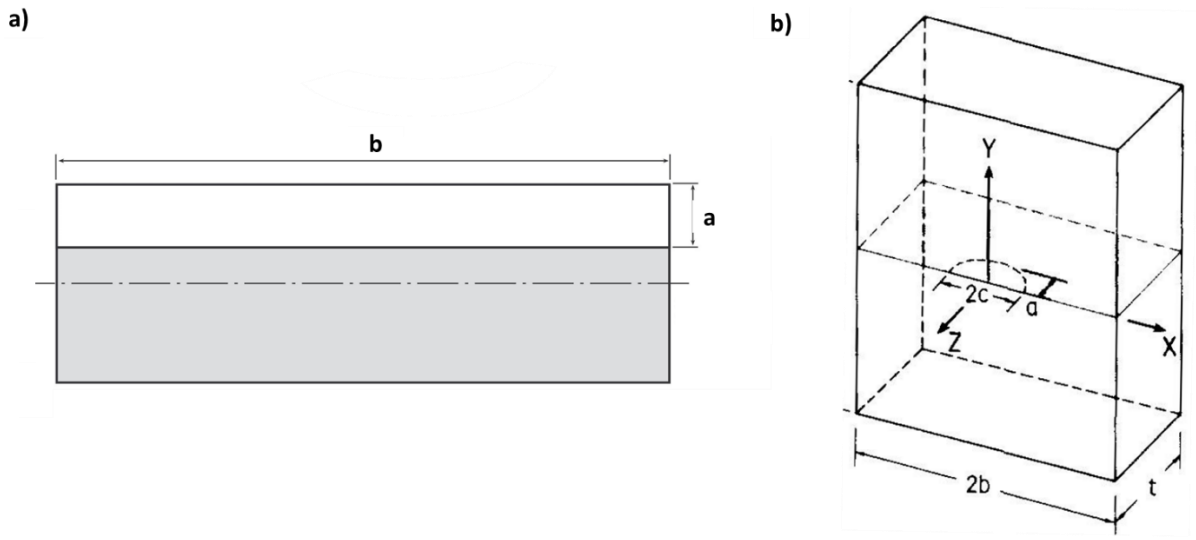

Figure 4.5: Surface crack in a finite plate – with a straight crack front [Brit15] (a) and a semi-elliptical crack front [Newm81] (b)

The stress intensity magnification factor M_k represents the influences of the weld geometry for the SIFs. The M_k factors can be determined both for the 2D case and the 3D case, see Figure 4.6. The 2D formulas are simpler but neglect influential effects, e.g. the aspect ratio *a/c*. The aspect ratio can be calculated by using the 3D M_k formulas, if this is not possible or not wanted, tabular values can be used, see for example the IIW recommendations [Hobb16].

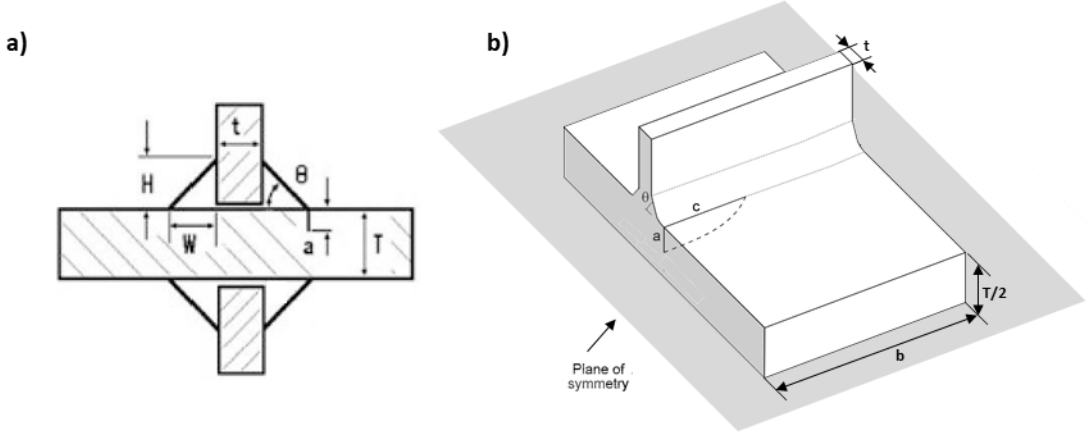

Figure 4.6: 2D transversal stiffener [Hobb16] (a) 3D transversal stiffener based on [Bown02] (b)

The formulas for the magnification factors M and M_k in the 2D case can be found in BS7910 and the IIW recommendations [Brit15] [Hobb16], their definition in BS7910 is:

$$M = 1.12 - 0.38 * \left(\frac{a}{T}\right) + 10.6 * \left(\frac{a}{T}\right)^2 - 21.7 * \left(\frac{a}{T}\right)^3 + 30.4 * \left(\frac{a}{T}\right)^4 \tag{4.10}$$

$$M_k = C_{Mk} * \left(\frac{a}{t}\right)^{k_{Mk}} \tag{4.11}$$

$$M_k \geq 1 \tag{4.12}$$

$$C_{Mk} = 0.8068 - 0.1554 * \left(\frac{H}{t}\right) + 0.0429 * \left(\frac{H}{t}\right)^2 + 0.0794 * \left(\frac{W}{t}\right) \tag{4.13}$$

$$k_{Mk} = -0.1993 - 0.1839 * \left(\frac{H}{t}\right) + 0.0495 * \left(\frac{H}{t}\right)^2 + 0.0815 * \left(\frac{W}{t}\right) \quad (4.14)$$

For the calculation of the analytical SIFs for the 3D case values for the crack width *c* or a relation like the aspect ratio *a/c* is needed. There are two possibilities to obtain these values either by calculating them or by using tabular values. The calculation of the *a* and *c* values based on an iterative approach, the calculation is more complicated but the iterative method has a higher accuracy and should therefore initially examined for its applicability to the scope of the thesis. The procedure is depicted in form of a flow diagram in Figure 4.7, it is based on BOWNESS and LEE [Bown02].

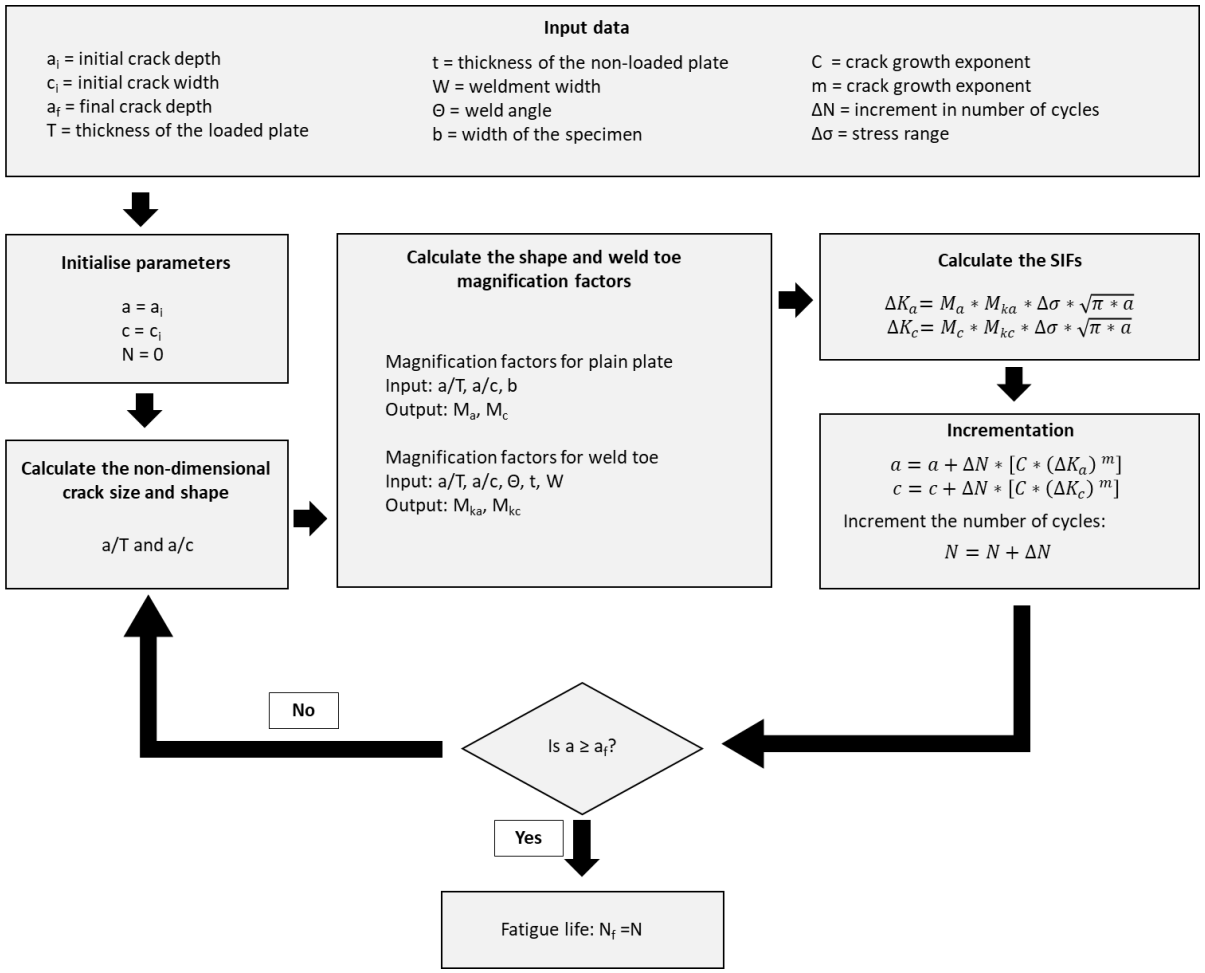

Figure 4.7: Procedure for iterative crack growth calculations of transversal stiffener, based on [Bown02]

The procedure of iterative crack growth according to BOWNESS and LEE, differs from others described in the IIW Recommendations by the fact that the iterations do not depend on a uniform leap in crack depth *da*, but from an increment based on a number of constant cycles *ΔN* [Bown02] [Hobb16]. Therefore, it is not possible to determine all magnification factors *M* and M_k first by using the geometry of the crack but it must iteratively calculate the SIFs and the crack lengths for each step before the factors for the next step can be calculated. Additionally, the *M* and M_k weight functions are separated in one set describing the deepest point of the crack M_a and M_{ka} and another set describing the SIFs at the surface M_c and M_{kc}, this increases

the number of necessary calculations. The procedure based on a constant cycle increment has the advantage that more calculations are done at crack length which have the greatest impact on the fatigue life, i.e. more calculations for small crack lengths because the majority of fatigue life takes place in this region, this increases the accuracy.

One aim of this thesis is to determine the effects of sub-zero temperatures on the fatigue life of the weldments, the change in the material behaviour due to the sub-zero temperatures is expressed by the adaption of the *C* and *m* parameters in the Paris-Erdogan equation. For the iterative procedure based on a uniform leap in cracking depth *da* only the *C* and *m* parameters have to be adapted and the SIFs are not changing. While for a *ΔN* increment the whole calculation of the SIFs has to be repeated for each adaption of the *C* and *m* parameters. This behaviour is very adversely with regard to the scope of this thesis. Despite of this, the calculations should be done with an increment of *ΔN* = 5000, first. The values for the *C* and *m* parameters are taken from the BS7910, they are *C* = 5.21e-13 and *m* = 3 [Brit15].

The formulas for the M_{ka}, M_c and M_{kc} can be found in Appendix A1. While the formula for M_a and its sub-parameters are shown here [Newm81]:

$$M_a = \left(M_1 + M_2 * \left(\frac{a}{T}\right)^2 + M_3 * \left(\frac{a}{T}\right)^4\right) * \frac{f_w * f_\Phi * g}{Q} \tag{4.15}$$

$$M_1 = 1.13 - 0.09 * \left(\frac{a}{c}\right) \tag{4.16}$$

$$M_2 = -0.54 + \left(\frac{0.89}{0.2 + \left(\frac{a}{c}\right)}\right) \tag{4.17}$$

$$M_3 = 0.5 - \left(\frac{1}{0.65 + \left(\frac{a}{c}\right)}\right) + 14 * \left(1 - \left(\frac{a}{c}\right)\right)^{24} \tag{4.18}$$

$$f_w = \sqrt{\sec\left(\frac{\pi}{2} * \frac{c}{b} * \left(\frac{a}{T}\right)^{0.5}\right)} \tag{4.19}$$

$$f_\Phi = \left(\left(\frac{a}{c}\right)^2 * \left(\cos\left(\frac{\pi}{4}\right)\right)^2 + \left(\sin\left(\frac{\pi}{4}\right)\right)^2\right)^{0.25} \tag{4.20}$$

$$g = 1 + \left(0.1 + 0.35 * \left(\frac{a}{T}\right)^2\right) * \left(1 - \sin\left(\frac{\pi}{4}\right)\right)^2 \tag{4.21}$$

$$\mathrm{Q} = \sqrt{\left(1 + 1.464 * \left(\frac{a}{c}\right)^{1.65}\right)} \tag{4.22}$$

Where:

f_w = finite width correction factor [Newm81]

f_Φ = an angular function from the embedded elliptical crack [Newm81]

g = correction factor depending on the crack depth and the position in the elliptical crack

Q = shape factor for elliptical crack [Newm81]

The factors f_w, f_Φ, g and Q are used to determine the SIF correction factor for a crack in a plane plate, considering the shape of the crack, the finite dimensions of the plate and the position within the crack at which the SIFs should be calculated. For the deepest point of the crack this position is $\Phi = \pi/4$, for the surface it is $\Phi = 0$. Regarding the validity of the correction factors M_a and M_c of NEWMAN and RAJU it has to be noted that $c/b < 0.5$, for a straight crack front $c = b$ this is not the case, the formulas are out of their verified range of validity [Newm81].

The results of the iterative calculation are plotted in Figure 4.8. The higher number of points at short crack sizes shows the influence of this area on the fatigue life.

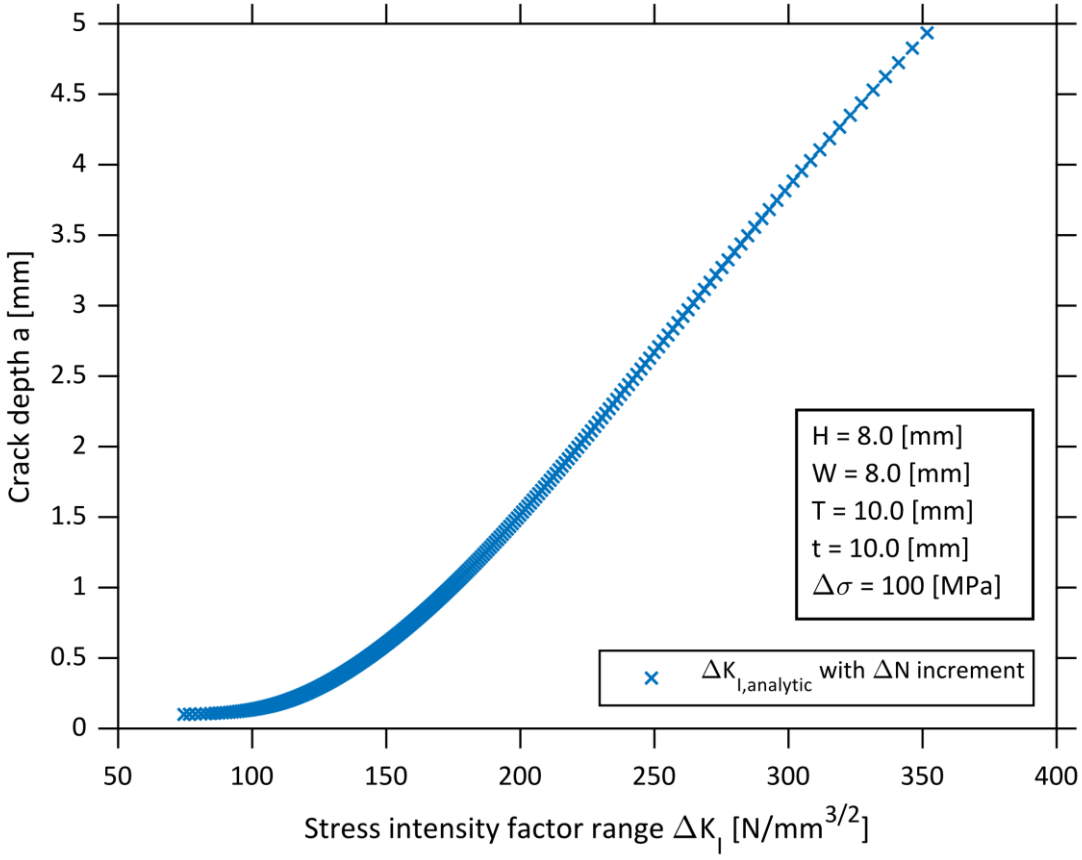

Figure 4.8: Analytical calculated SIFs for a transversal stiffener with ΔN increment

Because the use of the ΔN increment is not suitable for the scope of this thesis, in the following the applicability of tabular values for the definition of the aspect ratio a/c should be examined. The IIW Recommendations proposes several approaches for selecting aspect ratios. A conservative approach stipulates a constant aspect ratio of $a/c = 0.1$, another approach uses a variable aspect ratio. The variable aspect ratio based on a linear relation which was proposed by ENGESVIK and MOAN, starting from a semi-elliptical crack front the crack front turn into a straight crack front at a crack depth of 3 mm, the formulas are [Enge83]:

$$2 * c = 6.34 * a - 0.27 \tag{4.23}$$

$$\frac{a}{2} * c \; = \; 0; \text{if } a \; > \; 3 \text{ mm} \tag{4.24}$$

The assumption of a constant aspect ratio is especially suited for constructive design but describes not a real fracture mechanical relation. Normally, above a certain crack depth, there is a continuous crack front, which cannot be reflect by a constant aspect ratio. For that reason, the ENGESVIK and MOAN approach is used in the following [Enge83]. The condition that after 3 mm the elliptical transform in a straight crack front will result in a jump between the values but this has to be accepted. The formulas for M_a and M_{ka} are used to calculate the SIFs together with the ENGESVIK and MOAN aspect ratios [Enge83]. These calculations are neglecting the determination of the crack width *c* but make it possible to determinate the SIFs without using the Paris-Erdogan equation in an iterative cycle. The results are depicted, together with the analytical 2D values, in Figure 4.9. In this plot, the results based on the *ΔN* increment were connected by a spline function and the results for each crack depth *da* = 0.1 are plotted, this allows a better comparison.

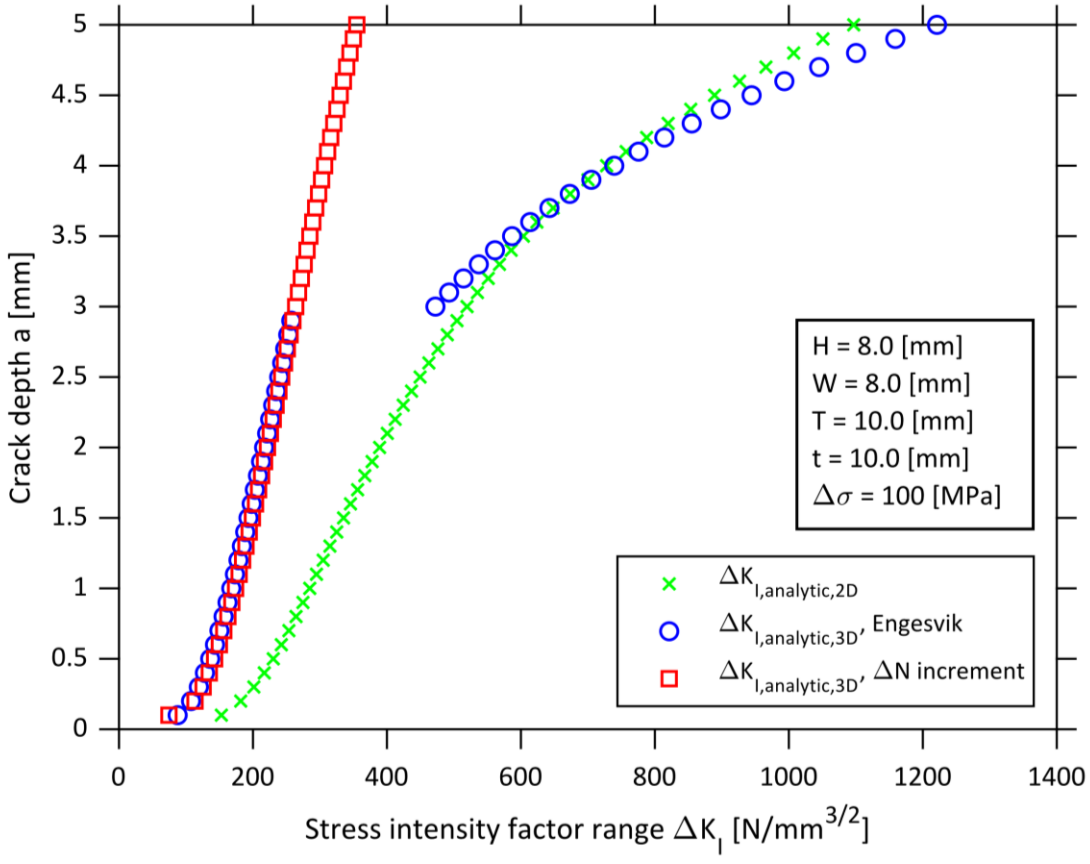

Figure 4.9: Analytical calculated SIFs for a transversal stiffener with different methods

Figure 4.9 shows that the SIFs calculated with the iterative approach and with the 3D formulas together with the ENGESVIK and MOAN aspect ratio are almost congruent until the straight crack front is reached [Enge83]. After this point the values differ greatly. The plot shows also that the SIFs calculated by the 2D formulas are not comparable with the iterative solutions at any point but with the 3D ENGESVIK and MOAN solutions after *c* = *b* [Enge83].

The approach that a continuous crack front is existing after a crack depth of 3 mm is not reflected in the iterative calculation. For the example geometry, at the final crack depth a_f = 5 the final crack width is only c_f =14.0 mm. The apparent contradiction between the ENGESVIK and MOAN transition and the iterative solution is based on the fact that iteratively only one initial defect was simulated, but in reality, there are several initial defects that grow together at a certain depth. According to BOWNESS and LEE, this leads to a dramatic drop in the aspect ratio *a/c* [Enge83] [Bown02], see Figure 4.10.

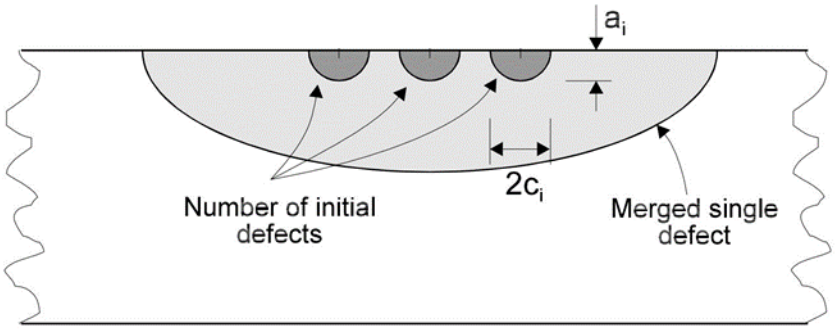

Figure 4.10: Sketch of crack growth with multiple initial defects [Bown02]

The assumption of a continuous crack front after 3 mm can therefore be assumed to be realistic. As already mentioned, however, the NEWMAN and RAJU function is not verified for *c* = *b* [Newm81]. Therefore, after the transition, the 2D formula is used to calculate the correction factor *M*, the resulting plot is depicted in Figure 4.11.

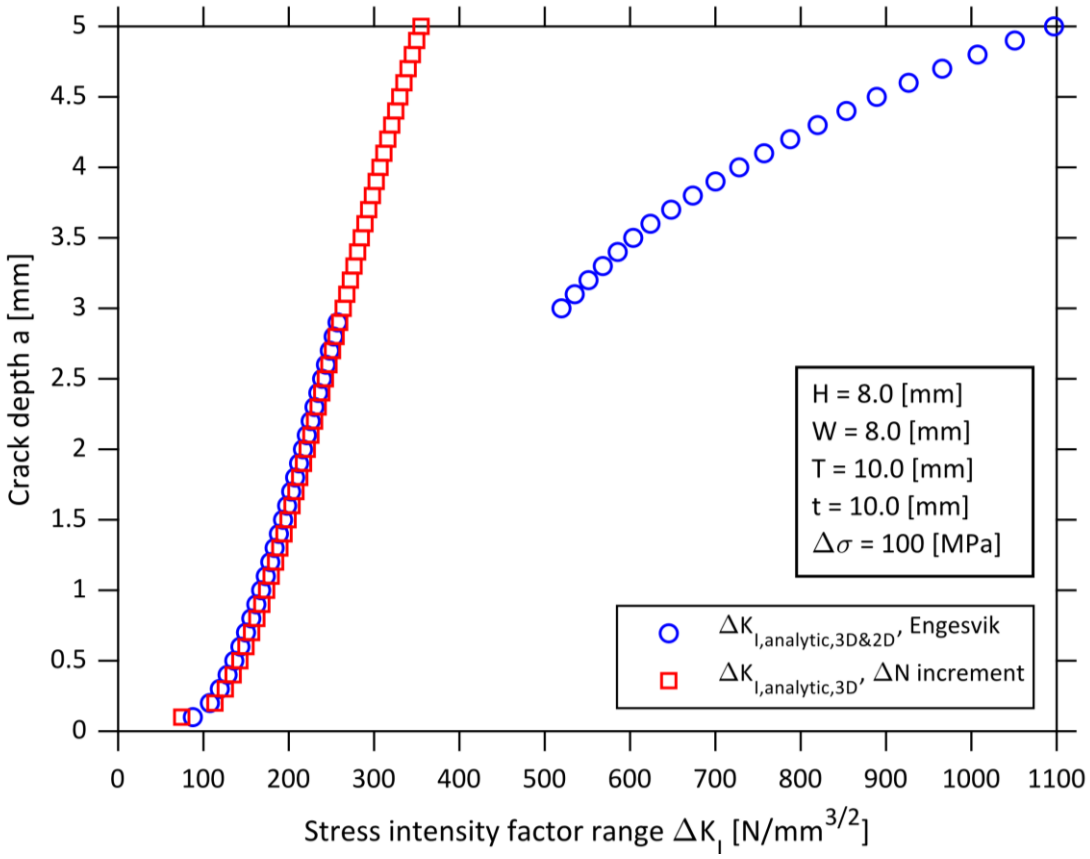

Figure 4.11: Analytical calculated SIFs for a transversal stiffener with adapted transition point from elliptical to straight crack front

4.3.3 Cruciform joint – weld toe failure

The procedure and the necessary specifications for determining the analytical solutions for the weld toe failure in the C-joint largely are corresponding to the transversal stiffener, see Section 4.3.2. However, there is the central difference that there are no detailed formulas, for the C-joint M_k values, as described by BOWNESS and LEE for the transversal stiffener [Bown02]. Instead, in the literary adjustment functions are written to the elliptical case, e.g. in BS7910 [Brit15]. First, the weighting functions for the 2D case should be determined. Subsequently, the calculation of the adaptation factors for the 3D case take place. For the calculation of the weight function M the same equations and sub-equations as for the transversal stiffener are used, see Formulae (4.10 and (4.15. The M_k values for the C-joint with a toe failure can be found in the IIW recommendations, their definition is [Hobb16]:

$$M_k = C_{Mk} * \left(\frac{a}{t}\right)^{k_{Mk}} \tag{4.25}$$

$$M_k \geq 1 \tag{4.26}$$

$$C_{Mk} = 0.8068 - 0.1554 * \left(\frac{H}{t}\right) + 0.0429 * \left(\frac{H}{t}\right)^2 + 0.0794 * \left(\frac{W}{t}\right) \tag{4.27}$$

$$k_{Mk} = -0.1993 - 0.1839 * \left(\frac{H}{t}\right) + 0.0495 * \left(\frac{H}{t}\right)^2 + 0.0815 * \left(\frac{W}{t}\right) \tag{4.28}$$

As previously the SIF equation can be solved with the M_k and M values:

$$\Delta K_I = \Delta\sigma * \sqrt{\pi * a} * M_k * M \tag{4.29}$$

The adaption from the 2D to the 3D case are done by extending the M equation with the parameters f_w, f_Φ, g and Q:

$$M = \left(M_1 + M_2 * \left(\frac{a}{T}\right)^2 + M_3 * \left(\frac{a}{T}\right)^4\right) * \frac{f_w * f_\Phi * g}{Q} \tag{4.30}$$

For the aspect ratio the ENGESVIK and MOAN linearisation is used with the transition from an elliptical to a straight crack front at a = 3 mm [Enge83]. The results of the calculation for the 2D and 3D case are depicted in Figure 4.12. Because of the scope of the 3D M function after the transition the 2D formula should be used.

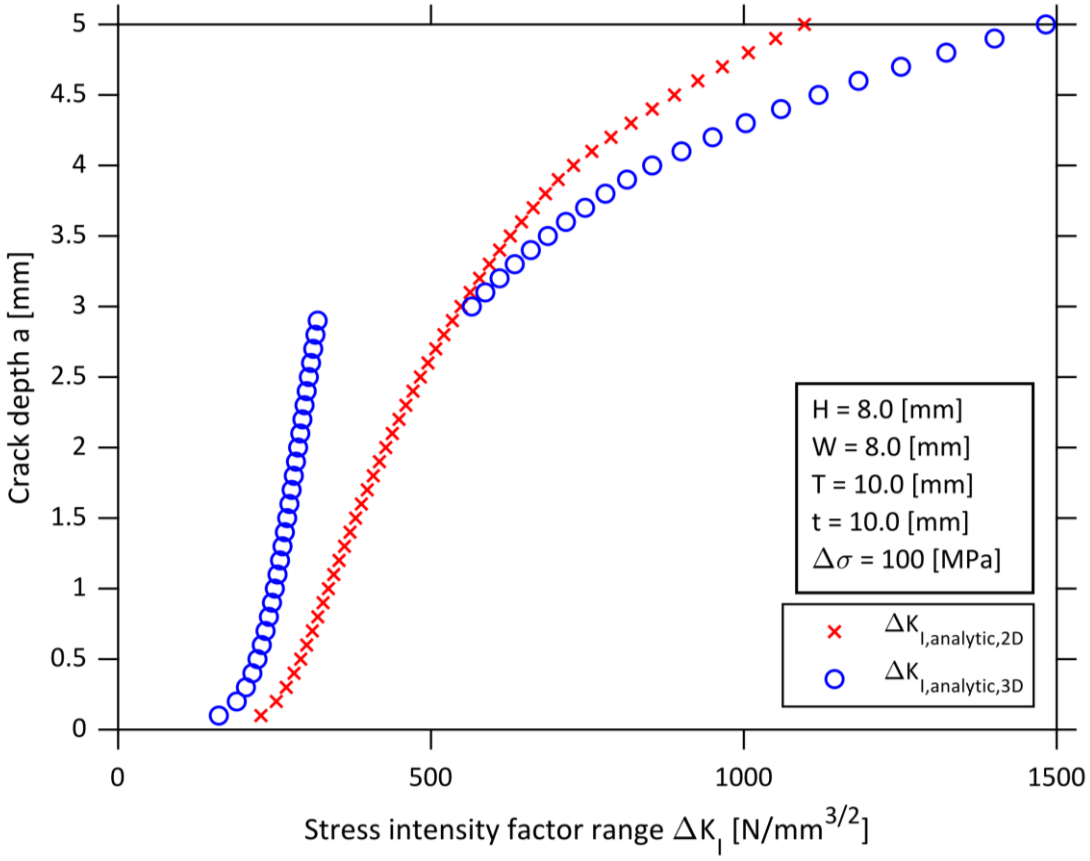

Figure 4.12: Analytical calculated SIFs for a C-joint with 2D and 3D equations

4.4 Creation of numerical solutions

The numerical calculations of the SIFs are executed according to the procedure in Figure 4.2, the results are stored in a master file together with their metadata. For a later calculation of the fatigue lives based on the Paris-Erdogan equation the FEM simulation do not have to be repeated, the numerical results remain unchanged see Section 4.3.2. Decisive for the accuracy of numerical results is the quality of the model geometries, the mesh, the boundary conditions and the settings of the FEM program. In the following section, the design of the FEM models and the settings made in Franc2D is discussed, the SIFs for the specimen geometry determined and their validity confirmed or discarded on the basis of the analytical results from the previous Section 4.3.

For the simulation of fracture mechanical behaviour and their failure, much of the necessary information has already been included, such as the geometric dimensions of the model, the step size of the increment *da*, the selection of the 2D simulation environment, the material parameters, the initial dimensions of the crack and the definition of the loads. Not yet determined is the fineness of the mesh, it affects the accuracy of the simulation results. The mesh is generated in ANSYS APDL, the generation depends on the defined geometry of the weld so that a uniform mesh can be generated for all weld configurations. The fineness of the mesh depends on one settings parameter, by adjusting this parameter the mesh density can be changed if the initially selected mesh density proves to be unsuitable. Due to the increased complexity of the network definition, a uniform size of the elements for the entire model is

used. Advantageous would be a finer definition in the area of the crack and a coarser definition on the plate end but this would increase the workload for the initial design of the scripts. The fracture mechanical simulation takes place in a 2D environment, compared to 3D, the number of elements is significantly lower. Therefore, a relatively fine mesh can be used for the entire model, without that the computational effort becomes too high. For the model higher order 2D, 8-node or 6-node elements are used, see Figure 4.13 [Depa17]. By the creation of the cracks in Franc2D, the elements around the crack front are deleted and substituted with degenerated triangle elements, this is done by using an approach from the energy method to take into account the stress increase. Nevertheless, fine meshes are necessary to achieve the required accuracy of the results [Fric17]. The size of the elements is defined as $T/20$, for a plate with the thickness of T = 10 mm the edge length of an element is 0.5 mm.

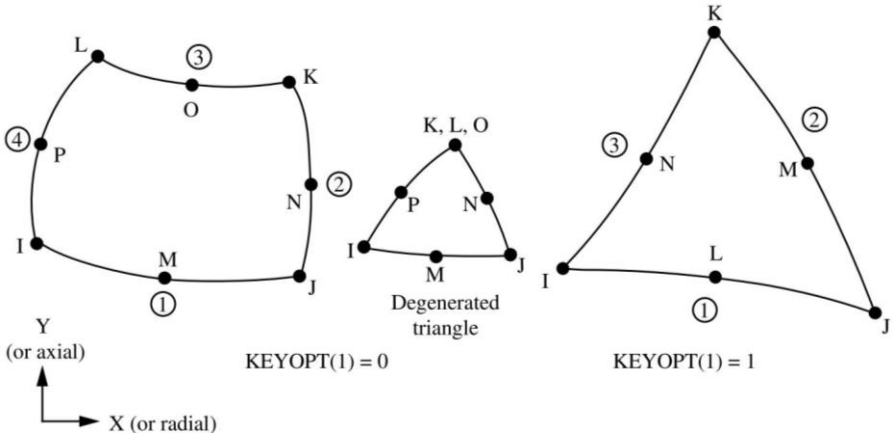

Figure 4.13: Geometry of the Plane183 Ansys APDL element [Depa17]

The simulation of the two types of weldments, transversal stiffener and C-joint, and their possible failure locations, toe and root failure, differs in how their geometry and the crack should be represented in the model. The previously enumerated assumptions are equally valid for all cases. The individual cases are discussed below, starting with the C-joint, that breaks at the root.

4.4.1 Cruciform joint – weld root failure

For the simulation model of the C-joint with root failure has to be clarified, which simplifications can be made to reduce modelling and simulation effort. A classical approach in the FEM is to show if there are existing or assumable symmetries, which can be replaced by bearings. The examined specimens have each 4 weldments, which differs in their local geometry. For the simulation of the real specimens just the weldment which causes the failure is from relevance. For the failure of a weld, the detailed geometries of the other welds are of subordinate importance, because their influence on the acting tensions on the critical weld are negligible. This determination allows the simplification that all welds have the same, the critical, geometry. In Section 3.2 a procedure has been displayed to correct the effects of the angular and axial misalignment, thereby only stresses within the plate must be taken into account. These two assumptions allow the use of the axial symmetry around the y-axis, see Figure 4.14 (a).

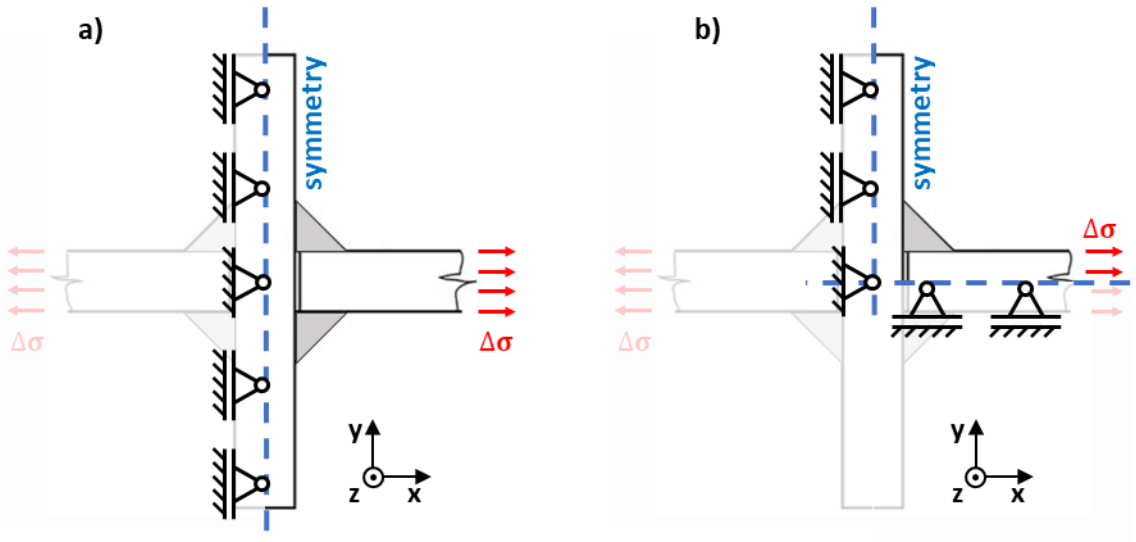

Figure 4.14: C-joint – axial geometry around y-axis (a) and axial geometry around x-axis (b)

The crack growth for C-joints failing at the root takes place nearly simultaneously in the two weldments on one side, even though the crack at the critical weld is slightly more developed, see Figure 4.15. The effect of simultaneous crack growth is magnified by the simulation assumption that alle weldments have the same geometry. Based on this observation also the symmetry around the x-axis can be used in the FEM model, see Figure 4.14 (b).

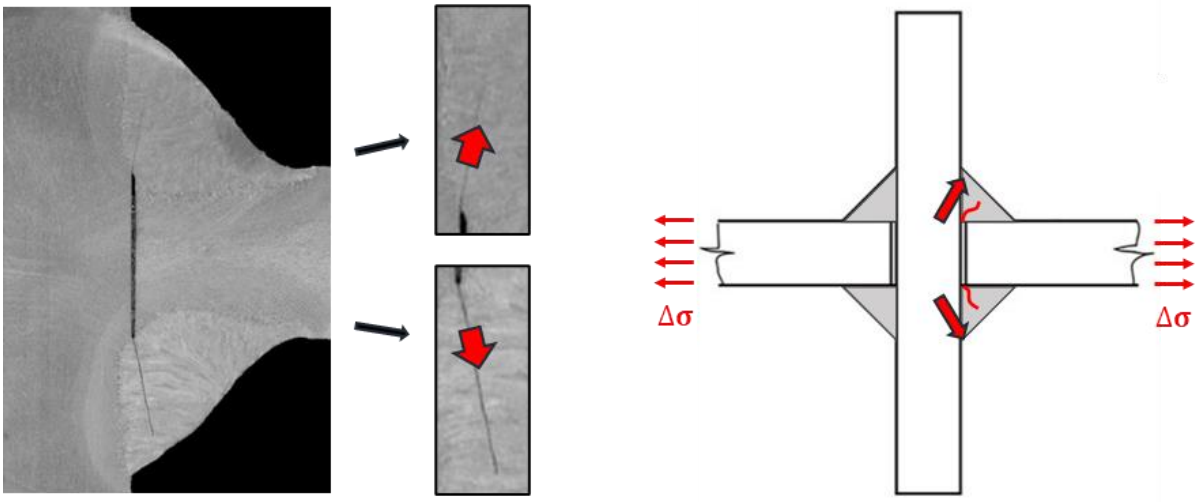

Figure 4.15: Macrographic of a C-joint with weld root failure and a sketch of the case, from [Brau20a]

Before the parametric script for the simulation model can be created, it must be decided how the non-welded gap is to be considered. This is possible in two ways, either the non-welded gap is modelled as a blank space in the model or as an already existing crack in solid material via Franc2D. In the following FCG simulation, this crack is continued. The second possibility has its analogy in the analytical formulas, as there the non-welded gap is taken into account as initial crack length. With this approach no additional initial cracking depth a_i must be defined. To determine which approach is better suited, the corresponding models are generated and their SIFs are calculated via Franc2D, see Figure 4.16.

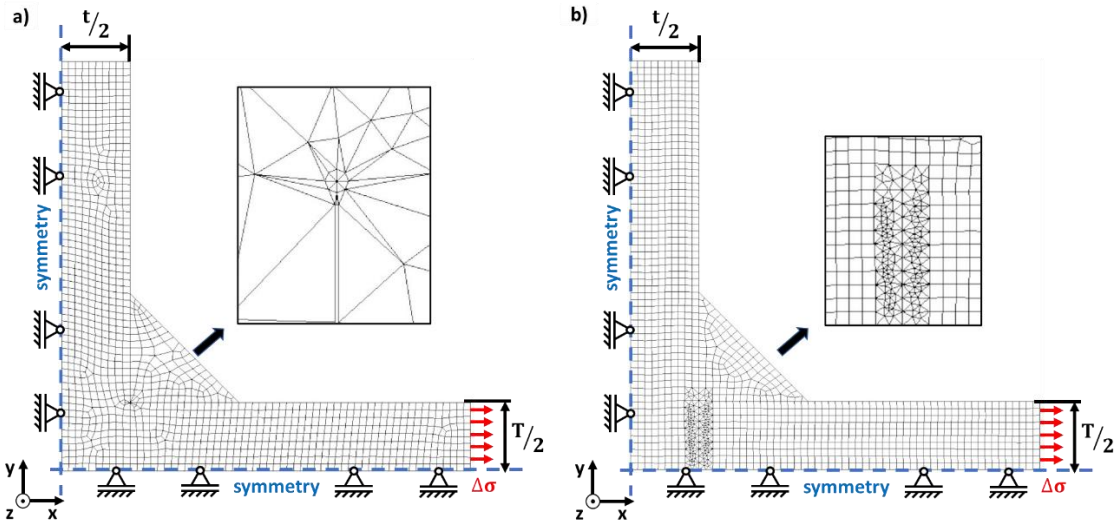

Figure 4.16: Simulation model for C-joint with weld root failure – crack as empty space (a) and crack as initial crack length (b)

In the following, the results will be compared with the analytical solution from Section 4.3.1. In order to reduce the deviation of the SIFs from reality, the mean values for both the numeric and the analytical SIFs should be created. The averaging of two consecutive crack states prevents the SIFs from being over- or underestimated [Fisc12]. The formula is:

$$\log(\Delta\overline{K}_{I,2}) = \frac{\log(\Delta K_{I,1}) + \log(\Delta K_{I,2})}{2} \tag{4.31}$$

The two simulation models are now opened in Franc2D and the FCG simulated. After that, the numeric calculated SIFs are read into MATLAB and evaluated together with the analytically SIFs. In Figure 4.17, the SIFs are compared, the exact values can be found in Appendix A2. From the values it can be seen that the numerically calculated SIFs from both models have a good match with the analytical SIFs. From particular importance is the conformity at short crack length because the majority of the fatigue life takes place there. The deviation of the full model is smaller than that of the model with the blank spaces. Therefore, the full model is used in the further course of the work. The high level of matching with the analytical solution shows that the chosen mesh size is suitable, so no further sensitivity analysis is conducted.

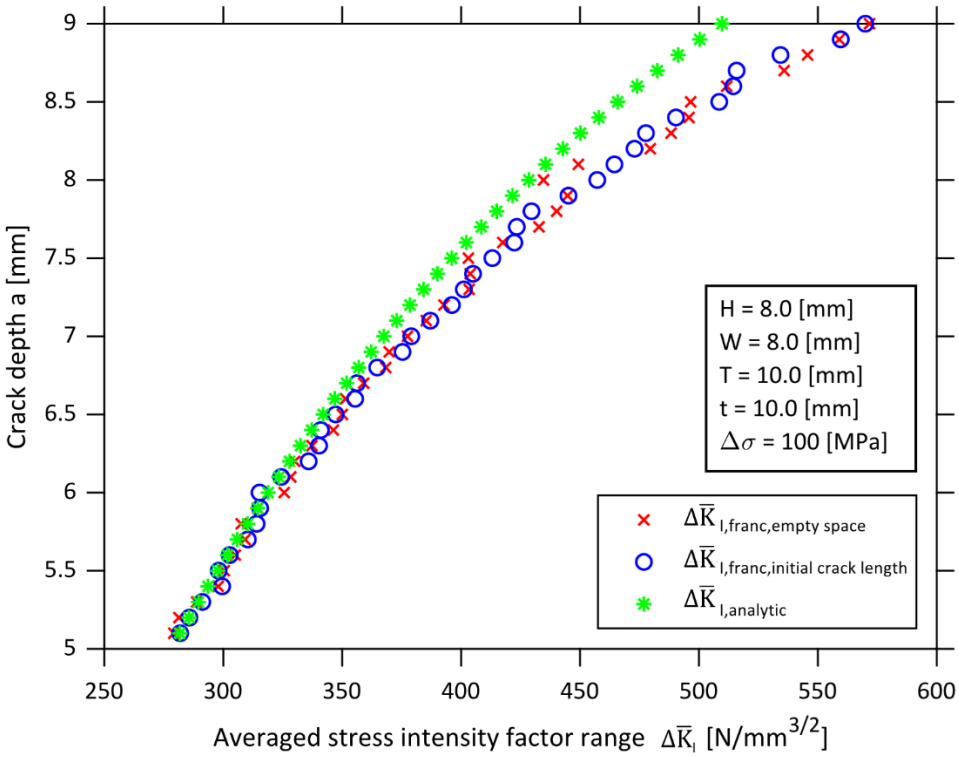

Figure 4.17: Comparison of the numerical and analytical solutions

4.4.2 Transverse stiffener – weld toe failure

The procedure and the decisions to determine the simulation model of the transversal stiffener correspond to those that have been made in the previous Section 4.4.1. All weldments of the model have the shape of the critical weldment. Therefore, the symmetry around the y-axis can be used and only one side of the specimen is to simulate. In contrast to the failure at the root of the C-joint, the crack growth is based on one weld, there is no symmetry around the x-axis, see Figure 4.18.

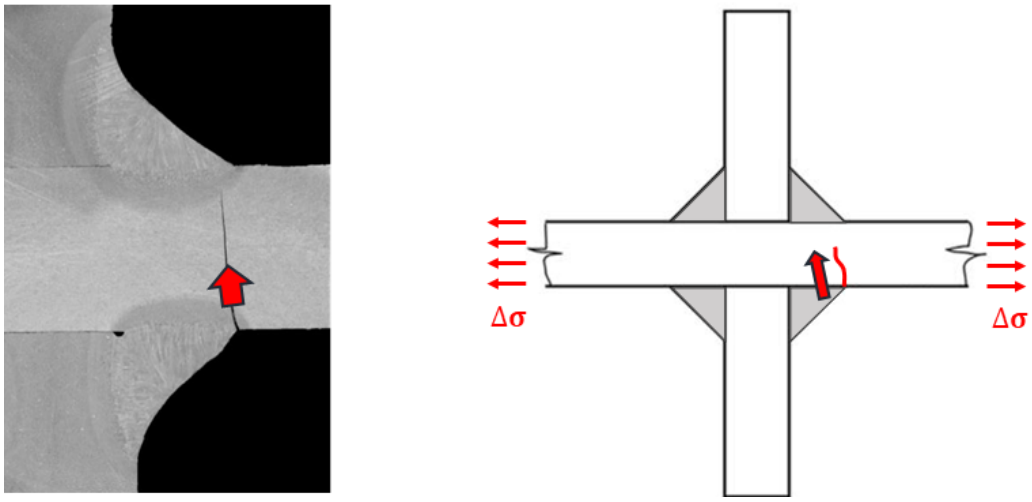

Figure 4.18: Picture of a transversal stiffener with weld toe failure and a sketch of the case, macrographic from [Brau20a]

There is no non-welded gap which serves as the origin of crack growth, the non-welded gap is designed as blank space in the model. The initial crack starts direct at the weld toe and is rectangular to the plate, the initial crack depth is a_i = 0.1 mm. The model is pictured in Figure 4.19.

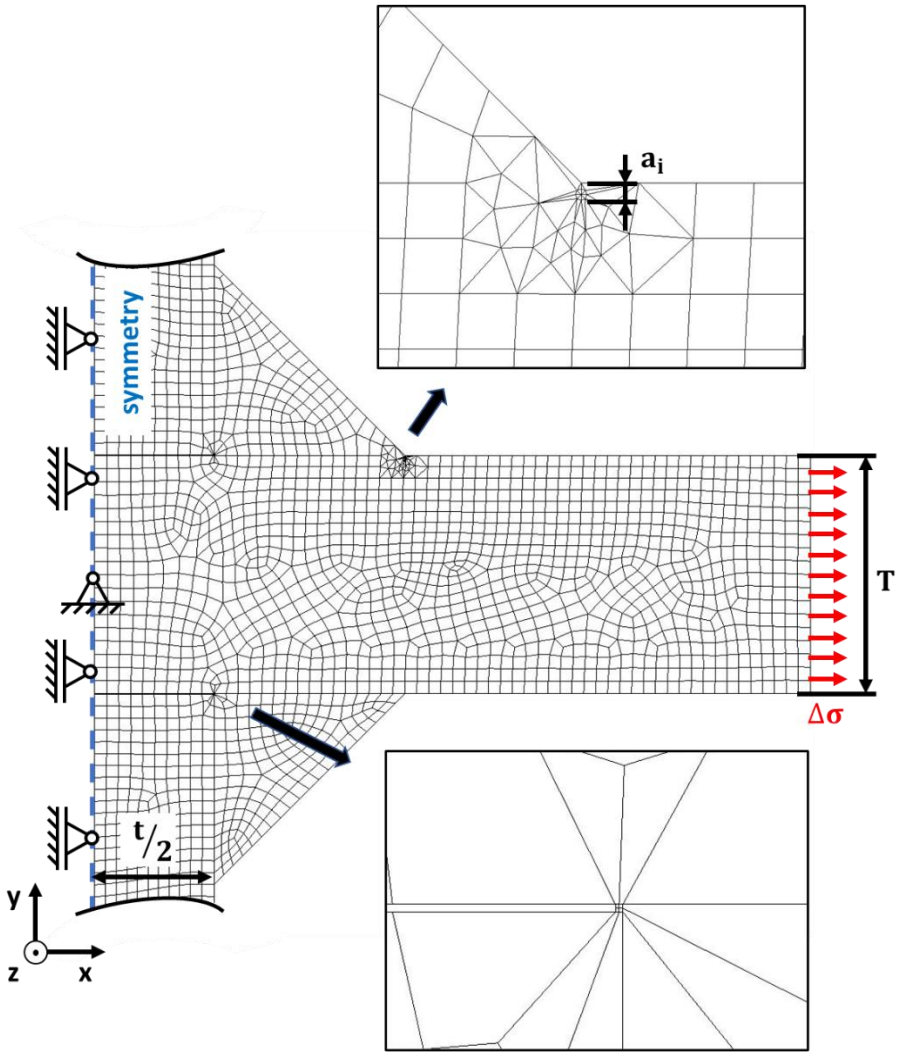

Figure 4.19: Simulation model for transversal stiffener – non-welded area crack as empty space and crack with initial crack length

The SIFs calculated by Franc2D are transmitted to MATLAB and the average SIFs calculated, just as the analytical SIFs. The plots for the analytical 2D, 3D SIFs and the numerical SIFs are plotted in Figure 4.20, the detailed values can be found in Appendix A3.

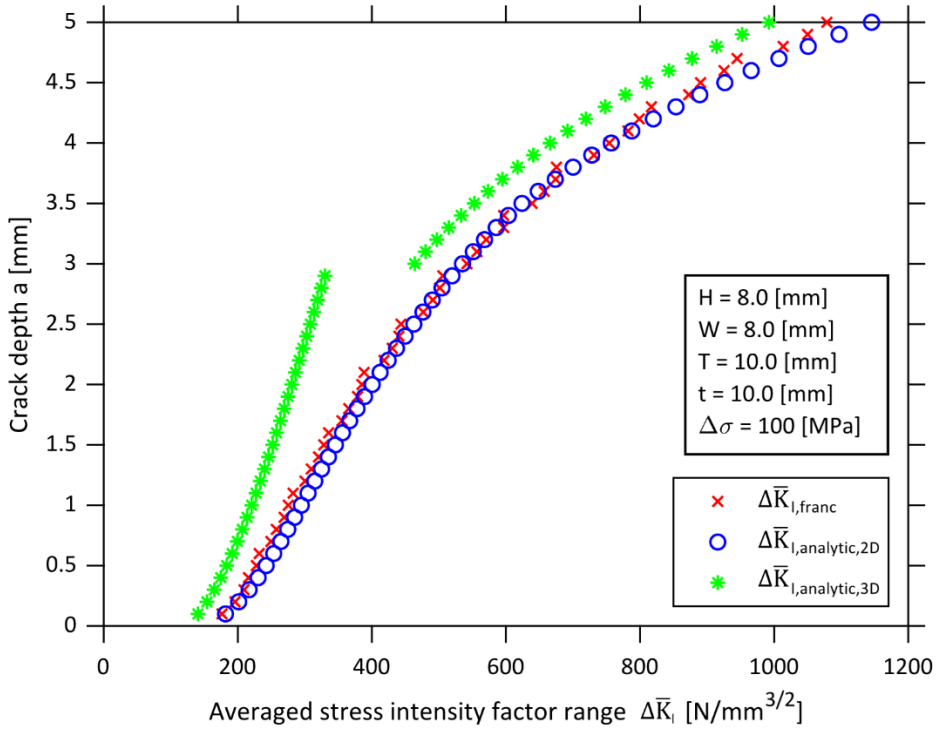

Figure 4.20: Comparison of the numerical and analytical solutions

In Figure 4.20 can be seen that the numerical and the analytical 2D SIFs show a great degree of congruence. That is validating the numerical model but also shows that there is a gap between 3D reality and the simulation. In the further process of the thesis, below the transition to a continuous crack front at 3 mm, the SIFs are calculated via the 3D formulas, above this the 2D formulas, see Section 4.3.2. The congruence between the numerical and the 2D analytical calculated SIFs also shows also that the initial cracking depth of a_i = 0.1 mm according to the IIW Recommendations for the context is well suited. Further reviews with other initial crack depth are therefore not examined.

4.4.3 Cruciform joint – weld toe failure

The C-joint failing at the weld toe differs from that of the transversal stiffener only in the analytical formulas used, see Section 4.4.2. The procedure for the numerical calculation of the SIFs is quite similar. The simulation model is depicted in Figure 4.21.

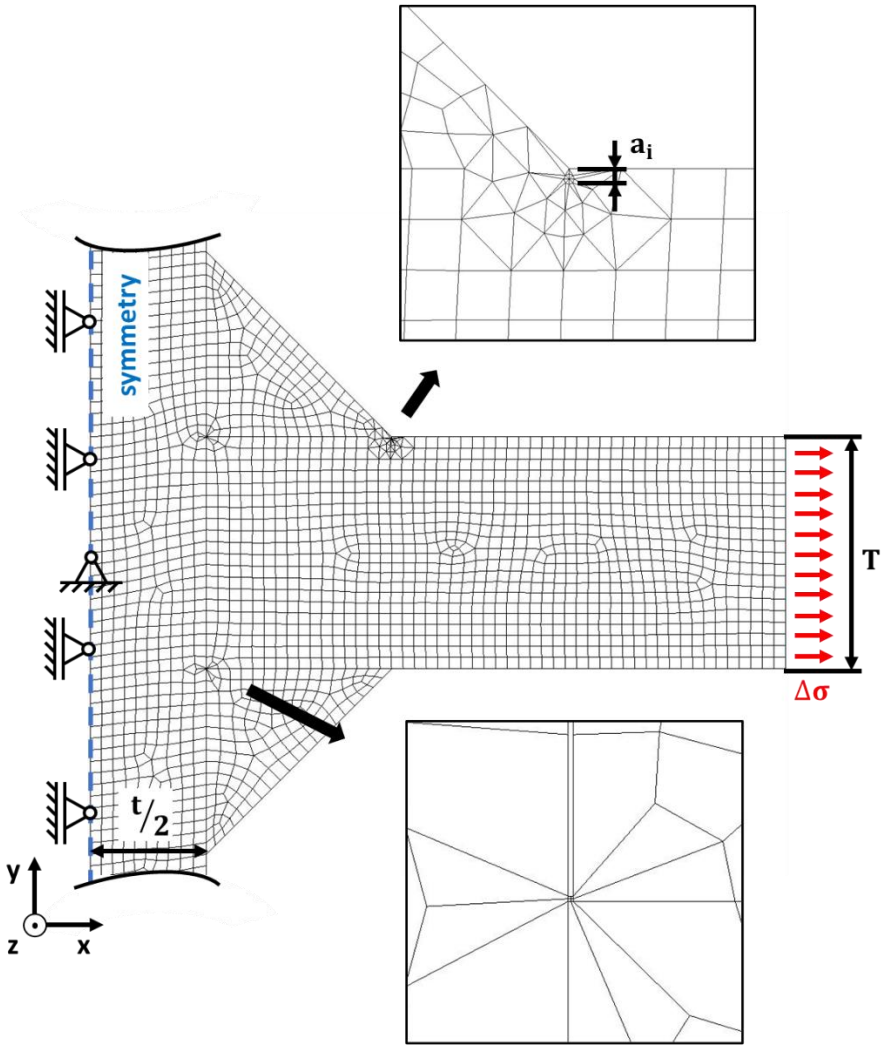

Figure 4.21: Simulation model for C-joint with toe failure– non-welded area crack as empty space and crack with initial crack length

The averaged SIFs calculated in Franc2D and the analytical SIFs are plotted in Figure 4.22 and the exact results can be found in Appendix A4. The numerical values have a good congruence with the 2D analytical values but not with the 3D analytical values. The numerical Franc2D SIFs can be seen as validated.

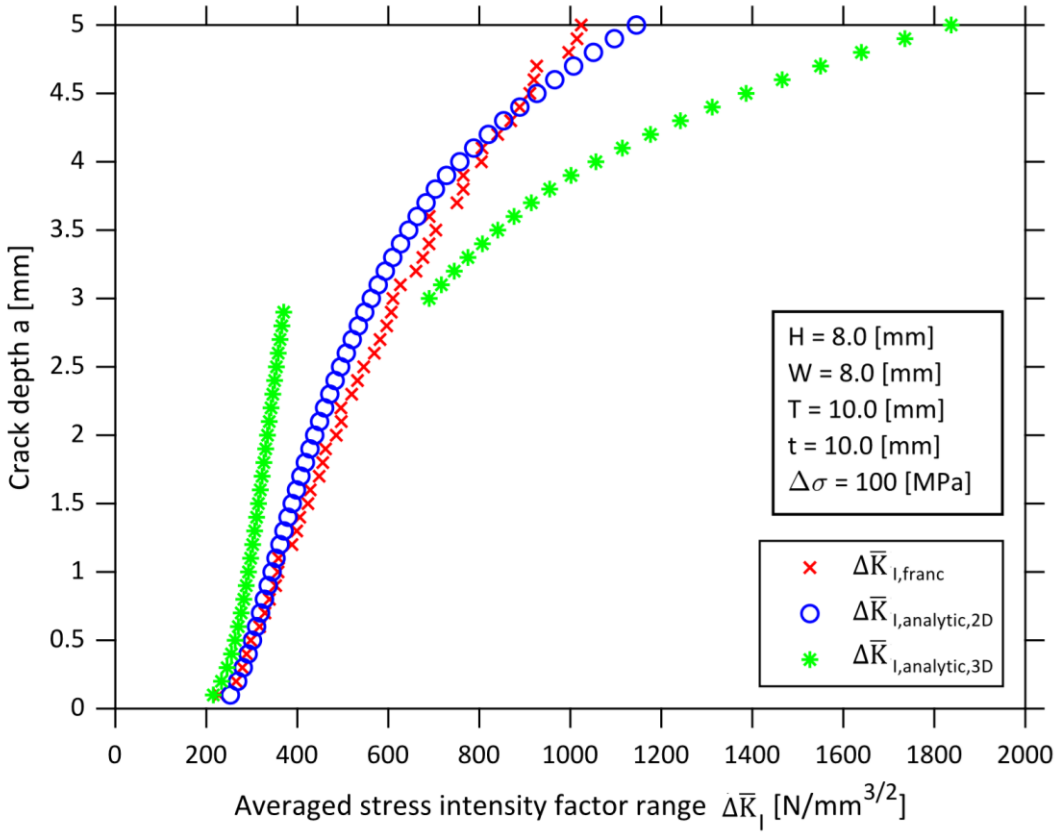

Figure 4.22: Comparison of the numerical and analytical solutions

5 Creation of a prediction model

In the previous Chapter 4, simulation models for the three test cases were developed and validated using analytical formulae. In this chapter, the fatigue life for different weldment geometries and temperatures will be predicted. First, the simulation models are verified on the basis of experimental results, in order to use these comparisons as a basis for further analyses.

5.1 Approach for the verification of the simulation models

The recorded measurement data of the fatigue tests include the number of cycles until the final failure of the specimen occurs, the machine parameters and the temperatures of the specimens as well as the test environment, see Section 3.3. The measurement of SIFs over the crack growth is complicated and therefore did not take place, the verification of the simulation models is based on the fatigue lives N_f. The fatigue life is calculated via the Paris-Erdogan equation from the SIFs, using the *C* and *m* parameters. The corresponding formulas are:

$$\frac{da}{dN} = C * (\Delta K)^m \tag{5.1}$$

$$N_f = \int_{a_i}^{a_f} \frac{da}{C * (\Delta K)^m} \tag{5.2}$$

The Paris parameters *C* and *m*, which are necessary for the calculation of the fatigue lives, are rarely mentioned in the literature. The existing parameters are also very general and broadly defined, i.e. there are few scopes of coverage. In the IIW Recommendations and BS7910, differentiations are made according to stress ratio *R* and for steel according to BM and WM [Brit15] [Hobb16]. With regard to temperatures lower than RT, there are no further specifications for temperature and material dependent ranges of validity. In the case of steel materials, large differences can be assumed between the Paris parameters *C* and *m*, see e.g. SCHIJVE and Figure 2.9 [Schi09]. Through a paper by SALLABA et al., results from constant ΔK experiments on S235 and S500 are available, from which the *C* and *m* values can be calculated [Sall22]. For this purpose, the Paris-Erdogan equation is extended by adding the logarithm. By determining the slope in logarithmic space, *m* can be obtained. Then the parameter *C* can be calculated. The Paris-Erdogan equation extended by the logarithm is:

$$log\left(\frac{da}{dN}\right) = m * log(\Delta K) + log(C) \tag{5.3}$$

The available parameters for *C* and *m* are shown in Table 5.1.

Table 5.1: Parameter for Paris-Erdogan equation

Source	Material	Environ-ment	Tempe-rature	Units	C	m
IIW	Steel - BM	Air	≤ RT	$\left[N * mm^{-\frac{3}{2}}\right]$	$3*10^{-13}$	3
IIW	Steel - WM	Air	≤ RT	$\left[N * mm^{-\frac{3}{2}}\right]$	$5.21*10^{-13}$	3
BS7910	Steel - BM	Air	< 100 °C	$\left[N * mm^{-\frac{3}{2}}\right]$	$5.21*10^{-13}$	3
BS7910	Steel - WM	Air	< 100 °C	$\left[N * mm^{-\frac{3}{2}}\right]$	$1.10*10^{-13}$	3.1
SALLABA et al. [SALL22]	S235 - BM	Air	RT	$\left[N * mm^{-\frac{3}{2}}\right]$	$1.02*10^{-16}$	4.2
SALLABA et al. [SALL22]	S235 - WM	Air	RT	$\left[N * mm^{-\frac{3}{2}}\right]$	$6.26*10^{-14}$	3.2
SALLABA et al. [SALL22]	S500 - BM	Air	RT	$\left[N * mm^{-\frac{3}{2}}\right]$	$3.02*10^{-14}$	3.38
SALLABA et al. [SALL22]	S500 - WM	Air	RT	$\left[N * mm^{-\frac{3}{2}}\right]$	$8.13*10^{-12}$	2.36

For the verification of the simulation models, the fatigue lives at RT are examined. For the verification, the values for the upper bound from the IIW Recommendations BS7910 and the values for the mean curve by SALLABA et al. are used and the results are compared [Hobb16] [Brit15] [Sall22]. The differences in the definition and scope of the values must be accepted due to the lack of data on the mean value curves in the standards.

5.2 Verification of cruciform joints – weld root failure

For the C-joints, at RT and *R* = 0, there are data for 24 experiments available, which led to a failure at the root. Of these, 12 specimens were made of S235 and 12 of S500. The geometries of the specimens, the applied stress and the experimentally determined fatigue life are shown in detail in Appendix A5. For the calculation of the fatigue life from the averaged SIFs at weld root failure, the *C* and *m* parameters for the WM are used, see also Section 3.1. Figure 5.1 plots the results of the calculation of the fatigue life for the analytical and numerical SIFs with the parameters from BS7910 and the experimentally determined fatigue life of one specimen.

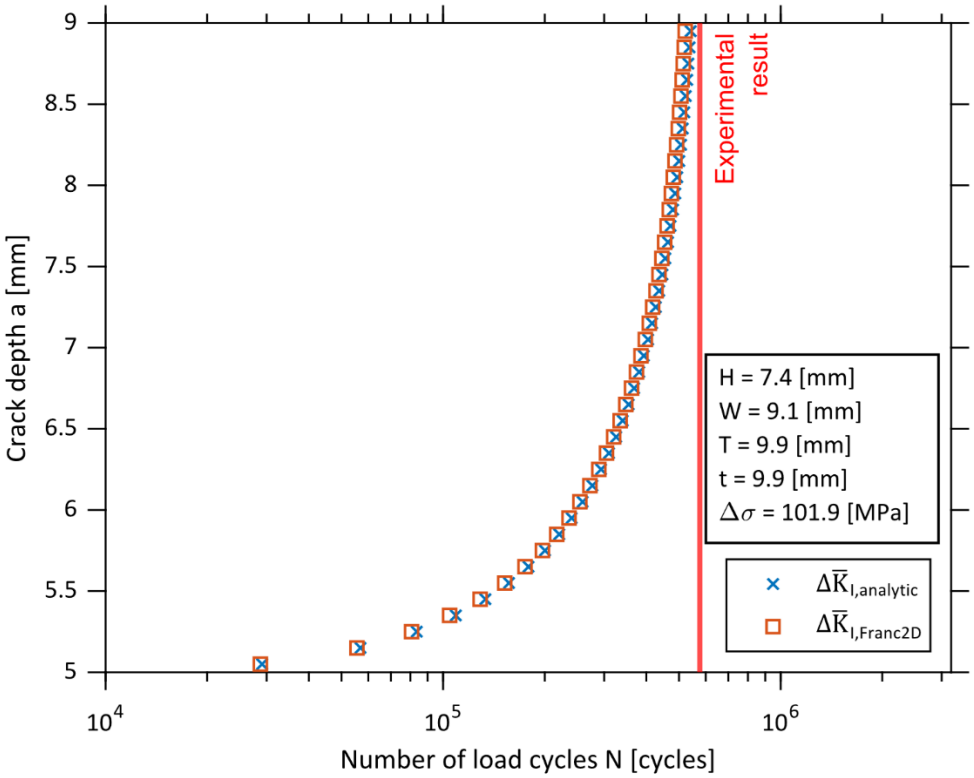

Figure 5.1: Comparison of numerical and analytical calculated fatigue lives with experimental results – BS7910 WM S500

This presentation is not suitable for assessing the accuracy of the prediction, only the deviation in relation to one test can be shown well, but several results must be taken into account for a meaningful prediction. Figure 5.2 shows the fatigue lives of all tests, separately for S235 (a) and S500 (b), at RT and $R = 0$ in logarithmic space. In the plots, the predicted fatigue life of the numerical SIFs is compared to the experimentally determined value. The 1:1-line represents the ideal case of perfect agreement between predicted and experimental values, the further the points are from this line, the worse the prediction. A curve fitting of first order has been drawn through the single points in the logarithmic space.

Due to the structure of the formulae, the parameter *m* defines the slope and the two parameter *C* and *m* define together the shift, see Formulae (5.3. A slope of the best fit line deviating from the 1:1-line therefore indicates the degree of deviation of the *m* parameter, while the distance between the best fit line and the 1:1-line defines the degree of deviation of the *C* parameter, if the *m* parameter fits.

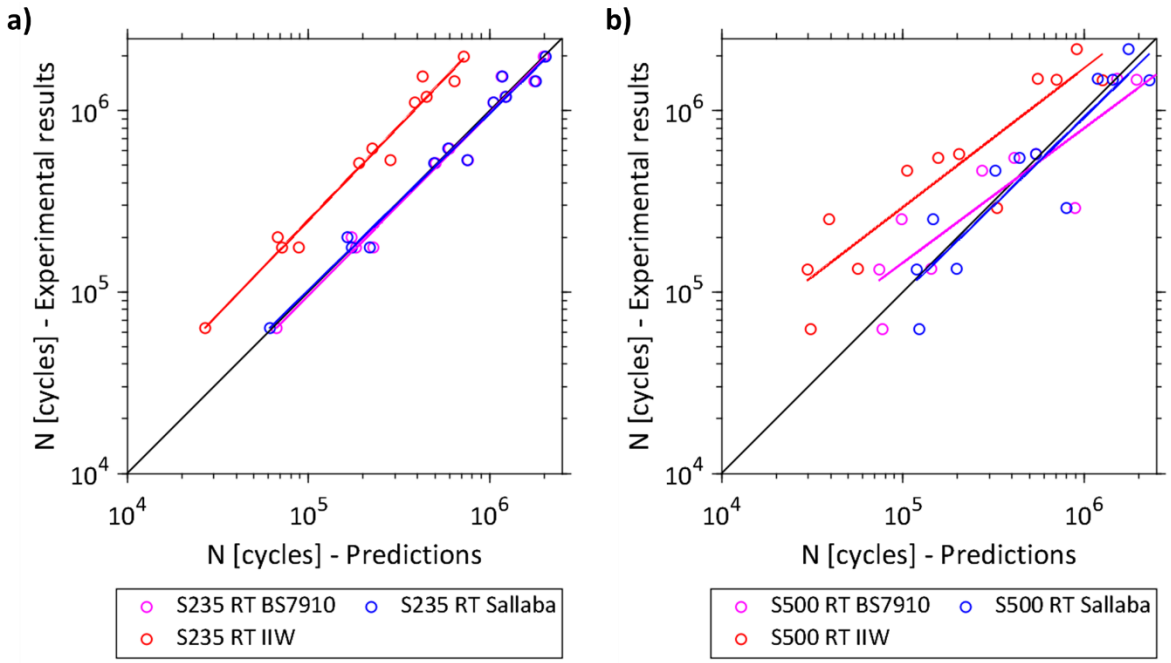

Figure 5.2: Comparison of numerical calculations of the fatigue lives with experimental results – C-joint root failure for S235 specimens (a) and S500 specimens (b)

The results in Figure 5.2 show with respect to the used *C* and *m* parameters that with the values from BS7910 and SALLABA et al. a high agreement between prediction and reality can be achieved [Sall22]. However, the comparison of the 1:1-lines with the first order best fit line shows that the correlation of the SALLABA et al. values is higher [Sall22]. Independent of the Paris parameters, the results show that the scatter of the results among the S500 specimens is higher than among the S235 specimens. The exact reasons for this cannot be assessed conclusively at this point, but it should be noted that 11 of the 12 S235 specimens were sawn from the same plate, while 8 of the S500 specimens were sawn from one plate and the remaining 4 from two other plates. In the following Section 5.5, the fatigue life at sub-zero temperatures is predicted. The results at RT with the Paris parameters of SALLABA et al. are used as a reference [Sall22].

5.3 Verification of transverse stiffener

For the prediction of the fatigue life of transversal stiffener, the key difference is that the failure occurs at the weld toe. In this case, the crack initially grows within the HAZ and then transitions into the BM. Due to the non-uniform dimensions and composition of the HAZ, the FCG is difficult to describe, see Section 2.6. Additionally, there are only few data of Paris parameters for the HAZ, therefore, similar to SONG et al., the simplifying assumption for the weld toe is made, that the FCG take place only in BM [Song21], see Section 3.1. If the assumption does not correspond to reality, it is to be expected that the predicted and the experimentally determined fatigue lives show a low agreement. In the case of a high deviation, the predicted fatigue lives would have to be higher than the experimentally determined values due to on average poorer mechanical properties of the HAZ material compared to the BM.

As shown in Section 4.4.2, the failure at the toe cannot be simulated in 2D, due to the 3D effects, the fatigue lives are significantly higher than simulated in 2D. Because no 3D simulation programme is used in this work, the 3D analytical solutions are used for prediction instead. Measurement data are available for 19 transversal stiffeners at RT and $R = 0$, of which 9 are made of S235 and 10 of S500. Detailed information on the individual specimens are given in Appendix A6. The comparison of the predicted values with the test results is shown in Figure 5.3.

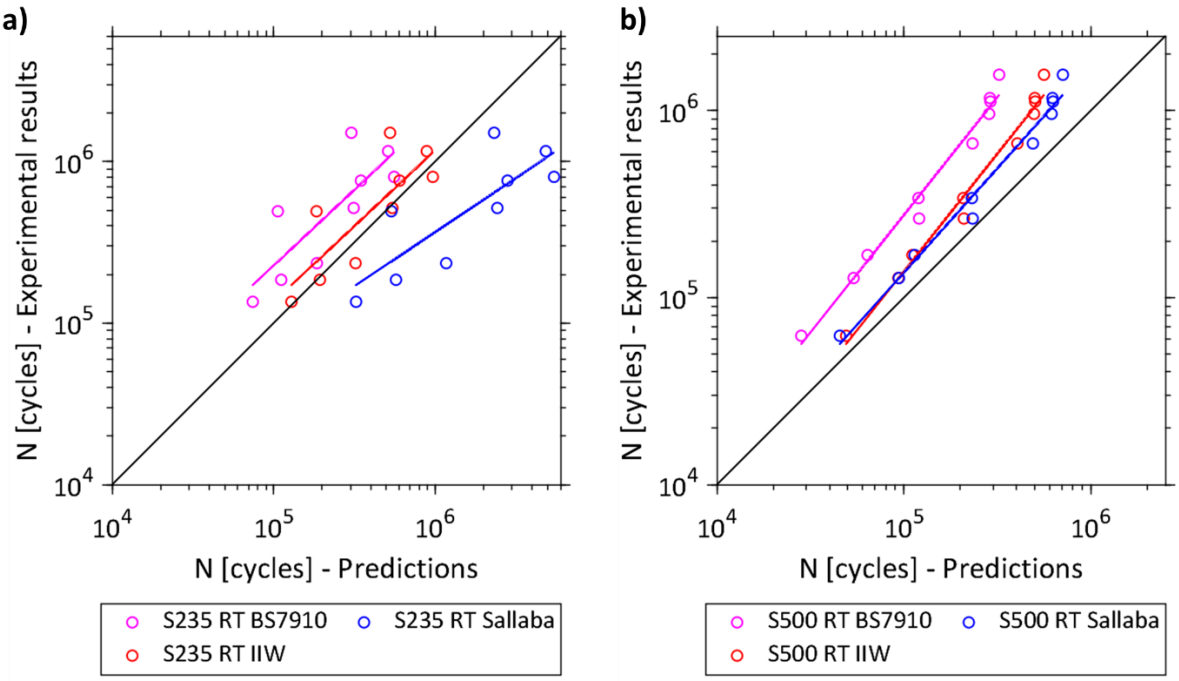

Figure 5.3: Comparison of analytical calculations of the fatigue lives with experimental results – transversal stiffener for S235 specimens (a) and S500 specimens (b)

The comparisons plotted in Figure 5.3 and their first order best fit line show that the predictions of the fatigue life for the S235 steel and the Paris parameters of SALLABA et al. are indeed partially overestimated [Sall22]. However, the fatigue lives predicted in this way differ from those of the IIW recommendations and BS7910, which also describe BM. However, it should be noted that the Paris parameters from SALLABA et al. are supposed to describe the mean FCG curve, while the parameters from the standards define the upper bound [Sall22]. The best fit line of the IIW recommendations show only small deviations from the 1:1-line for both the C and the m parameters. For the steel S500, the best fit line through the parameters of SALLABA et al. has a high agreement with the 1:1-line and differs only slightly from the best fit line through the parameters of the IIW recommendations [Sall22]. The very high deviation of the best fit line from the values of SALLABA et al. for S235 compared to the experimental fatigue lives, the very high deviation compared to best fit line from the IIW recommendations and the completely different behaviour of the best fit line from the values of SALLABA et al. for the S500 specimens, indicates that the results of the constant ΔK experiments of SALLABA et al. might not represent the actual material behaviour of S235 BM [Sall22]. In summary, the comparisons indicate that the simplifying assumption of crack growth by BM is sufficiently accurate. As a

reference for tests at different temperature levels, the Paris parameters of the IIW recommendations should be used for S235 and the Paris parameters of SALLABA et al. for S500 [Sall22].

5.4 Verification of cruciform joints – weld toe failure

Following the transition curves by MADDOX, the specimens tested in this thesis can be assumed to fail at the root due to their geometry, see Section 2.7 [Madd74]. Consistent with the curves, failure at the root occurred for the majority of the tested specimens but three specimens of S235 steel failed at the weld toe by a temperature of -20°C. These deviations cannot be explained by statistical scatter, as the number of specimens that failed in this way is too large. The reason for the failure at the weld root is not known, but one possible influencing factor could be the change of the material due to the welding process at the weld root. Because the FTT of the WM differs from that of the BM. The different FTTs are not taken into account in the limit curves of Figure 2.8 and therefore represent a possible explanation. However, this theory has to be proven in further investigations. Due to the small number of measurement results for this failure case and the lack of C-joint specimens that failed at RT at the toe, it is not possible to simulate this failure case in this thesis. Furthermore, as in Section 5.3 Paris, parameters for the HAZ are not available.

5.5 Verification of the cruciform joint – weld root failure at sub-zero temperatures

For the use of the simulation model at sub-zero temperatures, the Paris parameters have to be modified, they define the relationship between FCG and the SIFs. For this purpose, the paper by SALLABA et al. is used, who conducted constant ΔK tests at five different temperatures for the steel S500 for both BM and WM [Sall22]. For the steel S235, no Paris parameters for temperature levels other than RT are available, therefore the similarity with the behaviour of the S500 should first be proven by comparing the Paris parameters at RT. The parameters used for the C-joint are shown in Table 5.2. Detailed information on the geometry and test parameters as well as the calculated fatigue lives can be found in Appendix A7.

Table 5.2: Parameter for Paris-Erdogan equation – C-joint

Source	Material	Environment	Temperature	Units	C	m
SALLABA et al. [SALL22]	S235 - WM	Air	RT	$\left[N * mm^{-\frac{3}{2}}\right]$	6.26*10^{-14}	3.2
SALLABA et al. [SALL22]	S500 - WM	Air	RT	$\left[N * mm^{-\frac{3}{2}}\right]$	8.13*10^{-12}	2.36
SALLABA et al. [SALL22]	S500 - WM	Air	M0	$\left[N * mm^{-\frac{3}{2}}\right]$	8.32*10^{-12}	2.36
SALLABA et al. [SALL22]	S500 - WM	Air	M20	$\left[N * mm^{-\frac{3}{2}}\right]$	8.57*10^{-12}	2.36
SALLABA et al. [SALL22]	S500 - WM	Air	M40	$\left[N * mm^{-\frac{3}{2}}\right]$	7.92*10^{-12}	2.36
SALLABA et al. [SALL22]	S500 - WM	Air	M60	$\left[N * mm^{-\frac{3}{2}}\right]$	6.84*10^{-12}	2.36

Figure 5.4 compares the experimental data of the fatigue lives of the S235 specimens (a) and S500 specimens (b) with the predicted results with the Paris parameters at RT. Besides the experimental data, the figures also contain the data of the experiments at -20°C and -50°C, which were also calculated with the values of SALLABA et al. at RT [Sall22]. The experimental data for S235 at -50°C include two outliers for which the predicted fatigue lives are significantly higher than the experimentally determined values. If these 2 outliers are neglected at this point and first order best fit line is formed, the stratification of the best fit lines to each other is similar to that of the S500 specimens. For the experimental results at RT, the prediction is almost congruent with the 1:1-line. This is followed by the best fit line of the experiments at -20°C, which is slightly shifted from the 1:1-line, closer to the experimental results. Further away from the 1:1-line is the best fit line of the experimental results at -50°C, i.e. the real fatigue life is higher than the predicted one. The slopes of the best fit lines differ only slightly, the central difference being the displacement from the 1:1-line. The plots for S235 and S500 differ in the fact that the displacements of the best fit lines of the S500 specimens are smaller than for the best fit lines of the S235 specimens, due to the agreement in the ordering it can be assumed that the behaviour of the S500 specimens is similar to that of the S235 specimens. Due to the lack of Paris parameters for S235, the following investigations are limited to S500 steel.

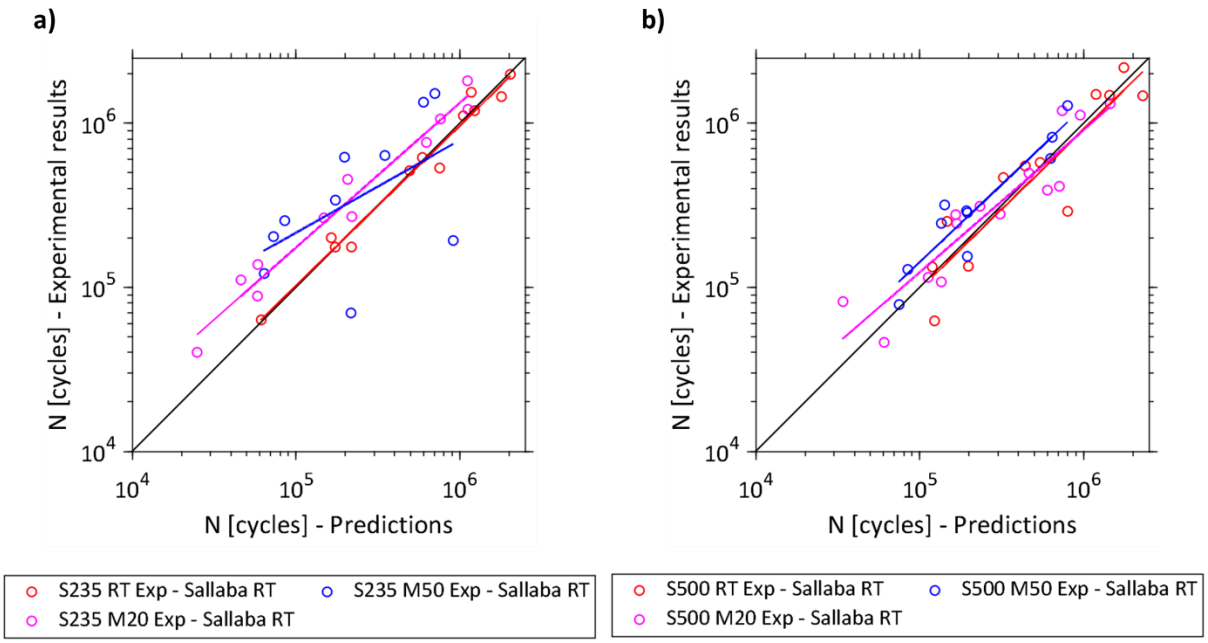

Figure 5.4: Comparison of numerical calculations of the fatigue lives with experimental results at different temperatures with same Paris Parameters for S235 specimens (a) and S500 specimens (b)

Figure 5.5 shows three plots which contain the experimental results of the S500 specimens, separated into the three test temperatures RT, -20°C and -50°C. In each plot the experimental data is shown five times, therefore the individual measurement points are only shifted on the x-axis, they are the same experimental results. However, the predicted data differed because they were determined with different Paris parameters. The first order best fit lines are all parallel to each other, as the SALLABA et al. parameter *m* that determines the slope in the log-log plot is given as a constant 2.36 for all temperature levels [Sall22].

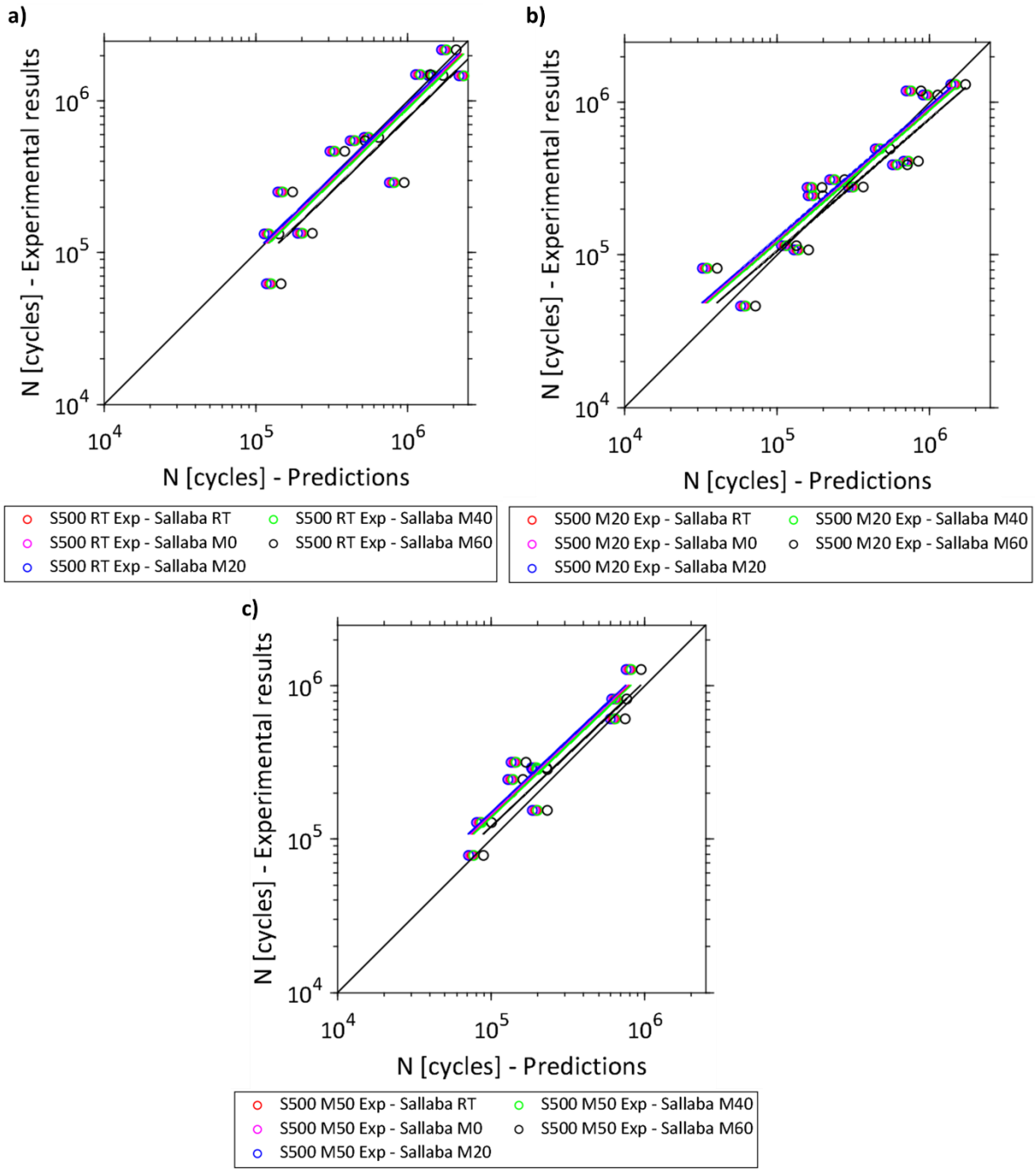

Figure 5.5: Comparison of numerical calculations of the fatigue lives with experimental results and different Paris Parameters for experiment at RT (a), -20°C (b) and -50°C (c)

The best fit lines in Figure 5.5 for the temperature levels of RT, 0°C, -20°C and -40°C are almost identical. In the experiments at RT Figure 5.5 (a), these four best fit lines are largely in concurrence with the 1:1-line. Only the best fit line from the -60°C Paris Parameter are below the 1:1-line, so the predicted fatigue lives are higher than the experimentally determined ones. For the experimental results at -20°C Figure 5.5 (b), the best fit line from the -60°C Paris Parameter is closer to the 1:1-line at low fatigue lives, at higher ones the other best fit lines show a higher agreement. The slope of the best fit lines deviates significantly from the 1:1-line in comparison to the other experimental temperatures. For the experimental results at -50°C

Figure 5.5 (c), the slope of the degrees of compensation and that of the 1:1-line do not completely match either. Here, however, for all fatigue lives, the best fit lines from the -60°C Paris Parameters show the highest agreement with the 1:1-line. The predicted results are nevertheless slightly lower than the experimental results.

5.6 Verification of the transverse stiffener at sub-zero temperatures

The procedure for the transversal stiffener is the same as for the C-joint, see Section 5.5. Table 5.3 presents the Paris parameters used in this section. As there are no parameters for the low temperature behaviour of the S235 specimens, the similarity of the behaviour between S235 and S500 should be checked first. Detailed information on the geometry and test parameters, as well as the calculated fatigue lives, can be found in Appendix A8.

Table 5.3: Parameter for Paris-Erdogan equation – transversal stiffener

Source	Material	Environment	Temperature	Units	C	m
IIW	Steel - BM	Air	≤ RT	$\left[N * mm^{-\frac{3}{2}}\right]$	$3*10^{-13}$	3
SALLABA et al. [SALL22]	S500 - BM	Air	RT	$\left[N * mm^{-\frac{3}{2}}\right]$	$3.02*10^{-14}$	3.38
SALLABA et al. [SALL22]	S500 - BM	Air	M0	$\left[N * mm^{-\frac{3}{2}}\right]$	$4.17*10^{-14}$	3.38
SALLABA et al. [SALL22]	S500 - BM	Air	M20	$\left[N * mm^{-\frac{3}{2}}\right]$	$2.92*10^{-14}$	3.38
SALLABA et al. [SALL22]	S500 - BM	Air	M40	$\left[N * mm^{-\frac{3}{2}}\right]$	$2.79*10^{-14}$	3.38
SALLABA et al. [SALL22]	S500 - BM	Air	M60	$\left[N * mm^{-\frac{3}{2}}\right]$	$1.962*10^{-14}$	3.38

Section 5.3 shows that the parameters from the IIW recommendations best describe the behaviour of S235 at RT. Figure 5.6 (a) shows the fatigue lives of the experiments with the parameters of the IIW recommendations for S235 and Figure 5.6 (b) shows these comparison for the S500 specimens with the parameters of SALLABA et al. [Sall22]. The plots show an equal stratification of the best fit lines for the different temperatures of the experiments despite high deviations in the slope for the results of the S235 specimens. Starting from the experimental results at RT to the results at -50°C, the experimentally determined fatigue lives become larger than the predicted ones. The behaviour for the S235 specimens and the S500 specimens is similar, in the following only experiments with S500 are simulated due to the lack of Paris parameters for S235.

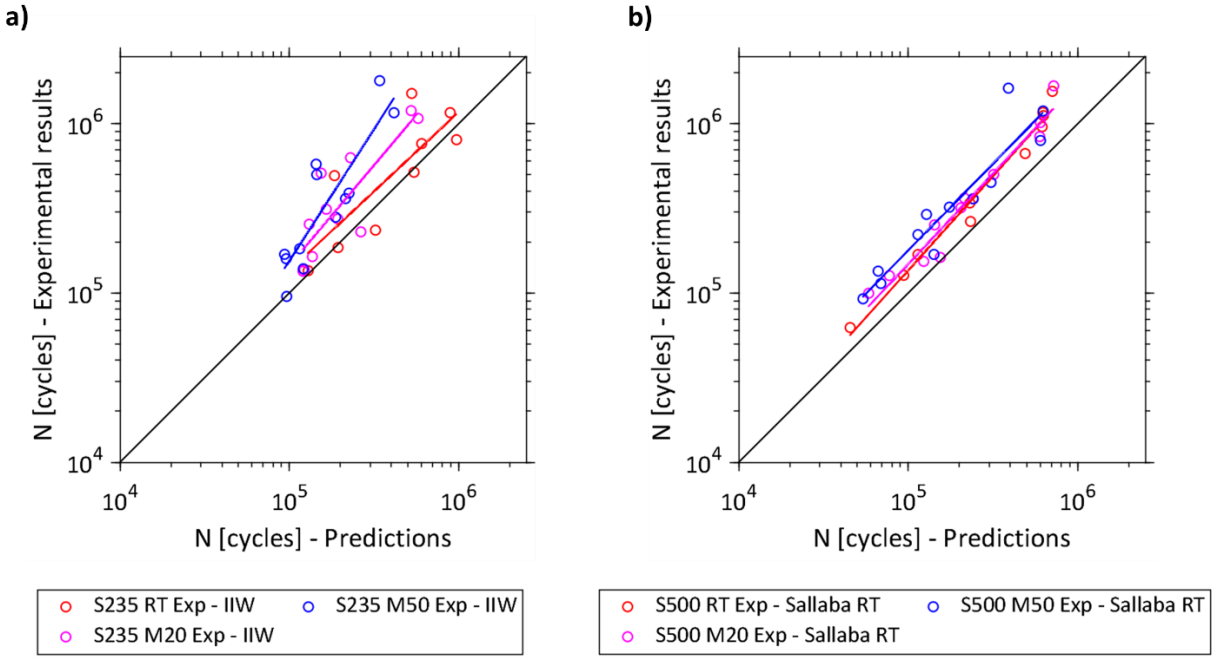

Figure 5.6: Comparison of analytical calculations of the fatigue lives with experimental results at different temperatures with same Paris Parameters for S235 specimens (a) and S500 specimens (b)

In Figure 5.7, the experimental fatigue lives of one test temperature are compared with the five Paris parameters of different temperature levels. Due to the constant *m* parameter, the first order best fit lines are parallel to each other. For all experimental temperatures, the best fit lines for RT, -20°C and -40°C are almost the same, while the best fit lines for -60°C show a larger gap, which is in line with the results in Section 5.5. The best fit lines for 0°C are also shifted from the other best fit lines, with regard to the fact that the temperature level is between RT and -20°C, a measurement inaccuracy is assumed for SALLABA et al. and the parameters are considered to be flawed [Sall22].Based on the experimental results at RT Figure 5.7 (a) to those at -50°C (c), the best fit lines are shifted in the direction of the experimental results. The shift from -20°C to -50°C is the largest. For all temperature levels, the best fit lines from the -60°C Paris Parameter show the highest agreement with the 1:1-line [Sall22].

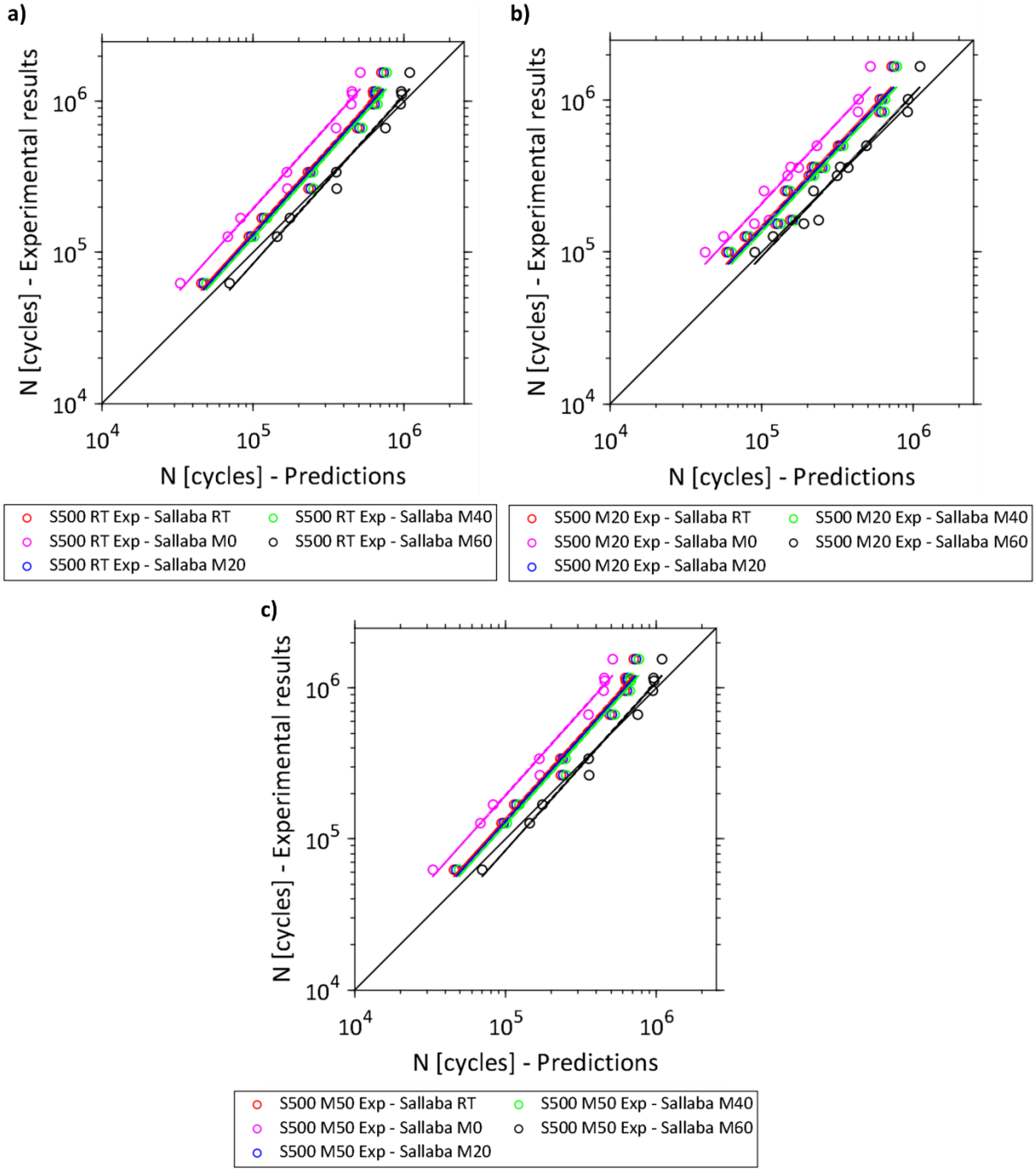

Figure 5.7: Comparison of analytical calculations of the fatigue lives with experimental results and different Paris Parameters for experiment at RT (a), -20°C (b) and -50°C (c)

6 Discussion

The comparisons of numerically and analytically determined fatigue lives with the experimentally determined fatigue lives in the previous Chapter 5 show that the crack growth can be simulated even at sub-zero temperatures and the fatigue life can be predicted with a high degree of accuracy. The differences between the predicted fatigue lives by using Paris parameters *C* and *m* from different sources, shows the high influence and the dependency of the predicted results from the Paris parameters. In Figure 5.2 and Figure 5.3 the experimental results at RT are compared with the predicted fatigue lives. For the prediction of the fatigue lives, the Paris parameters from the IIW recommendations and the BS7910 as well as the material specific Paris parameters from SALLABA et al., each applied to the same data set, have been used [Hobb16] [Brit15] [Sall22]. The boundary conditions of the experiments to be predicted were all within the specified application ranges that exist for the individual Paris parameters. Nevertheless, the predicted fatigue lives differ strongly from each other, while the parameters from the standards produced conservative values, for most cases a high agreement of the predicted fatigue lives with the real test results were achieved with the material-specific parameters. This result was expected, as the guidelines make little distinction between different steels, their mechanical properties and describe the upper bound, while the Paris parameters show material and temperature dependencies and describe the mean curves, see among others ALVARO et al. or SCHIJVE [Alva14] [Schi09]. In order to be able to predict the fatigue life of a welded joint with a high degree of accuracy, specific *C* and *m* parameters must be used for the application, but the tests to determine them are time consuming.

In the representation form in logarithmic space used in Chapter 5 for the comparison of the numerically simulated fatigue lives and the experimentally determined fatigue lives, the quality of the Paris parameters used is indicated by the congruence of a first-order best fit line with the 1:1-line, see Figure 6.1.

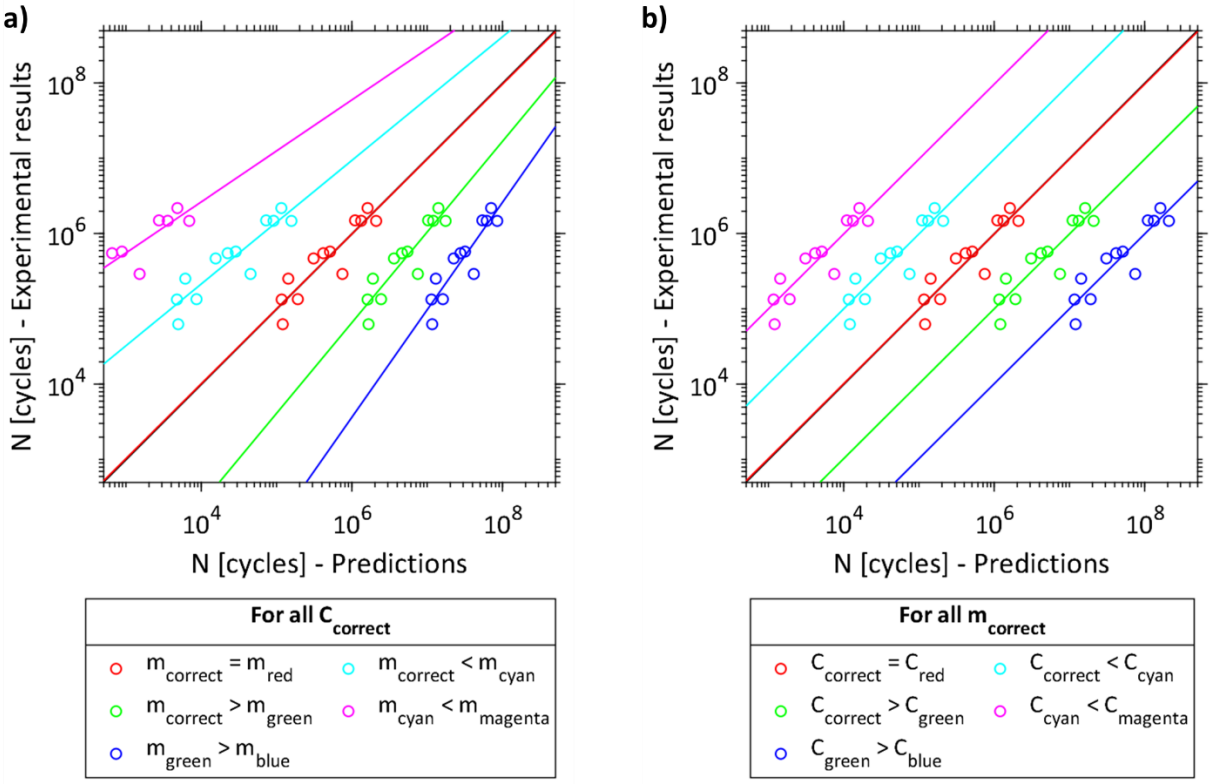

Figure 6.1: Example for the influence of the Paris parameters on the orientation of the best fit line first order to the 1:1-line, correct *C* parameter with different *m* parameters (a) and correct *m* parameter with different *C* parameters (b)

This representation form has the potential to simplify at least the validation process for *C* and *m* parameters. Due to the representation in the logarithmic space and the completed verification of the numerically determined SIFs, the slope of the first order best fit line depends only on the parameter *m*, all best fit lines are parallel to the 1:1-line, see Figure 6.1 (b). Whereas the displacement of the best fit lines from the 1:1-line are dependent from the parameters *m* and *C* but because *m* is known, *C* can also be determined. The parallelism of the lines for constant m is only existing in logarithmic space, this originates from the form of the Formulae (5.3. If the 1:1-line and the best fit line match, the Paris parameters used in the Paris-Erdogan equation represent the real FCG. Provided that the selected initial crack depth, the initial crack width, the aspect ratio, the point of transition from a semi-elliptical to a straight, continuous crack front and the specified point at which failure occurs are proper. As a data basis, no complicated constant ΔK experiments are necessary, but only comparably simple tests at constant stress on a resonance type fatigue testing machine.

Simplifying the Paris parameter determination process is highly relevant, as ALVARO et al. has shown that both slope and intercept in the Paris diagram for ferritic steels are dependent on sub-zero temperatures and thus the determination of a material specific Paris parameter pairing alone is not sufficient [Alva17]. The temperature dependence applies both above the FTT and below the FTT, whereby the dependencies below the FTT are much stronger [Alva17], see also Figure 2.9. The dependence of the Paris parameters on temperature is clearly visible in Figure 5.5 and Figure 5.7. When comparing the predicted fatigue lives resulting from the pa-

rameters determined by SALLABA et al., the best fit lines for the Paris parameters of the temperature levels RT, 0°C, -20°C and -40°C (BM and WM) are almost identical, i.e. they are little influenced by the temperature [Sall22]. While the best fit lines of the fatigue lives, determined with the Paris parameters of SALLABA et al. for the temperature level of -60°C, show a clear deviation [Sall22]. This indicates that there is a temperature related increase in fatigue life, whereby the rate of increase grows with decreasing material temperature, see the idealized example in Figure 6.2. Both plots show the same predicted values, the shift of the best fit lines results from the increase of the measured fatigue lives when the temperature decreases.

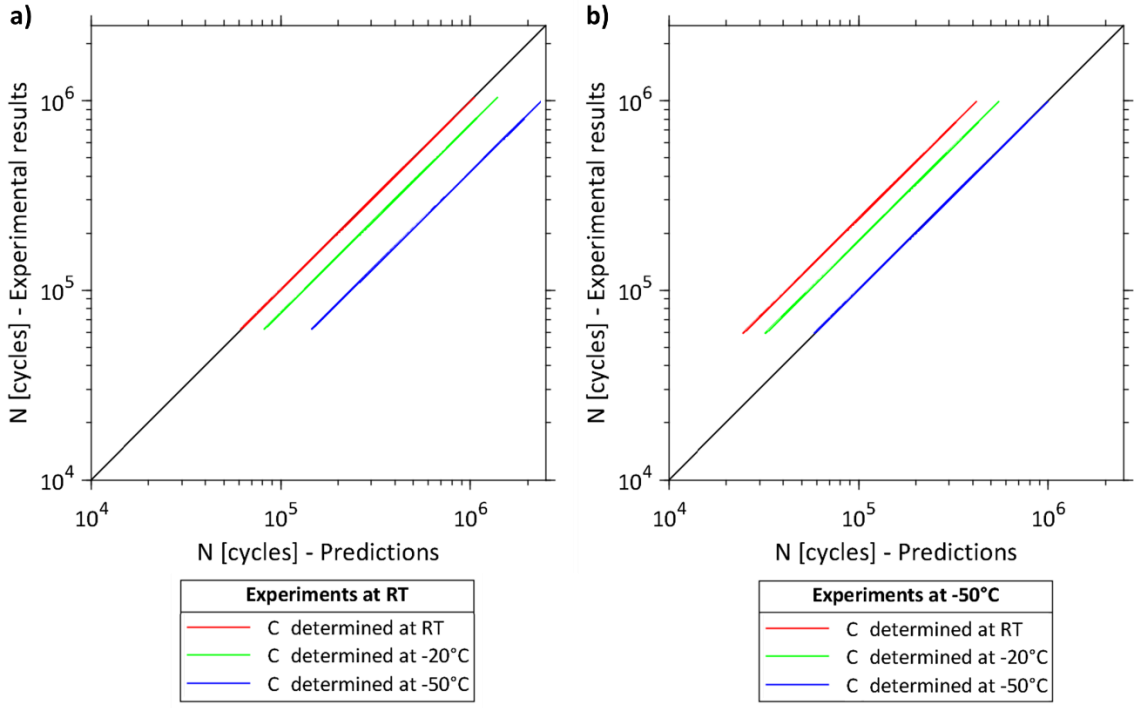

Figure 6.2: Idealised comparison of predicted and experimental fatigue lives determined via Paris parameter *C* determined at different temperatures, experiments at RT (a) and experiments at -50°C (b)

When determining the Paris parameters for different temperature levels, SALLABA et al. determined only *C* parameters for simplicity and assumed the *m* parameter to be constant between RT and -60°C [Sall22]. The simplification is based on the assumption that there is only a small temperature dependence of the *m* parameter above the FTT, which can be confirmed with Figure 5.5 and Figure 5.7. Despite the uniform *m* parameter, the slope of the best fit lines for experiments at RT as well as at -50°C largely coincides with the 1:1-line.

With regard to the question of whether the individual experiments are above or below the FTT, Figure 5.7 shows the relationship already described in the previous paragraph, namely that the fatigue life increases with decreasing temperature. From this observation, it can be concluded that all experiments in this plot were conducted above the FTT. Otherwise, a reduction of the experimentally determined fatigue lives should be observable. This observation is in line with the expectations based on the DBTT for the related BM of S500. The level of the DBTT of S500 is defined by the T_{50J} value, these are shown in Table 3.1 and is -119°C for the BM. From an assumed correlation between the FTT and the DBTT of a material, the FTT is

approximately 15°C - 20°C below the DBTT [Alva17] [Walt16]. The experiments shown in Figure 5.7 were therefore carried out far above the expected FTT. This is different for the experiments shown in Figure 5.5, where the failure of C-joints at the root has been examined. The T_{50J} value indicating the temperature of the DBTT is -39°C for the WM of S500 and the FTT can therefore be assumed to be close to the specimen temperature of -50°C. However, no decrease in fatigue lives associated with the transition to brittle fracture dominated failure can be observed in Figure 5.5. For the WM of the S235 material the DBTT is at a temperature of T_{27J} = -28°C, unfortunately no specific Paris parameters are available for different temperature levels of this material. However, Figure 5.4 plots the results of the experiments at RT, -20°C and -50°C, with the Paris parameters of SALLABA et al. for RT [Sall22]. Figure 5.4 shows on the one hand that the expected fatigue life increases steadily from RT over -20°C to -50°C, but also that in the experiments with a specimen temperature of -50°C there were 2 outliers among the 10 measurements. It can therefore be assumed that these two outliers have failed below the FTT. In addition, the fracture surfaces of the corresponding specimens show the characteristics of a brittle fracture, see Figure 6.3.

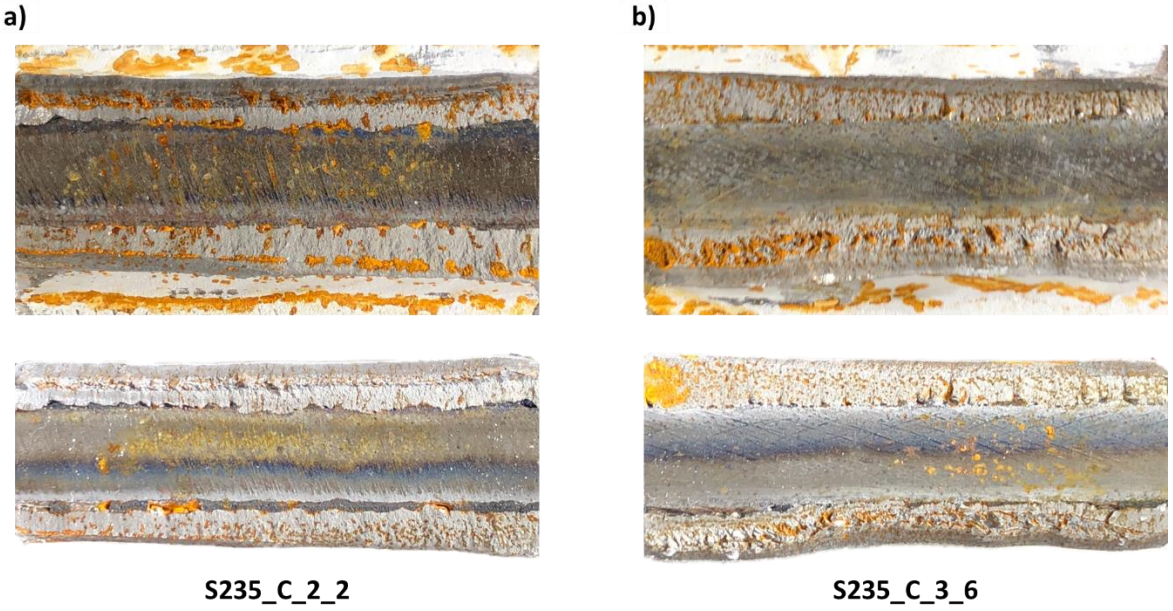

Figure 6.3: Fracture surfaces of two C-joint specimens with presumed break below the FTT

Assuming that the 2 outliers are specimens that failed below the FTT, the question is why 2 specimens are below the FTT and 8 are above the FTT, despite nearly identical test parameters. The temperature of the climatic chamber varies around ±1 °C, due to the heat capacity of the entire system of the resonance type fatigue testing machine, the fluctuations in the measurement temperature of the clamped specimen are even lower and can be excluded as the cause of the scatter. In the specimens, possible influencing factors on the scatter are the inhomogeneity of the material due to the directional solidification of the weld seam and the different strain rates of the WM, BM and the HAZ [Brau21a]. However, a comprehensive explanation does not yet exist. Regardless of the explanatory approach, it is clear that for a wide temperature range around the assumed FTT, there is a large uncertainty in the selection of the Paris parameters *C* and *m*. Averaging between the results of ductile and brittle failure is

not useful, it is mandatory to use the conservative Paris parameters, i.e. parameters for the brittle failure. This results in over dimensioning for the majority of welds sized for applications close to FTT.

With regard to the question of whether the fracture mechanics approach is suitable for simulating the failure of transversal stiffeners at the weld toe and C-joints at the weld root, it is useful to compare the plots in Figure 5.5 and Figure 5.7. The displacement of the first order best fit lines from the 1:1-line in Figure 5.5 is small for the different experimental temperatures. In contrast, for the transversal stiffeners with failure at the weld toe in Figure 5.7, a clear displacement of the best fit lines can be observed, the predicted fatigue lives are lower than the experimentally determined ones. It is not likely that these differences can be attributed to deviations in the determination of Paris parameter *C*, as the parameters were determined by the same person within the same work. A possible explanation for the different displacements is that for the root failure there is no long crack initiation period, but rather macro crack growth occurs immediately, starting from the unwelded gap. In the case of failure at the weld toe, on the other hand, there is a notable crack initiation period, and this period cannot be covered by the fracture mechanics approach alone. This is in contrast to the assumption by BRANCO et al. that due to pre-existing crack-like flaws there is virtually no crack initiation period for fatigue cracks at the weld toe [Bran99]. It can be concluded from this that the fracture mechanics approach is better suited for failure starting from the root than from the toe. An interesting observation is that despite the displacement of the best fit lines from the 1:1-line, the scatter of the predicted fatigue lives of the transversal stiffener around the degrees of compensation are not significantly larger than for the C-joint. With regard to the deviation between predicted and experimentally determined fatigue lives, it should be noted that the specimens contain residual stresses as a result of the welding process. Residual stresses have an influence on the fatigue lives, but they were not considered in the described prediction model [Al-M10].

7 Summary and Conclusion

The objective of this thesis has been achieved, which was to simulate weldments of different geometries at sub-zero temperatures using fracture mechanical methods. With regard to the quality of the results, respectively how well the simulation models reflect the behaviour of the real specimens, there are differences depending on the type of weldment and the location of the critical crack.

For the simulation of the fracture mechanical behaviour, the 2D FEM software Franc2D was used. With this software, the fracture mechanical behaviour of C-joints which are failing at the root could be simulated well, the deviations between the numerically and analytically determined SIFs are small and the fatigue lives calculated from the numerical SIFs agree with the values determined experimentally for that geometry. The high accuracy with which the root failure is simulated in Franc2D can be related to the crack origin, the initial defect and its shape. The unwelded gap that serves as the origin of the crack growth can be considered as an initial crack with a continuous crack front, this allows to simulate the SIFs of the real case accurately despite the reduction of the model to 2 dimensions and also to keep the modelling and computational effort low.

The two failure modes which were investigated and with Franc2D simulated are weld toe and weld root failure. In contrast to failure at the root, the crack growth for the weld toe failure does not start from a single initial crack with a continuous crack front, the unwelded gap. Instead, crack growth starts from one or more initial defects following the crack initiation period. These cracks initially grow both in depth and width and merge into a continuous crack front when they reach a certain depth. Because crack growth at short lengths determines most of the fatigue life and 3D crack growth occurs during this life stage for cracks failing at the weld toe, it can hardly be reproduced with 2D simulations. The agreement of the numerical calculation from Franc2D with reality is therefore low. According to FISCHER and FRICKE, it is, however, possible to modify the numerical 2D SIFs by modifying the dimensionless geometry factors M_K and M, together with a suitable aspect ratio a/c, and therefore to reproduce the to reality with them [Fisc12]. Therefore, Franc2D was still used in this thesis to simulate the failure at the weld toe, the numerically calculated SIFs could be validated successfully using 2D analytical formulas. However, as expected, the numerical SIFs from the 2D simulation could not be verified against the real experiments, so instead the 3D SIFs of the corresponding geometry were calculated analytically. These could be successfully verified on the real experiments.

With regard to the procedure for generating the numerical SIFs for the various geometries, parametric scripts that generate the geometries of the FEM models and a programme that automates the manual workflow in Franc2D were developed first. The parametric scripts and

the Franc2D controlling code have been embedded in a MATLAB script, allowing the whole simulation process to be run semi-automated. The geometry parameters and stresses to be simulated are read into the programme, the model is created, the simulation is conducted, the results are stored in tabular form and linked to the metadata. The result is a master file that contains among other data the analytical and numerical SIFs as well as the experimentally determined fatigue lives. With the master file specific parameters, such as specimen temperature, can be selected and stored in new file. It serves as the starting point for the calculation of the fatigue lives and the comparison with the real test results. The procedure described above has proven to be effective because a manual procedure would have been very time consuming due to the large number of tests and would probably have resulted in a large number of errors. Considering the high agreement of the numerical or analytical solutions with the experimental data and random checks of the data, it can be assumed that there are only a very small number of errors occurring during the generation of the SIFs.

When the fatigue life was estimated using the Paris-Erdogan equation and comparing the numerical or analytical values with the experimental data, a high level of correlation between the simulation and reality was reached, depending on the Paris parameters. However, it could also be shown that the influence of the Paris parameters on the simulation accuracy is very high and that the real FCG can only be simulated with material and temperature specific parameters. Using the Paris parameters provided in the International Standards and Guidelines, this is not possible. The fatigue lives calculated by them are very conservative. With the suitable parameters, the failure of both the C-joint at the root and the transversal stiffener at the weld toe were predicted well for the 3 temperatures of the RT, -20°C and -50°C experiments. Because there are not enough data regarding the failure of the C-joint at the weld toe, the corresponding model could not be verified and investigated further.

The logarithmic representation used to compare the predicted and experimentally determined fatigue lives has proven to be suitable beyond the mere visualisation of the results, in order to verify the Paris parameters *C* and *m* separately from each other, see Figure 6.1. The predicted and experimental fatigue lives are plotted on the x-axis and y-axis, respectively. The predicted and real fatigue lives agree if the measuring points lie on the 1:1-line. When now a first order best fit line is created using the individual measurement points, the deviation in slope of the resulting line to the 1:1-line represents the error in the Paris Parameter *m*. The displacement of the best fit line to the 1:1-line is dependent on both Paris parameters *C* and *m*, but because the slope is only dependent on the *m* Parameter, the *C* parameter can be verified based on the displacement. The clear attribution of the deviations is possible because the numerical SIFs have been validated using the analytical formulae and the representation in logarithmic space has been used, which is the result of extending the Paris-Erdogan equation by a logarithm:

$$log\left(\frac{da}{dN}\right) = m * log(\Delta K) + log(C) \tag{7.1}$$

A short literature research on methods of numerical determination of Paris parameters shows that there are already different approaches to determine Paris parameters by using numerical methods, see e.g. BRANCO et al. [Bran09]. A comparable method that uses the features of the

logarithmic space representation could not be found. Therefore, it makes sense to conduct further research on this advantageous relationship. More on this and other points arising from this work can be found in the following Chapter 8.

8 Future work

In the course of this thesis, questions arose that were beyond the scope of this thesis and could therefore not be conclusively addressed. One of these points is the distribution between the failure locations for the C-joint, some results indicate that the geometric limit curves are shifting within the sub-zero temperature range, see Figure 2.8. Differences in the mechanical properties of the BM, WM and HAZ could be the cause of a possible relocation of the limit curves, but so far there are too few measured data of C-joints that have failed at the weld toe. In a first step, C-joints specimens should be manufactured for which failure occurs at the weld toe according to the previous limit curves at RT. With this measurement data, the FEM model developed in this thesis, can be verified and based on this model, an investigation of the failure distribution at sub-zero temperatures can be conducted.

Another question is, what influence single and combinations of geometry parameters have on the fatigue life of the different weldments. In particular, the question if and how the influence of the geometry parameters changes at different temperature levels would be interesting. For example, does the influence of the plate thickness T change compared with the weldment height H, while the material of the plate can be divided into BM and a HAZ, whereas the weldment consists only of WM. To answer this question, the already existing data of the conducted tests can be used, in the selection script for the master file, geometry parameters must be added in the script as selection parameters.

For the determination of the fatigue life, the crack growth at short crack lengths is of high importance. In the case of failure at the weld toe, the crack grows from the connection point between the weldment and the plate, this point is always located in the HAZ. In the presentation of this thesis, however, a distinction has only been made between BM and WM. The material in the HAZ has not been considered due to the high complicity of the material in this area. A further investigation of the influencing parameters in the form of a literature research as well as fracture surface investigations would be useful. Together with the knowledge obtained, a 3D model can be created on which crack propagation simulations can be carried out, in which various material parameters (HAZ, BM), different crack fronts and crack initiation points should be simulated.

For an accurate fracture mechanics simulation of the fatigue life, material and temperature specific Paris parameters are necessary. However, their determination is time consuming and therefore expensive. For this reason, investigations should be carried out to determine whether the Paris-Erdogan equation can be extended to include corresponding dependency relationships, an example of this could be the master curve approach for fracture toughness

$K_{Ic,median}$ by WALLIN [Wall99]. Alternatively, it could be investigated whether the approach described in this thesis for the verification of C and m can be used to determine them directly.

9 Bibliography

[Akse17] Akselsen, O. M.; Ren, X.; Alvaro, A.; Nyhus, B.: Key Challenges in Materials and Welding for Application of Steel Structures in Arctic. In (Reza, A.; A. Ott, B. Hrsg.): ISOPE - International Offshore and Polar Engineering Conference. Proceedings. International Society of Offshore & Polar Engineers, 2017; pp. 282–289.

[Al-M10] Al-Mukhtar, A.: The safety analysis concept of welded components under cyclic loads using fracture mechanics method. Dissertation, 2010.

[Alva14] Alvaro, A.; Akselsen, O. M.; Ren, X.; Kaneko, A.: Fundamental Aspects of Fatigue of Steel in Arctic Applications. In (Chung, J. S. et al. Hrsg.): Proceedings of the Twenty-fourth (2014) International Offshore and Polar Engineering Conference. International Society of Offshore and Polar Engineers (ISOPE), 2014; pp. 247–254.

[Alva17] Alvaro, A.; Akselsen, O. M.; Ren, X.; Perillo, G.; Nyhus, B.: On the Relation between Fatigue and Static Ductile to Brittle Transition for Weld Simulated 420 MPa Structural Steel. In (Chung, J. S. et al. Hrsg.): ISOPE - International Offshore and Polar Engineering Conference. Proceedings. International Society of Offshore & Polar Engineers, 2017; pp. 298–303.

[ASTM03] ASTM International: ASTM E1921-21. Standard Test Method for Determination of Reference Temperature, To, for Ferritic Steels in the Transition Range, United States, 2003.

[Augu22] August Dreckshage GmbH & Co. KG: Nichteisenmetalle (NE-Metalle) I August Dreckshage I Bielefeld. https://dreckshage.de/de/werkstoffe/ne-metalle, 18.01.2022.

[Bown02] Bowness, D.; Lee, M. M.K.: Fracture mechanics assessment of fatigue cracks in offshore tubular structures. HSE Books, London, 2002. ISBN 0-7176-2328-9.

[Bran09] Branco, R.; Antunes, F. V.; Martins Ferreira, J. A.; Silva, J. M.: Determination of Paris law constants with a reverse engineering technique. In Engineering Failure Analysis, 2009, 16; pp. 631–638. doi:10.1016/j.engfailanal.2008.02.004.

[Bran99] Branco, C.; Maddox, S. J.; Infante, V.; Gomes, E. C.: Fatigue performance of tungsten inert gas (TIG) and plasma welds in thin sections. In International Journal of Fatigue, 1999, 21; pp. 587–601. doi:10.1016/S0142-1123(98)00084-X.

[Brau20a] Braun, M.; Scheffer, R.; Fricke, W.; Ehlers, S.: Fatigue strength of fillet-welded joints at subzero temperatures. In Fatigue & Fracture of Engineering Materials & Structures, 2020a, 43; pp. 403–416. doi:10.1111/ffe.13163.

[Brau20b] Braun, M.; Milaković, A.-S.; Renken, F.; Fricke, W.; Ehlers, S.: Application of local approaches to the assessment of fatigue test results obtained for welded joints at sub-zero temperatures. In International Journal of Fatigue, 2020b, 138. doi:10.1016/j.ijfatigue.2020.105672.

[Brau21a] Braun, M.: Assessment of fatigue strength of welded steel joints at sub-zero temperatures based on the micro-structural support effect hypothesis. Dissertation, Hamburg, 2021a.

[Brau21b] Braun, M.; Kahl, A.; Willems, T.; Seidel, M.; Fischer, C.; Ehlers, S.: Guidance for Material Selection Based on Static and Dynamic Mechanical Properties at Sub-Zero Temperatures. In Journal of Offshore Mechanics and Arctic Engineering, 2021b, 143. doi:10.1115/1.4049252.

[Brau22] Braun, M.; Dörner, A.; ter Veer, K. F.; Willems, T.; Seidel, M.; Hendrikse, H.; Høyland, K. V.; Fischer, C.; Ehlers, S.: Development of Combined Load Spectra for Offshore Structures Subjected to Wind, Wave, and Ice Loading. In Energies, 2022, 15. doi:10.3390/en15020559.

[Brit15] British Standards Institution: Guide to methods for assessing the acceptability of flaws in metallic structures. BS 7910:2013+A1:2015, 2015.

[Depa17] Department of Applied Mechanics: Ansys APDL Definitions. PLANE183 Element Description. https://www.mm.bme.hu/~gyebro/files/ans_help_v182/ans_elem/Hlp_E_PLANE183.html, 09.12.2021.

[Enge83] Engesvik, K. M.; Moan, T.: Probabilistic analysis of the uncertainty in the fatigue capacity of welded joints. In Engineering Fracture Mechanics, 1983, 18; pp. 743–762. doi:10.1016/0013-7944(83)90122-4.

[Fisc12] Fischer, C.; Fricke, W.: Simulation des zyklischen Rissfortschritts- und der Rissform an lasttragenden Kreuzstößen: ANSYS Conference & 30th User's Meeting, 2012.

[Fisc16] Fischer, C.: Bewertung der Schwingfestigkeit von Schweißverbindungen mittels der Formänderungsenergiedichte. Dissertation, Technische Universität Hamburg-Harburg, 2016. ISBN 978-3-8440-4400-3.

[Frau22] Fraunhofer-Institut für Werkstoffmechanik IWM: Schweißverbindungen - Fraunhofer IWM. https://www.iwm.fraunhofer.de/de/warum-fraunhofer-iwm/loesungen-fuer-produktlebenzyklus/schweissverbindungen.html, 17.01.2022.

[Fric12] Fricke, W.: IIW recommendations for the fatigue assessment of welded structures by notch stress analysis. Woodhead Publishing Limited, 2012. ISBN 978-0-85709-855-9.

[Fric13] Fricke, W.: IIW guideline for the assessment of weld root fatigue. In Welding in the World, 2013, 57; pp. 753–791. doi:10.1007/s40194-013-0066-y.

[Fric17] Fricke, W.: Lectures on fatigue strength of ships and offshore structures, Hamburg, 2017.

[Hobb16] Hobbacher, A. F.: Recommendations for Fatigue Design of Welded Joints and Components. Springer International Publishing, Cham, 2016. ISBN 978-3-319-23756-5.

[Kain06] Kainuma, S.; Mori, T.: A fatigue strength evaluation method for load-carrying fillet welded cruciform joints. In International Journal of Fatigue, 2006, 28; pp. 864–872. doi:10.1016/j.ijfatigue.2005.10.004.

[Lang19] Langenberg, P.; Kucharczyk, P.; Pilhagen, J.; Stranghöner, N.; Schedin, E.: Application of the Master Curve concept on the choice of duplex stainless steel to avoid brittle fracture. In ce/papers, 2019, 3; pp. 913–918. doi:10.1002/cepa.1152.

[Madd74] Maddox, S. J.: Assessing the significance of flaws in welds subject to fatigue. In Welding Journal Research Supplement, 1974; pp. 401–409.

[Newm81] Newman, J. C.; Raju, I. S.: An empirical stress-intensity factor equation for the surface crack. In Engineering Fracture Mechanics, 1981, 15; pp. 185–192. doi:10.1016/0013-7944(81)90116-8.

[Oh15] Oh, D.-J.; Lee, J.-M.; Noh, B.-J.; Kim, W.-S.; Ryuichi-Ando; Toshiyuki-Matsumoto; Kim, M.-H.: Investigation of fatigue performance of low temperature alloys for liquefied natural gas storage tanks. In Proceedings of the Institution of Mechanical Engineers, Part C: Journal of Mechanical Engineering Science, 2015, 229; pp. 1300–1314. doi:10.1177/0954406215569255.

[Renk21] Renken, F.; Bock und Polach, R. U. F. von; Schubnell, J.; Jung, M.; Oswald, M.; Rother, K.; Ehlers, S.; Braun, M.: An algorithm for statistical evaluation of weld toe geometries using laser triangulation. In International Journal of Fatigue, 2021, 149. doi:10.1016/j.ijfatigue.2021.106293.

[Sall20] Sallaba, F.: Investigation of fatigue ductile-brittle transition in steel and welded joints. Master Thesis, 2020.

[Sall22] Sallaba, F.; Rolof, F.; Ehlers, S.; Walters, C. L.; Braun, M.: Relation between the Fatigue and Fracture Ductile-Brittle Transition in S500 Welded Steel Joints. In Metals, submitted for publication (2022).

[Schi09] Schijve, J.: Fatigue of Structures and Materials. Springer Netherlands, Dordrecht, 2009. ISBN 978-1-4020-6807-2.

[Schu20] Schubnell, J.; Jung, M.; Le, C. H.; Farajian, M.; Braun, M.; Ehlers, S.; Fricke, W.; Garcia, M.; Nussbaumer, A.; Baumgartner, J.: Influence of the optical measurement technique and evaluation approach on the determination of local weld geometry parameters for different weld types. In Welding in the World, 2020, 64; pp. 301–316. doi:10.1007/s40194-019-00830-0.

[Song21] Song, W.; Liu, X.; Xu, J.; Fan, Y.; Shi, D.; He, M.; Wang, X.; Berto, F.: Fatigue fracture assessment of 10CrNi3MoV welded load-carrying cruciform joints considering mismatch effect. In Fatigue & Fracture of Engineering Materials & Structures, 2021, 44; pp. 1739–1759. doi:10.1111/ffe.13457.

[Wall99] Wallin, K.: Statistical re-evaluation of the ASME KIC and KIR fracture toughness reference curves. In Nuclear Engineering and Design, 1999, 193; pp. 317–326. doi:10.1016/S0029-5493(99)00187-9.

[Walt16] Walters, C. L.; Alvaro, A.; Maljaars, J.: The effect of low temperatures on the fatigue crack growth of S460 structural steel. In International Journal of Fatigue, 2016, 82; pp. 110–118. doi:10.1016/j.ijfatigue.2015.03.007.

[Zerb14] Zerbst, U.; Ainsworth, R. A.; Beier, H.T.; Pisarski, H.; Zhang, Z. L.; Nikbin, K.; Nitschke-Pagel, T.; Münstermann, S.; Kucharczyk, P.; Klingbeil, D.: Review on fracture and crack propagation in weldments – A fracture mechanics perspective. In Engineering Fracture Mechanics, 2014, 132; pp. 200–276. doi:10.1016/j.engfracmech.2014.05.012.

Appendix

A1 Formulas for iterative crack growth calculations

M_k for the deepest point of a transversal stiffener

$$A_1 = -1.0343 * \left(\frac{a}{c}\right)^2 - 0.15657 * \frac{a}{c} + 1.3409 \tag{A.1}$$

$$A_2 = 1.3218 * \left(\frac{a}{c}\right)^{-0.61153} \tag{A.2}$$

$$A_3 = -0.87238 * \frac{a}{c} + 1.2788 \tag{A.3}$$

$$A_4 = -0.46190 * \left(\frac{a}{c}\right)^3 + 0.67090 * \left(\frac{a}{c}\right)^2 - 0.37571 * \frac{a}{c} + 4.6511 \tag{A.4}$$

$$f_1 = 0.43358 * \left(\frac{a}{T}\right)^{A_1 + \left(A_2 * \frac{a}{T}\right)^{A_3}} + 0.93163 * \exp\left(\frac{a}{T}\right)^{-0.050966} + A_4 \tag{A.5}$$

$$A_5 = -0.00038737 * \theta^2 + 0.64771 * \theta - 0.72368 \tag{A.6}$$

$$A_6 = 0.24183 * \theta + 176.23 \tag{A.7}$$

$$A_7 = -0.00027743 * \theta + 2.8143 \tag{A.8}$$

$$f_2 = A_5 * \left(1 - \frac{a}{T}\right)^{A_6} + A_7 * \left(\frac{a}{T}\right)^{-0.10740 * \frac{a}{T}} \tag{A.9}$$

$$A_8 = -0.082502 * \theta^2 + 0.0084862 * \theta + 0.38417 \tag{A.10}$$

$$A_9 = 0.010766 * \left(\frac{L}{T}\right)^3 - 0.060159 * \left(\frac{L}{T}\right)^2 + 0.13667 * \frac{L}{T} - 0.023400 \tag{A.11}$$

$$A_{10} = -0.028378 * \left(\frac{L}{T}\right)^3 + 0.16489 * \left(\frac{L}{T}\right)^2 - 0.35584 * \frac{L}{T} - 0.00024554 \tag{A.12}$$

$$A_{11} = -0.0015061 * \left(\frac{L}{T}\right)^2 + 0.023369 * \frac{L}{T} - 0.23124 \tag{A.13}$$

$$A_{12} = 0.051554 * \theta^2 + 0.025447 * \theta + 1.8975 \tag{A.14}$$

$$A_{13} = -0.12914 * \theta^2 + 0.21863 * \theta + 0.13798 \tag{A.15}$$

$$A_{14} = -0.20136 * \left(\frac{L}{T}\right)^2 + 0.93311 * \frac{L}{T} - 0.41496 \tag{A.16}$$

$$A_{15} = 0.20188 * \left(\frac{L}{T}\right)^2 - 0.97857 * \frac{L}{T} + 0.068225 \tag{A.17}$$

$$A_{16} = -0.027338 * \left(\frac{L}{T}\right)^2 + 0.12551 * \frac{L}{T} - 11.218 \tag{A.18}$$

$$f_3 = A_8 * \left(\frac{a}{T}\right)^{A_9 * \theta^2 + A_{10} * \theta + A_{11}} + A_{12} * \left(\frac{a}{T}\right)^{A_{13}} + \left(A_{14} * \left(\frac{a}{T}\right)^2 + A_{15} * \frac{a}{T} + A_{16}\right) \tag{A.19}$$

$$M_{ka} = f_1 + f_2 + f_3 \tag{A.20}$$

M for the surface of a transversal stiffener

$$M_c = \left(M_1 + M_2 * \left(\frac{a}{T}\right)^2 + M_3 * \left(\frac{a}{T}\right)^4\right) * \frac{f_w * f_\Phi * g}{Q} \tag{A.21}$$

$$M_1 = 1.13 - 0.09 * \left(\frac{a}{c}\right) \tag{A.22}$$

$$M_2 = -0.54 + \left(\frac{0.89}{0.2 + \left(\frac{a}{c}\right)}\right) \tag{A.23}$$

$$M_3 = 0.5 - \left(\frac{1}{0.65 + \left(\frac{a}{c}\right)}\right) + 14 * \left(1 - \left(\frac{a}{c}\right)\right)^{24} \tag{A.24}$$

$$f_w = \sqrt{\sec\left(\frac{\pi}{2} * \frac{a}{T} * \left(\frac{c}{b}\right)^{0.5}\right)} \tag{A.25}$$

$$f_\Phi = \left(\left(\frac{c}{a}\right)^2 * (\cos(0))^2 + (\sin(0))^2\right)^{0.25} \tag{A.26}$$

$$g = 1 + \left(0.1 + 0.35 * \left(\frac{c}{b}\right)^2\right) * (1 - \sin(0))^2 \tag{A.27}$$

$$\mathrm{Q} = \sqrt{\left(1 + 1.464 * \left(\frac{c}{a}\right)^{1.65}\right)} \tag{A.28}$$

M_k for the surface of a transversal stiffener

$$A_1 = 0.0078157 * \left(\frac{c}{a}\right)^2 - 0.070664 * \left(\frac{c}{a}\right) + 1.8508 \tag{A.29}$$

$$A_2 = -0.000054546 * \left(\frac{L}{T}\right)^2 + 0.00013651 * \left(\frac{L}{T}\right) - 0.00047844 \tag{A.30}$$

$$A_3 = 0.00049192 * \left(\frac{L}{T}\right)^2 - 0.0013595 * \left(\frac{L}{T}\right) + 0.011400 \tag{A.31}$$

$$A_4 = 0.0071654 * \left(\frac{L}{T}\right)^2 - 0.033399 * \left(\frac{L}{T}\right) - 0.25064 \tag{A.32}$$

$$A_5 = -0.018640 * \left(\frac{c}{a}\right)^2 + 0.24311 * \left(\frac{c}{a}\right) - 1.7644 \tag{A.33}$$

$$A_6 = -0.0016713 * \left(\frac{L}{T}\right)^2 + 0.0090620 * \left(\frac{L}{T}\right) - 0.016479 \tag{A.34}$$

$$A_7 = -0.0031615 * \left(\frac{L}{T}\right)^2 - 0.010944 * \left(\frac{L}{T}\right) + 0.13967 \tag{A.35}$$

$$A_8 = -0.045206 * \left(\frac{L}{T}\right)^3 + 0.32380 * \left(\frac{L}{T}\right)^2 - 0.68935 * \left(\frac{L}{T}\right) + 1.4954 \quad \text{(A.36)}$$

$$f_1 = A_1 * \left(\frac{a}{T}\right)^{A_2*\left(\frac{c}{a}\right)^2 + A_3*\left(\frac{c}{a}\right) + A_4} + A_5 * \left(1 - \frac{a}{T}\right)^{A_6*\left(\frac{c}{a}\right)^2 + A_7*\left(\frac{c}{a}\right) + A_8} \quad \text{(A.37)}$$

$$A_9 = 0.15209 * \Theta^2 + 0.0029155 * \Theta - 0.38250 \quad \text{(A.38)}$$

$$A_{10} = -0.24523 * \Theta^2 + 0.0013244 * \Theta + 0.50434 \quad \text{(A.39)}$$

$$A_{11} = -0.64023 * \Theta^2 + 2.2642 * \Theta + 0.25959 \quad \text{(A.40)}$$

$$A_{12} = -0.25473 * \left(\frac{a}{c}\right)^2 + 0.40928 * \left(\frac{a}{c}\right) + 0.0021892 \quad \text{(A.41)}$$

$$A_{13} = -0.11458 * \Theta^2 + 0.72927 * \Theta - 0.22760 \quad \text{(A.42)}$$

$$A_{14} = 37.423 * \left(\frac{a}{c}\right)^2 - 15.741 * \left(\frac{a}{c}\right) + 64.903 \quad \text{(A.43)}$$

$$f_2 = \left(A_9 * \left(\frac{a}{c}\right)^2 + A_{10} * \left(\frac{a}{c}\right) + A_{11}\right) * \left(\frac{a}{T}\right)^{A_{12}} + A_{13} * \left(1 - \frac{a}{T}\right)^{A_{14}} \quad \text{(A.44)}$$

$$A_{15} = -0.14475 * \left(\frac{L}{T}\right)^2 + 0.51648 * \left(\frac{L}{T}\right) - 0.18189 \quad \text{(A.45)}$$

$$A_{16} = 0.34950 * \left(\frac{L}{T}\right)^2 - 1.3069 * \left(\frac{L}{T}\right) + 1.0641 \quad \text{(A.46)}$$

$$A_{17} = -0.10553 * \left(\frac{L}{T}\right)^3 + 0.41373 * \left(\frac{L}{T}\right)^2 - 0.38632 * \left(\frac{L}{T}\right) - 1.9885 \quad \text{(A.47)}$$

$$A_{18} = 1.8225 * \Theta^2 - 4.5008 * \Theta + 3.1650 \quad \text{(A.48)}$$

$$A_{19} = 0.041574 * \left(\frac{L}{T}\right)^2 - 0.16138 * \left(\frac{L}{T}\right) + 0.14184 \quad \text{(A.49)}$$

$$A_{20} = -0.098912 * \left(\frac{L}{T}\right)^2 + 0.39688 * \left(\frac{L}{T}\right) - 0.58821 \quad \text{(A.50)}$$

$$A_{21} = 0.043891 * \left(\frac{L}{T}\right)^3 - 0.19694 * \left(\frac{L}{T}\right)^2 + 0.23516 * \left(\frac{L}{T}\right) + 0.97585 \quad \text{(A.51)}$$

$$A_{22} = -0.046138 * \left(\frac{a}{c}\right)^2 - 0.12171 * \left(\frac{a}{c}\right) + 1.6277 \quad \text{(A.52)}$$

$$A_{23} = 0.088591 * \left(\frac{a}{c}\right)^2 + 0.27816 * \left(\frac{a}{c}\right) - 4.0124 \quad \text{(A.53)}$$

$$A_{24} = -0.052530 * \left(\frac{a}{c}\right)^2 - 0.13902 * \left(\frac{a}{c}\right) + 2.6646 \quad \text{(A.54)}$$

$$f_3 = (A_{15} * \Theta^2 + A_{16} * \Theta + A_{17}) * \left(\frac{a}{T}\right)^{A_{18}} + (A_{19} * \Theta^2 + A_{20} * \Theta + A_{21}) * \exp\left(\frac{a}{T}\right)^{A_{22}*\Theta^2 + A_{23}*\Theta + A_{24}} \quad \text{(A.55)}$$

$$M_{kc} = f_1 * f_2 * f_3 \quad \text{(A.56)}$$

A2 Analytical and numerical SIFs with deviations for the C-joint – root failure

Table A.1: Deviations between analytical and numerical $\Delta\overline{K}_I$

a [mm]	$\Delta\overline{K}_{I,analytical}\left[\frac{N}{mm^{1.5}}\right]$	$\Delta\overline{K}_{I,franc,open}\left[\frac{N}{mm^{1.5}}\right]$	Deviation - $\Delta\overline{K}_{I,franc,open}$ [%]	$\Delta\overline{K}_{I,franc,full}\left[\frac{N}{mm^{1.5}}\right]$	Deviation - $\Delta\overline{K}_{I,franc,full}$ [%]
5.10	281.69	279.21	0.88	281.88	-0.07
5.20	285.60	281.34	1.49	285.79	-0.07
5.30	289.56	288.82	0.25	291.19	-0.56
5.40	293.57	297.87	-1.47	299.52	-2.03
5.50	297.63	300.43	-0.94	298.05	-0.14
5.60	301.75	305.03	-1.09	302.72	-0.32
5.70	305.93	309.15	-1.05	310.31	-1.43
5.80	310.18	307.52	0.86	314.01	-1.24
5.90	314.49	314.38	0.04	315.49	-0.32
6.00	318.87	325.63	-2.12	315.24	1.14
6.10	323.33	328.39	-1.56	324.37	-0.32
6.20	327.87	330.04	-0.66	335.88	-2.45
6.30	332.49	337.28	-1.44	340.26	-2.34
6.40	337.19	346.31	-2.70	341.04	-1.14
6.50	341.99	350.05	-2.36	347.25	-1.54
6.60	346.88	351.42	-1.31	355.43	-2.47
6.70	351.87	359.05	-2.04	356.22	-1.24
6.80	356.97	368.32	-3.18	364.72	-2.17
6.90	362.18	369.77	-2.10	375.37	-3.64
7.00	367.50	377.47	-2.71	379.05	-3.14
7.10	372.95	385.33	-3.32	387.07	-3.79
7.20	378.52	392.79	-3.77	396.12	-4.65
7.30	384.22	403.39	-4.99	401.14	-4.41
7.40	390.06	403.83	-3.53	405.01	-3.83
7.50	396.05	403.06	-1.77	413.13	-4.31
7.60	402.19	417.51	-3.81	422.39	-5.02
7.70	408.50	432.75	-5.94	423.41	-3.65
7.80	414.97	440.17	-6.07	429.60	-3.53
7.90	421.62	444.77	-5.49	445.15	-5.58
8.00	428.46	434.64	-1.44	457.22	-6.71
8.10	435.49	449.31	-3.17	464.46	-6.65
8.20	442.74	479.55	-8.31	472.90	-6.81

8.30	450.20	488.30	-8.46	477.71	-6.11
8.40	457.89	495.82	-8.28	490.33	-7.09
8.50	465.83	496.50	-6.58	508.52	-9.16
8.60	474.02	511.69	-7.95	514.45	-8.53
8.70	482.49	535.83	-11.05	515.83	-6.91
8.80	491.25	545.66	-11.08	534.28	-8.76
8.90	500.31	558.99	-11.73	559.63	-11.86
9.00	509.70	571.73	-12.17	569.96	-11.82

A3 Analytical and numerical SIFs with deviations for the transversal stiffener

Table A.2: Deviations between analytical and numerical $\Delta\overline{K}_I$

a [mm]	$\Delta\overline{K}_{I,franc}\left[\frac{N}{mm^{1.5}}\right]$	$\Delta\overline{K}_{I,analytical,2D}\left[\frac{N}{mm^{1.5}}\right]$	Deviation - $\Delta\overline{K}_{I,analytical,2D}$ [%]	$\Delta\overline{K}_{I,analytical,3D}\left[\frac{N}{mm^{1.5}}\right]$	Deviation - $\Delta\overline{K}_{I,analytical,3D}$ [%]
0.10	160.35	162.25	3.77	129.91	-23.44
0.20	185.91	187.66	2.79	147.11	-26.38
0.30	202.46	205.21	3.11	159.41	-27.00
0.40	212.62	219.15	4.87	169.76	-25.25
0.50	221.79	230.93	6.13	179.01	-23.89
0.60	229.84	241.27	7.29	187.54	-22.56
0.70	240.56	250.56	7.08	195.52	-23.04
0.80	253.47	259.06	5.91	203.08	-24.81
0.90	263.31	266.95	5.84	210.30	-25.21
1.00	272.27	274.37	6.03	217.23	-25.34
1.10	278.93	281.40	6.96	223.93	-24.56
1.20	291.27	288.11	5.98	230.43	-26.41
1.30	304.94	294.57	4.68	236.75	-28.80
1.40	315.03	300.82	4.56	242.93	-29.68
1.50	324.40	306.89	4.70	248.97	-30.30
1.60	331.94	312.82	5.39	254.91	-30.22
1.70	345.32	318.64	4.47	260.74	-32.44
1.80	360.45	324.36	3.20	266.50	-35.25
1.90	372.08	330.01	2.96	272.19	-36.70
2.00	381.93	335.60	3.25	277.82	-37.47
2.10	386.82	341.15	4.81	283.40	-36.49
2.20	403.03	346.67	3.64	288.94	-39.49
2.30	424.26	352.17	1.45	294.44	-44.09
2.40	435.36	357.66	1.74	299.93	-45.15

2.50	441.85	363.15	3.10	305.40	-44.68
2.60	459.70	368.66	2.05	310.86	-47.88
2.70	483.72	374.17	-0.13	316.32	-52.92
2.80	496.04	379.71	0.26	321.79	-54.15
2.90	503.60	385.28	1.65	327.26	-53.88
3.00	523.57	504.65	0.71	391.30	-33.81
3.10	549.21	669.91	-1.12	471.95	-16.37
3.20	563.57	698.35	-0.71	488.45	-15.38
3.30	583.42	728.48	-1.17	505.75	-15.36
3.40	596.58	760.41	-0.35	523.90	-13.87
3.50	617.40	795.03	-0.60	542.95	-13.71
3.60	647.98	834.60	-1.90	562.93	-15.11
3.70	665.54	878.77	-0.73	583.91	-13.98
3.80	674.70	925.70	1.75	605.93	-11.35
3.90	702.68	975.57	1.57	629.04	-11.71
4.00	742.56	1028.58	-0.03	653.31	-13.66
4.10	767.99	1084.94	0.55	678.77	-13.14
4.20	790.47	1144.88	1.63	705.50	-12.04
4.30	807.87	1208.65	3.43	733.55	-10.13
4.40	844.36	1276.48	3.08	762.98	-10.67
4.50	881.47	1348.66	2.88	793.85	-11.04
4.60	907.67	1425.47	4.04	826.23	-9.86
4.70	934.97	1507.23	5.20	860.18	-8.69
4.80	978.48	1594.24	4.89	895.78	-9.23
4.90	1031.57	1686.88	3.92	933.08	-10.56
5.00	1064.23	1785.50	5.05	972.16	-9.47

A4 Analytical and numerical SIFs with deviations for the C-joint – root failure

Table A.3: Deviations between analytical and numerical $\Delta\overline{K}_I$

a [mm]	$\Delta\overline{K}_{I,franc}\left[\frac{N}{mm^{1.5}}\right]$	$\Delta\overline{K}_{I,analytical,2D}\left[\frac{N}{mm^{1.5}}\right]$	Deviation - $\Delta\overline{K}_{I,analytical,2D}$ [%]	$\Delta\overline{K}_{I,analytical,3D}\left[\frac{N}{mm^{1.5}}\right]$	Deviation - $\Delta\overline{K}_{I,analytical,3D}$ [%]
0.10	209.94	240.21	12.60	195.57	-7.35
0.20	245.82	260.62	5.68	224.11	-9.69
0.30	272.22	274.85	0.96	239.34	-13.74
0.40	283.78	286.40	0.91	250.40	-13.33
0.50	293.02	296.53	1.18	259.30	-13.01
0.60	307.23	305.86	-0.45	266.85	-15.13

0.70	322.92	314.72	-2.60	273.50	-18.07
0.80	333.74	323.33	-3.22	279.49	-19.41
0.90	345.47	331.82	-4.11	284.99	-21.22
1.00	355.03	340.30	-4.33	290.12	-22.37
1.10	358.21	348.81	-2.70	294.96	-21.44
1.20	373.15	357.42	-4.40	299.58	-24.56
1.30	393.37	366.16	-7.43	304.01	-29.39
1.40	402.03	375.06	-7.19	308.30	-30.40
1.50	414.24	384.15	-7.83	312.48	-32.56
1.60	425.79	393.43	-8.23	316.57	-34.50
1.70	438.07	402.94	-8.72	320.60	-36.64
1.80	451.90	412.68	-9.50	324.58	-39.23
1.90	458.92	422.68	-8.57	328.52	-39.70
2.00	473.66	432.95	-9.40	332.43	-42.48
2.10	491.03	443.51	-10.71	336.34	-45.99
2.20	496.11	454.38	-9.18	340.24	-45.81
2.30	507.45	465.58	-8.99	344.15	-47.45
2.40	525.79	477.13	-10.20	348.07	-51.06
2.50	538.96	489.06	-10.20	352.00	-53.11
2.60	557.40	501.38	-11.17	355.97	-56.59
2.70	575.48	514.13	-11.93	359.96	-59.87
2.80	589.08	527.34	-11.71	363.99	-61.84
2.90	601.40	541.05	-11.16	368.05	-63.40
3.00	608.24	555.27	-9.54	505.30	-20.37
3.10	618.24	570.06	-8.45	703.13	12.07
3.20	643.43	585.45	-9.90	730.64	11.94
3.30	668.31	601.49	-11.11	759.81	12.04
3.40	682.66	618.22	-10.42	790.73	13.67
3.50	696.92	635.68	-9.63	823.51	15.37
3.60	697.10	653.94	-6.60	858.27	18.78
3.70	719.70	673.04	-6.93	895.15	19.60
3.80	757.66	693.04	-9.32	934.25	18.90
3.90	764.57	715.54	-6.85	977.83	21.81
4.00	784.30	742.36	-5.65	1028.58	23.75
4.10	805.28	772.24	-4.28	1084.94	25.78
4.20	823.01	803.60	-2.42	1144.88	28.11
4.30	854.59	836.54	-2.16	1208.65	29.29

4.40	878.84	871.17	-0.88	1276.48	31.15
4.50	899.81	907.59	0.86	1348.66	33.28
4.60	915.63	945.93	3.20	1425.47	35.77
4.70	923.16	986.29	6.40	1507.23	38.75
4.80	960.67	1028.81	6.62	1594.24	39.74
4.90	1005.56	1073.61	6.34	1686.88	40.39
5.00	1019.34	1120.83	9.05	1785.50	42.91

A5 Fatigue life prediction – C-joints root failure at RT

Table A.4 Specimen configuration of C-joint specimens

Weld-ment	Steel	Tempe-rature	Stress ratio	Failure location	H [mm]	W [mm]	T [mm]	t [mm]	Δσ [MPa]	N_f - expe-rimental
C-joint	S235	RT	0	Root	8.83	7.78	10.1	10	134.45	200397
C-joint	S235	RT	0	Root	8.92	7.9	10.1	10	96.29	513308
C-joint	S235	RT	0	Root	8.74	8.18	10.1	10	189.18	63264
C-joint	S235	RT	0	Root	8.58	8.2	10.1	10	92.84	617488
C-joint	S235	RT	0	Root	8.57	7.91	10.1	10	75.56	1107726
C-joint	S235	RT	0	Root	8.81	8.34	10.1	10	128.84	175885
C-joint	S235	RT	0	Root	8.59	8.34	10.1	10	66.42	1450935
C-joint	S235	RT	0	Root	8.46	8.96	10.1	10	144.41	175690
C-joint	S235	RT	0	Root	8.9	8.94	10.1	10	92.09	533189
C-joint	S235	RT	0	Root	8.79	8.8	10.1	10	66.52	1983106
C-joint	S235	RT	0	Root	8.55	9.09	10.1	10	79.25	1190738
C-joint	S235	RT	0	Root	6.58	8.93	10.1	10	73.81	1542842
C-joint	S500	RT	0	Root	7.89	8.56	10	10	150.56	134308
C-joint	S500	RT	0	Root	7.43	8.89	10	10	188.02	133046
C-joint	S500	RT	0	Root	7.43	8.87	10	10	59.95	2181756
C-joint	S500	RT	0	Root	7.46	9.18	10	10	189.48	62366
C-joint	S500	RT	0	Root	7.45	9.44	10	10	68.06	1477773
C-joint	S500	RT	0	Root	7.42	9.14	9.9	10	101.93	576098
C-joint	S500	RT	0	Root	7.3	9.45	10	10	73.73	1496514
C-joint	S500	RT	0	Root	7.27	9.18	10	10	109.67	548545
C-joint	S500	RT	0	Root	8.58	7.94	9.9	10	119.7	466503
C-joint	S500	RT	0	Root	7.71	6.97	10	10	146.58	251687
C-joint	S500	RT	0	Root	7.71	10.45	9.8	10	96.25	290161
C-joint	S500	RT	0	Root	7.96	10.03	9.9	10	60.08	1469382

Table A.5 Predicted fatigue lifes

Specimen	N_f - WM BS7910	N_f - WM IIW	N_f - S235 WM Sal-laba	N_f - expe-rimental	N_f - WM BS7910	N_f - WM IIW	N_f – S500 WM Sal-laba	N_f - expe-rimental
1	173190	67807	164181	200397	143484	56520	198157	134308
2	503484	190511	493855	513308	74213	29838	119339	133046
3	66799	26978	61386	63264	2539379	911118	1758411	2181756
4	599316	225501	591163	617488	77258	31033	123331	62366
5	1046492	386647	1051251	1107726	1947664	705024	1439520	1477773
6	228248	88617	218192	175885	542395	204540	542861	576098
7	1759978	639607	1797411	1450935	1521359	554820	1188779	1496514
8	183043	71586	173707	175690	412417	156882	440211	548545
9	758964	283640	753713	533189	273847	105636	323971	466503
10	1986618	719694	2035226	1983106	98644	39244	146903	251687
11	1219493	448698	1230100	1190738	891189	331148	798647	290161
12	1162589	427030	1174821	1542842	3559157	1264944	2294095	1469382

A6 Fatigue life prediction – transversal stiffener at RT

Table A.6 Specimen configuration of transversal stiffener specimens

Weldment	Steel	Tempe-rature	Stress ratio	Failure location	H [mm]	W [mm]	T [mm]	t [mm]	Δσ [MPa]	N_f - experi-mental
transversal stiffener	S235	RT	0	Toe	7.93	8.14	10	10	159.94	1509639
transversal stiffener	S235	RT	0	Toe	7.81	8.8	9.9	10	134.14	1161853
transversal stiffener	S235	RT	0	Toe	7.56	8.31	10.1	10	226.72	493274
transversal stiffener	S235	RT	0	Toe	7.64	7.73	10	10	153.1	763297
transversal stiffener	S235	RT	0	Toe	7.77	7.83	10	10	255.94	135579
transversal stiffener	S235	RT	0	Toe	7.56	7.81	9.7	10	189.66	235077
transversal stiffener	S235	RT	0	Toe	7.72	7.94	10	10	130.67	804553
transversal stiffener	S235	RT	0	Toe	7.75	7.54	9.9	10	224	185544
transversal stiffener	S235	RT	0	Toe	7.3	7.35	10.1	10	158.43	516850
transversal stiffener	S500	RT	0	Toe	6.81	7.38	9.8	10	163.68	1115441
transversal stiffener	S500	RT	0	Toe	7.07	7.78	9.8	10	157.69	1552463

transversal stiffener	S500	RT	0	Toe	6.65	7.38	9.8	10	271.16	168696
transversal stiffener	S500	RT	0	Toe	6.92	7.77	9.8	10	164.44	959266
transversal stiffener	S500	RT	0	Toe	6.75	7.27	9.8	10	287.07	127220
transversal stiffener	S500	RT	0	Toe	7.08	7.89	9.9	10	219.28	340001
transversal stiffener	S500	RT	0	Toe	6.72	7.64	10	10	163.54	1164655
transversal stiffener	S500	RT	0	Toe	6.92	7.12	9.8	10	355.53	62466
transversal stiffener	S500	RT	0	Toe	7.42	7.96	9.8	10	218.73	264277
transversal stiffener	S500	RT	0	Toe	7.1	7.57	9.9	10	175.64	666117

Table A.7 Predicted fatigue lifes

Specimen	N_f - WM BS7910	N_f - WM IIW	N_f - S235 WM Sallaba	N_f - experimental	N_f - WM BS7910	N_f - WM IIW	N_f – S500 WM Sallaba	N_f - experimental
1	303831	527653	2326860	1509639	290131	503862	627372	1115441
2	512710	890407	4860144	1161853	323280	561429	708612	1552463
3	106438	184848	537388	493274	63927	111021	114185	168696
4	348218	604738	2818604	763297	285590	495974	616499	959266
5	74422	129247	324747	135579	53808	93447	93991	127220
6	185720	322534	1174761	235077	119618	207736	231107	340001
7	559049	970882	5469781	804553	288436	500918	623163	1164655
8	111731	194039	573732	185544	28273	49101	45489	62466
9	313724	544834	2434705	516850	120550	209354	233037	264277
10					232940	404540	489445	666117

A7 Fatigue life prediction for C-joints at different temperatures

Table A.8 Specimen configuration of C-joint specimens

Weldment	Steel	Temperature	Stress ratio	Failure location	H [mm]	W [mm]	T [mm]	t [mm]	Δσ [MPa]	N_f - experimental
C-joint	S500	RT	0	Root	7.89	8.56	10	10	150.56	134308
C-joint	S500	M50	0	Root	8.22	8.83	9.9	10	87.09	1280183
C-joint	S500	M50	0	Root	7.92	8.43	9.9	10	151.55	284986
C-joint	S500	RT	0	Root	7.43	8.89	10	10	188.02	133046
C-joint	S500	M50	0	Root	7.27	9.12	10	10	154.58	292182
C-joint	S500	RT	0	Root	7.43	8.87	10	10	59.95	2181756
C-joint	S500	RT	0	Root	7.46	9.18	10	10	189.48	62366

C-joint	S500	RT	0	Root	7.45	9.44	10	10	68.06	1477773
C-joint	S500	RT	0	Root	7.42	9.14	9.9	10	101.93	576098
C-joint	S500	RT	0	Root	7.3	9.45	10	10	73.73	1496514
C-joint	S500	RT	0	Root	7.27	9.18	10	10	109.67	548545
C-joint	S500	M20	0	Root	7.44	8.49	9.9	10	189.48	114953
C-joint	S500	M20	0	Root	7.05	9.22	9.9	10	79.06	1119176
C-joint	S500	MT50	0	Root	7.63	8.66	9.9	10	83.67	1195473
C-joint	S500	M20	0	Root	8	8.45	9.9	10	141.36	311537
C-joint	S500	M50	0	Root	8.5	9.18	10	10	189.64	245270
C-joint	S500	M50	0	Root	8	8.92	10	10	178.8	317495
C-joint	S500	M20	0	Root	7.25	7.4	9.9	10	283.3	81776
C-joint	S500	M20	0	Root	7.79	9.35	9.9	10	173.79	276996
C-joint	S500	M20	0	Root	7.21	8.86	9.9	10	162.31	244758
C-joint	S500	RT	0	Root	8.58	7.94	9.9	10	119.7	466503
C-joint	S500	M20	0	Root	7.93	9.74	10	10	94.04	1191167
C-joint	S500	M50	0	Root	8.11	9.81	9.9	10	253.49	78425
C-joint	S500	M50	0	Root	8.27	7.9	9.9	10	208.62	128434
C-joint	S500	M20	0	Root	8.15	10.1	9.9	10	201.77	107830
C-joint	S500	M50	0	Root	7.98	9.92	9.9	10	102.15	821066
C-joint	S500	M20	0	Root	7.58	9.65	9.9	10	113.77	496190
C-joint	S500	RT	0	Root	7.71	6.97	10	10	146.58	251687
C-joint	S500	RT	0	Root	7.71	10.45	9.8	10	96.25	290161
C-joint	S500	M50	0	Root	7.72	10.37	10	10	103.81	609769
C-joint	S500	M20	0	Root	7.86	10.41	9.9	10	74.1	1313662
C-joint	S500	M20	0	Root	7.75	9.9	9.9	10	104.1	390510
C-joint	S500	RT	0	Root	7.96	10.03	9.9	10	60.08	1469382
C-joint	S500	M20	0	Root	7.99	9.91	9.9	10	98.07	412030
C-joint	S500	M20	0	Root	7.31	8.86	9.9	10	250.86	46177
C-joint	S500	M50	0	Root	8.2	10.22	9.9	10	173.91	154210
C-joint	S500	M20	0	Root	7.94	9.16	9.9	10	132.28	279244

Table A.9 Predicted fatigue lifes

Temperature Exp.	N_f - S235 Sal-laba RT	N_f - S235 Sal-laba M0	N_f - S235 Sal-laba M20	N_f - S235 Sal-laba M40	N_f - S235 Sal-laba M60	N_f - experi-mental
RT	198157	193653	187979	203260	235276	134308
RT	119339	116627	113209	122412	141694	133046
RT	1758411	1718442	1668089	1803692	2087792	2181756
RT	123331	120528	116996	126507	146433	62366

RT	1439520	1406800	1365578	1476590	1709168	1477773
RT	542861	530522	514976	556840	644548	576098
RT	1188779	1161758	1127716	1219391	1411457	1496514
RT	440211	430205	417599	451547	522670	548545
RT	323971	316607	307330	332313	384656	466503
RT	146903	143564	139358	150686	174421	251687
RT	798647	780494	757624	819214	948248	290161
RT	2294095	2241950	2176256	2353170	2723818	1469382
M20	112656	110096	106869	115557	133759	114953
M20	952467	930818	903543	976994	1130881	1119176
M20	233251	227949	221270	239257	276943	311537
M20	34081	33306	32330	34958	40465	81776
M20	165812	162043	157295	170082	196871	276996
M20	168347	164521	159700	172682	199881	244758
M20	739474	722665	701490	758516	877990	1191167
M20	135521	132440	128560	139011	160906	107830
M20	463792	453250	439968	475735	550668	496190
M20	1450255	1417291	1375762	1487601	1721913	1313662
M20	601517	587844	570619	617006	714191	390510
M20	710882	694724	674367	729188	844042	412030
M20	60732	59351	57612	62296	72108	46177
M20	309179	302152	293298	317141	367094	279244
M50	797355	779231	756398	817888	946713	1280183
M50	195548	191103	185504	200584	232178	284986
M50	192790	188408	182887	197755	228903	292182
M50	135435	132357	128479	138923	160805	245270
M50	141989	138762	134696	145646	168586	317495
M50	75036	73330	71181	76968	89091	78425
M50	84581	82658	80236	86759	100424	128434
M50	643194	628574	610156	659757	763676	821066
M50	628498	614213	596215	644683	746227	609769
M50	195291	190852	185260	200320	231873	154210

A8 Fatigue life prediction for transversal stiffener at different temperatures

Table A.10 Specimen configuration of transversal stiffener specimens

Weldment	Steel	Tempe-rature	Stress ratio	Failure location	H [mm]	W [mm]	T [mm]	t [mm]	Δσ [MPa]	N_f - expe-rimental

transversal stiffener	S500	M50	0	Toe	6.89	8.33	9.8	10	188.13	1622199
transversal stiffener	S500	RT	0	Toe	6.81	7.38	9.8	10	163.68	1115441
transversal stiffener	S500	RT	0	Toe	7.07	7.78	9.8	10	157.69	1552463
transversal stiffener	S500	RT	0	Toe	6.65	7.38	9.8	10	271.16	168696
transversal stiffener	S500	RT	0	Toe	6.92	7.77	9.8	10	164.44	959266
transversal stiffener	S500	M50	0	Toe	6.88	7.71	9.8	10	337.84	92407
transversal stiffener	S500	RT	0	Toe	6.75	7.27	9.8	10	287.07	127220
transversal stiffener	S500	M20	0	Toe	6.85	7.73	9.9	10	264.31	153744
transversal stiffener	S500	M20	0	Toe	6.81	7.56	9.9	10	216.6	359963
transversal stiffener	S500	M20	0	Toe	7.07	7.87	9.9	10	224.17	363454
transversal stiffener	S500	M20	0	Toe	7.48	7.6	9.8	10	247.15	162264
transversal stiffener	S500	M50	0	Toe	7.18	7.75	9.9	10	313.53	113804
transversal stiffener	S500	M20	0	Toe	7.05	7.73	9.8	10	199.67	501744
transversal stiffener	S500	RT	0	Toe	7.08	7.89	9.9	10	219.28	340001
transversal stiffener	S500	RT	0	Toe	6.72	7.64	10	10	163.54	1164655
transversal stiffener	S500	M50	0	Toe	7.17	7.91	9.9	10	316.9	134674
transversal stiffener	S500	M50	0	Toe	6.88	7.59	9.8	10	270.89	221062
transversal stiffener	S500	M50	0	Toe	7.08	7.73	9.8	10	165.38	796126
transversal stiffener	S500	M50	0	Toe	6.64	7.56	9.8	10	262.09	290906
transversal stiffener	S500	M20	0	Toe	7.04	7.53	9.8	10	156.97	1671841
transversal stiffener	S500	M20	0	Toe	7.36	7.89	9.8	10	329.39	99708
transversal stiffener	S500	M50	0	Toe	7.19	7.9	9.8	10	216.78	359960

transversal stiffener	S500	M50	0	Toe	6.86	7.24	9.9	10	253.55	168862
transversal stiffener	S500	M20	0	Toe	7.19	7.67	9.8	10	227.64	318516
transversal stiffener	S500	M20	0	Toe	7.24	7.78	9.8	10	303.43	126662
transversal stiffener	S500	M20	0	Toe	7.17	7.28	9.8	10	165.94	838979
transversal stiffener	S500	RT	0	Toe	6.92	7.12	9.8	10	355.53	62466
transversal stiffener	S500	M20	0	Toe	6.55	6.72	9.8	10	165.76	1015536
transversal stiffener	S500	M50	0	Toe	7.15	7.12	9.8	10	238.45	321248
transversal stiffener	S500	M20	0	Toe	6.88	7.19	9.7	10	253.86	252670
transversal stiffener	S500	RT	0	Toe	7.42	7.96	9.8	10	218.73	264277
transversal stiffener	S500	RT	0	Toe	7.1	7.57	9.9	10	175.64	666117
transversal stiffener	S500	M50	0	Toe	6.67	7.34	9.9	10	201.85	450327
transversal stiffener	S500	M50	0	Toe	6.69	6.79	9.8	10	163.87	1189241

Table A.11 Predicted fatigue lifes

Temperature Exp.	**N_f - S235 Sal-laba RT**	**N_f - S235 Sal-laba M0**	**N_f - S235 Sal-laba M20**	**N_f - S235 Sal-laba M40**	**N_f - S235 Sal-laba M60**	**N_f - experi-mental**
RT	627372	454600	649539	678154	965039	1115441
RT	708612	513467	733650	765971	1090006	1552463
RT	114185	82739	118219	123427	175642	168696
RT	616499	446721	638283	666402	948315	959266
RT	93991	68106	97312	101599	144579	127220
RT	231107	167462	239273	249814	355495	340001
RT	623163	451550	645182	673605	958566	1164655
RT	45489	32962	47096	49171	69972	62466
RT	233037	168861	241271	251900	358463	264277
RT	489445	354656	506739	529063	752877	666117
M20	123433	89441	127795	133424	189868	153744
M20	242041	175385	250593	261633	372314	359963
M20	214554	155468	222135	231922	330033	363454
M20	154447	111913	159904	166948	237574	162264

M20	319254	231335	330535	345096	491085	501744
M20	720397	522007	745852	778710	1108133	1671841
M20	58485	42379	60551	63219	89963	99708
M20	204600	148255	211829	221161	314721	318516
M20	77366	56060	80100	83628	119006	126662
M20	596083	431927	617145	644333	916910	838979
M20	601096	435560	622335	649752	924621	1015536
M20	143008	103625	148061	154584	219978	252670
M50	390102	282672	403886	421679	600065	1622199
M50	54118	39214	56030	58498	83245	92407
M50	68944	49958	71380	74525	106052	113804
M50	66469	48164	68818	71850	102245	134674
M50	114182	82738	118217	123425	175638	221062
M50	603290	437150	624606	652123	927996	796126
M50	128175	92877	132704	138550	197162	290906
M50	241098	174702	249617	260614	370863	359960
M50	141890	102815	146903	153375	218259	168862
M50	175041	126836	181226	189210	269253	321248
M50	307678	222947	318550	332584	473279	450327
M50	624129	452250	646183	674650	960052	1189241